FIRST-PRINCIPLES CALCULATIONS OF HELIUM CLUSTER FORMATION IN PALLADIUM TRITIDES

A Thesis
Presented to
The Academic Faculty

by

Pei Lin

In Partial Fulfillment
of the Requirements for the Degree
Doctor of Philosophy in the
School of Physics

Georgia Institute of Technology
August 2010

FIRST-PRINCIPLES CALCULATIONS OF HELIUM CLUSTER FORMATION IN PALLADIUM TRITIDES

Approved by:

Professor Mei-Yin Chou, Advisor
School of Physics
Georgia Institute of Technology

Professor Andrew Zangwill
School of Physics
Georgia Institute of Technology

Professor James Gole
School of Physics
Georgia Institute of Technology

Professor David Sholl
School of Chemical and Biomolecular Engineering
Georgia Institute of Technology

Professor Phillip N. First
School of Physics
Georgia Institute of Technology

Date Approved: May 10, 2010

To my beloved family

ACKNOWLEDGEMENTS

I owe my sincere gratitude to all who have helped me, encouraged me, and believed in me through this challenging journey.

Foremost, I am deeply indebted to my thesis advisor, Professor Mei-Yin Chou, for every advice and opportunity she provided me through the years of my education. Her exceptional insight and broad-minded guidance led me the way to be a critical-thinking and self-stimulating physicist, which would be my greatest asset in the future. I owe my sincere thanks to Professor Andrew Zangwill, Professor James Gole, Professor Phillip First, and Professor David Sholl for their precious time being in my thesis defense committee.

I am thankful to our previous and current group members Dr. Amra Peles, Dr. Li Yang, Dr. Zhu Ma, Dr. Wolfgang Geist, Dr. Alexis Nduwinmana, Dr. Jia-An Yan, Dr. Wen-Ying Ruan, Dr. Li Huang, Dr. Salvador Barraza-Lopez, Dr. Feng Zhang, and Lede Xian. I considered myself very fortunate to be able to spend a lot of time with these outstanding people. I cordially thank Dr. Yan Wang, for her experienced knowledge and patient discussion in helping me completing this work.

There are so many great people at Georgia Tech who have helped and inspired me in various ways. I thank the people in the school of Physics. Their friendship and enthusiasm for science make the department the most exciting and stimulating place for learning.

Finally, my heartfelt gratitude goes to my beloved family, especially my parents and my cousin, Show-Chaun Chen. I would not be able to on the path to a self-esteem and self-discipline life without their constant support, inspiration, and encouragement.

TABLE OF CONTENTS

LIST OF TABLES

LIST OF FIGURES

SUMMARY

The accumulation of helium atoms in metals or metal tritides is known to result in the formation of helium bubbles in the lattice and to cause degradation of the material. Helium is introduced either through a neutron transmutation reaction or via the radioactive decay of tritium. The close-shelled helium atom is chemically inactive to the metals. It will diffuse rapidly in the interstitial region until it reaches a trapping site. Therefore, a low helium diffusion barrier and the preferred attachment to a defect serves as two sufficient conditions for the growth of helium bubbles. This thesis is aimed to use first-principles calculations to study helium diffusion and helium cluster formation in the metal and metal tritides. The advantage of using first-principles calculations is to gain reliable insights, without experimental parameters, of the atomistic behavior which gives rise to the macroscopic phenomenon. In addition, one of the values of atomistic simulation is to examine in detail the atomistic processes, at the level that experimental measurements cannot reach.

We present a first-principles investigation in Chapter 3 to study the helium cluster formation in pure palladium bulk. Hydrogen diffusing into the palladium system has been studied extensively in the past; one of the reasons is that palladium exhibits fast kinetics for absorption and desorption of hydrogen and hydrogen isotopes. The diffusion of tritium and helium in palladium is studied by calculating their potential energy surface in the interstitial region and zero point energies at the local minimum sites. A self-trapping mechanism is found for helium cluster formation. Five or more interstitial helium atoms are energetically favorable to create a Frenkel defect consisting of a lattice vacancy and a palladium atom at the interstitial position. This self-interstitial atom energetically diffuses away. The vacancy defect has a higher tendency to trap more helium atoms that ultimately grow to a larger cluster.

In Chapter 4 we consider the helium cluster formation in palladium hydrides with various hydrogen concentrations. Palladium readily forms reversible hydrides at equilibrium pressures under one atm, with hydrogen occupying octahedral sites in the face-centered-cubic (fcc) palladium lattice. By loading hydrogen atoms at certain concentrations, a local minimum site with a higher diffusion barrier can trap the helium atom generated from tritium decay. The diffusion mechanism is studied systematically in these hydrides. Similar to pure palladium, the self-trapping mechanism is identified in palladium hydrides with a hydrogen concentration at 0.25 and 0.50. This chapter discusses the effects on the helium behavior due to the electronic structure changes in the presence of hydrogen.

A metal alloy could impede helium mobility because it creates local trapping sites in a less homogeneous interstitial region. The helium diffusion in palladium-based alloys with M = Cu, Ag, Au, and Pt is evaluated by searching the transition states between the local minima with first-principles calculations. A higher activation energy in $Pd_{87.5}Pt_{12.5}$ compared to that in pure Pd is in agreement with recent experimental results concerning helium bubble formation in pure Pd and $Pd_{90}Pt_{10}$. The results provide a first-step understanding of how alloying can affect helium migration properties in tritium storage application.

CHAPTER I

INTRODUCTION

Serious concerns over the reliability of the fossil fuel supply, as well as the environmental issue, have refocused public attention on the search for alternative energy sources. One result in recent years has been a renewed interest in nuclear technology as a large-scale source of energy with zero emissions of carbon-dioxide as a byproduct. There is now an opportunity for research which can improve new fission energy systems as well as establish promising fusion energy by employing the deuterium-tritium (DT) fusion reaction. A general challenge for both types of nuclear energy systems is the need for materials research to improve the service lifetime of the structural walls of the reactor or the storage medium for the radioactive products. The economically and environmentally acceptable performance of advanced fission and fusion systems will require significant advances in material technology.

Among many aspects in nuclear materials research, one major problem is the formation of helium bubbles, which can have a significant impact on the mechanical properties and structural stability of materials in radiation environments [1, 2, 3]. Helium is the second lightest element on earth with a close-shell electronic structure. The element is traditionally referred to as a noble gas atom, indicating that it is chemically inactive with other elements. In nuclear energy systems, helium is created from nuclear reactions. Due to different nuclear reaction processes, helium is found inside two types of materials: metals and metal tritides.

Helium is introduced into metals via the (n,α) transmutation reactions in neutron-irradiated materials. These materials serve as the main structural components in the reactor subject to high-energy neutron radiation beams during the reaction. The collisions of the neutrons with the metal atoms produce numerous defects and helium atoms in the host matrix. The properties of these helium defects have been studied mostly for iron and iron alloys [4, 5, 6], which are known to be promising materials for fusion technology [7]. Research on helium in other metals such as molybdenum [8], tungsten [9, 10, 11], and copper [12] has

also drawn theoretical interest in the past.

Helium also exists in metal tritides through tritium decay. Tritium is the hydrogen isotope with one proton and two neutrons. The element is created as a byproduct from fission reactions or neutron activity reactions [2]. Tritium atoms could contaminate the environment by replacing hydrogen atoms and form tritium compounds, which are hazardous to the human body. Therefore, tritium has to be processed and stored safely. One solution is to store tritium in metal tritides. However, unlike the proton or deuterium, tritium is radioactive and will decay into helium-3 as a final product. This is known as the "tritium trick": a tritium atom transmutes into a β particle, an anti-neutrino, and a helium-3 atom with a half-life of 12.3 years:

$$^{3}\mathrm{H} \rightarrow \bar{\nu}_e + \beta^- + {}^{3}\mathrm{He}. \tag{1.1}$$

During this decay process, the recoil energy of the electron and the helium atom is about 5.7 keV and 1.03 eV, respectively. Because the energy for the helium product is insufficient to cause any lattice defect in host materials [13], the helium atom is generated at the interstitial site originally occupied by the tritium atom. These insoluble helium atoms can diffuse and agglomerate into nano-sized bubbles to produce dislocations and voids in metal tritides. These dislocations and voids are further populated with helium bubbles, which cause some macroscopic events such as lattice swelling, work hardening, and other plastic deformations, all of which lead to irreversible changes in some mechanical properties, ultimately causing the loss of material functionality. In the past, experimental investigation of aging metal tritides including niobium, tantalum [14, 15], titanium [16], zirconium [2], erbium [17, 18], palladium [19, 20, 21] , and $LaNi_5$ [22] have been studied in connection with the formation of helium bubbles in tritium storage application.

A considerable body of experimental work has been carried out to study tritium storage systems. Bowman, who based his nuclear magnetic resonance (NMR) studies on various metal tritides, suggested that the helium bubbles would form early in palladium tritides [23]. Using transmission electron microscopy (TEM), Thomas [24, 25] observed the images of

helium bubbles in young-aged palladium tritides ($PdT_{0.66}$). These bubbles having diameters of 1-2 nm distribute uniformly in the tritide with a density of 10^{23} bubbles/m^3. In addition to the formation of helium bubbles, understanding of the capacity of helium trapped inside the bubbles can be further assisted by the use of thermal desorption-mass spectroscopy (TD-MS) experiments. Abell et al. [26, 27] measured helium desorption and found that, in the early stages of tritium storage, only a small fraction of the helium atoms produced are released compared to the amount of helium generated in the matrix, indicating that most helium atoms are trapped inside the bubbles. When the ratio of helium to matrix atoms has reached its critical limit, these bubbles burst and a large amount of helium escapes from the solid. The limiting ratio for helium in $PdT_{0.66}$ at room temperature is around 0.5. This result with the initial condition of tritium concentration (0.66) and its decay coefficient indicate that helium can be retained in bulk palladium for more than ten years [26]. Fabre et al. [28] applied the microcantilever method to measure the elastic properties of palladium tritides. They found that the Young's modulus of the sample increases sharply in the first few weeks and increases at much slower rate afterwards [28].

The preparation of tritide samples consumes tremendous labour and time due to their radioactive nature and the long half-life of tritium. In addition, the high migration mobility of helium atoms in solids presents a challenge using modern experimental facilities to provide direct information of the helium diffusion mechanism [29, 30]. However, advances in modeling and computational technologies can provide a comparatively inexpensive tool to study these phenomena and give us a better understanding of the properties at the atomic scale, a level of understanding not achievable through traditional experiments.

For a helium-metal system, *ab initio* calculations based on density functional theory (DFT) can describe the interactions between metals and noble gas atoms with better accuracy compared to the empirical potential methods[31]. Seletskaia et al. [32] studied helium in iron using *ab initio* calculations. They showed that helium is more energetically favorable at the tetrahedral site over the octahedral site in the bcc iron lattice regarding magnetic interactions. Earlier simulations using pair potential and effective medium models [33, 34]

have found octahedral site most energetically stable. In addition to providing more accurate energetics information of helium-metal interactions, the *ab initio* method addresses the electronic properties of helium inside metals to understand the hybridization between metal and helium electronic states [35, 36].

To study helium diffusion properties in metals, Fu [37] and Domain [38] conducted studies using *ab initio* calculations in the bcc metal lattice. Fu found a very low activation energy, around 0.1 eV, for interstitial helium in iron, suggesting that helium atoms can diffuse at low temperatures in the interstitial region of bulk iron. He also evaluated the formation of small helium-vacancy complexes and found that helium stabilizes the vacancy cluster and that the optimized ratio of helium-to-vacancy is 1.3 with both the helium and the vacancy dissociation energy equal to 2.6 eV [37]. Domain, with *ab initio* calculations, found strong helium to helium binding in the bcc tungsten lattice, indicating the mobile helium interstitial can be decelerated by being trapped with another helium atom [38]. In the study of the helium diffusion properties in erbium tritides (ErT_2), Wixom et al. [39] reported an activation energy of 0.49 eV for helium migration in the tritides if a neighboring vacant interstitial site exists. The concerted motion of helium diffusion, with a hydrogen atom moved out of the way temporarily, is calculated in the study and the activation energy of this diffusion is 0.88 eV. [39].

Palladium and palladium hydride systems have been studied extensively in the past because palladium has a high solubility of hydrogen atoms and can be permeated fast by hydrogen atoms [40, 41, 42]. Palladium is also used as a material for storing tritium for many reasons: palladium readily forms palladium tritide under ambient conditions [43]; the palladium bulk is resistant to oxidation and poisoning [22]; it has fast kinetics of absorption and desorption of tritium gas. In addition, the ability to retain helium atoms in the metal lattice for a long time [26] also makes palladium tritide a prototype material in helium-tritide research. The *ab initio* studies of hydrogen in palladium would be a convenient starting point for tritium in palladium since the electronic properties of hydrogen and its isotopes are similar within the Born-Oppenheimer approximation [44]. In this work, we revisit the hydrogen isotopes and palladium system using *ab initio* methods to unfold the

properties of helium diffusion and helium cluster formation in metals, metal tritides, and alloys.

This work focuses on the atomic configuration and the migration mechanism of helium atoms, as well as the nucleation process of small helium clusters by applying DFT calculations. Understanding the diffusion mechanism is essential for the understanding of bubble formation and growth. The diffusion coefficient obeys the Arrhenius relation:

$$D = D_0 e^{-E_a/(k_B T)}, \tag{1.2}$$

where D_0 is the pre-exponential coefficient, and E_a is the activation energy along the diffusion path. The exponential function indicates that the value of E_a requires a high degree of accuracy. This high level of accuracy requires calculations of the barriers along the diffusion path on the multi-dimensional surface using first-principles calculations [45].

In aging metal tritides, because the intrinsic point defects are not produced concurrently with the emergence of helium atoms, a critical step in the nucleation process of helium clusters occurs through the self trapping mechanism [46, 47]. In this process, interstitial helium atoms migrate and aggregate to form small clusters. At some critical number of helium atoms, it becomes energetically favorable for the matrix to create a Frenkel pair consisting of a vacancy and a self-interstitial atom (SIA) in order to accommodate the helium cluster. These defects facilitate bubble growth by further attracting helium atoms and ejecting more metal atoms. In this nucleation mechanism, both the formation energy of a self-interstitial atom and the optimized ratio of helium-to-vacancy become important factors for one to understand the experimental observations of the bubble growth and bubbles distribution [20].

The first part of this work applies first-principles calculations to examine the energetics of hydrogen, helium, and the nucleation of helium clusters in the fcc palladium lattice. We then examine the potential energy surface of helium in the lattice with and without a vacancy defect and compare it with that of hydrogen in the same environment [48, 49]. It is revealed that five or more interstitial helium atoms are energetically favorable to form

a Frenkel defect in the fcc Pd lattice, with a Pd atom being pushed to an interstitial site. This Pd self-interstitial energetically diffuses away, and a vacancy site is left with the helium cluster. The use of a 108 Pd supercell allows us to consider the formation of clusters up to fifteen helium atoms around a single palladium vacancy site. The strain field due to the cluster formation is analyzed in order to explain the structural and energetic properties.

The second part of this work studies the energetics of helium atoms and cluster formation in palladium hydrides (PdH_x) at various hydrogen concentrations. For each compound, we start with the minimum-energy configuration which was determined from a previous first-principles study [50]. The palladium hydride has an fcc palladium lattice in which hydrogen atoms occupy octahedral sites in a specific order. The electronic structure is examined in order to understand the interaction among helium, hydrogen, and the metal Pd atom. It is found that the helium diffusion barrier can be increased by loading hydrogen into the lattice for a certain range of hydrogen concentration. We calculated the atomic attachment energies for helium clusters with a size up to six atoms with and without a lattice vacancy in $PdH_{0.25}$ and $PdH_{0.5}$. The chapter also discusses the effects on the helium behavior due to the presence of hydrogen in palladium hydrides.

In the last part of this thesis, helium in Pd-based alloys is studied with first-principles calculations. Metal alloying is suggested to yield dense trapping sites inside the bulk and to disrupt the migration of helium atoms [7, 51]. As a result, alloys can preserve the integrity of the materials for a longer time. Experimentally, compared to pure Pd, the $Pd_{90}Pt_{10}$ alloy is found to have fewer helium bubbles and dislocation loops when it is used as a tritium storage material [52]. We design several models to understand the change of helium energetics due to substituting Pt atoms in palladium bulk. In addition, we extend our study with alloying elements including Cu, Ag, Au, and Pt. Our results provide a first-step understanding of how alloys can affect helium migration properties in the tritium storage application.

CHAPTER II

COMPUTATION BACKGROUND

This chapter gives a review of the fundamental concepts of first-principles calculations, which is the major computational method in my work. First-principles (*ab initio*) calculations by definition contain no empirical parameters, with the only input being atomic numbers and spatial coordinates of the atoms. The calculation is based on density functional theory (DFT) in order to describe a many-body system and to unravel many physical properties from the electronic structure of materials.

2.1 Density Functional Theory

All properties of materials can be derived from the interactions of electrons and ions. The interaction is described by the many-body Schrödinger's equation:

$$\hat{H}\Psi(\vec{r}_1, ..., \vec{r}_N) = E\Psi(\vec{r}_1, ..., \vec{r}_N). \tag{2.1}$$

Within the Born-Oppenheimer approximation that the motions of electrons and nuclei are decoupled, the Hamiltonian of electrons in the system has the form (in atomic units)

$$\hat{H} = \hat{T} + \hat{H}_{ee} + \hat{H}_{ext}, \tag{2.2}$$

where

$$\hat{T} = -\frac{1}{2}\sum_i \nabla_i^2 \tag{2.3}$$

$$\hat{H}_{ee} = \frac{1}{2}\sum_i \sum_j \frac{1}{|\vec{r}_i - \vec{r}_j|} \tag{2.4}$$

$$\hat{H}_{ext} = \frac{1}{2}\sum_\alpha \sum_i \frac{Z_\alpha}{|\vec{r}_i - \vec{R}_\alpha|} + \hat{V}_{field}(\vec{r}). \tag{2.5}$$

The three operators $\hat{t}$, $\hat{h}_{ee}$, and $\hat{h}_{ext}$ represent the kinetic energy operator, the electron-electron coulomb interaction, and the external potential (including the coulomb interaction with the atomic nuclei and the applied fields), respectively. The coordinate vectors $\vec{r}$ and $\vec{R}$ denote the positions of electrons and atoms, respectively, and Z_α is the valence number of the atom α. However, this equation is too complicated to be solved directly. To simplify the problem, density functional theory was developed to use the charge density of an N-electron system as the main input parameter:

$$n(\vec{r}) = \int |\Psi(\vec{r}, \vec{r}_2, ...\vec{r}_N)|^2 d\vec{r}_2 ... d\vec{r}_N. \tag{2.6}$$

2.1.1 Hohenberg-Kohn Theorems

The Hohenberg-Kohn theorem [64] demonstrates that the ground-state (GS) properties of a many-electron system can be expressed as a functional of the GS electron density. The theorem, proved by *Reductio ad absurdum*, shows that there exists a one-to-one mapping between the external potential $\mathrm{V_{ext}}$ and the GS electron density with a reference constant. Since the external potential determines the Hamiltonian, the ground state of the whole system can be determined by knowing the electron density.

In addition, the Hohenberg-Kohn theorem defines a global functional of $\mathrm{n}(\vec{r})$,

$$F[n] = \langle \Psi | \hat{T} + \hat{H}_{ee} | \Psi \rangle, \tag{2.7}$$

such that the total energy, at the true ground state density, has the minimum value corresponding to the many-body system, and that this minimum value is the ground state energy. By definition,

$$E[n(\vec{r})] = F[n(\vec{r})] + \int d\vec{r} n(\vec{r}) \mathrm{V_{ext}}(\vec{r}). \tag{2.8}$$

Overall, the theorems provide a revolutionary concept that one can bypass the many-body Schrödinger equation by introducing a global functional which depends only on the density function. Instead of solving for the many-body wave functions, the problem is reduced to minimize the energy functional by varying the charge density $n(\vec{r})$. Since the

exact functional is too difficult to find, the major effort is to find approximations to the global functional with well-defined assumptions.

2.1.2 Kohn-Sham Equation

The idea of the Kohn-Sham (KS) equation [67] is to construct the global functional F$[n(\vec{r})]$ which consists of three parts:

$$F[n(\vec{r})] = T_S[n(\vec{r})] + \frac{1}{2}\int d\vec{r}\int d\vec{r'}\frac{n(\vec{r})n(\vec{r'})}{|\vec{r}-\vec{r'}|} + E_{xc}[n(\vec{r})], \tag{2.9}$$

where $T_S[n]$ is the kinetic energy of a non-interacting electron gas that has the same GS density as the interacting system. $T_S[n]$ is constructed using a Slater determinant of orbitals as wave functions. The exchange-correlation energy functional, $E_{xc}[n(\vec{r})]$, is introduced in order to capture all the quantum mechanical and coulomb many-body effects left from the first two terms. For a slowly varying $n(\vec{r})$, the exchange-correlation energy can be assumed to have a localized form:

$$E_{xc} = \int d\vec{r} n(\vec{r})\epsilon_{xc}(n(\vec{r})), \tag{2.10}$$

where $\epsilon_{xc}(n)$ is the exchange-correlation energy per electron of a uniform electron gas of density n. This is the so-called local density approximation (LDA), in which the exchange-correlation energy is determined from the parameters of a uniform electron gas.

The Lagrange multiplier method is used to find the minimum of total energy subject to the orthogonality of one-electron wave functions, such that

$$L[n] = E_{tot}[n] - \sum_{ij}^{N}\lambda_{ij}[\langle\phi_i|\phi_j\rangle - \delta_{ij}], \tag{2.11}$$

where λ_{ij} is a set of multipliers. The partial derivative of $L[n]$ with respect to the wave function is zero. As a result, the problem is reduced to solving a series of one-electron Schrödinger-like equation (the Kohn-Sham equation):

$$\{-\frac{1}{2}\nabla^2 + V_{eff}(\vec{r})\}\psi_i(\vec{r}) = \epsilon_i\psi_i(\vec{r}), \tag{2.12}$$

where

$$\hat{V}_{eff}(\vec{r}) = V_{ext}(\vec{r}) + \int d\vec{r'}\frac{n(\vec{r'})}{|\vec{r} - \vec{r'}|} + \mu_{xc}(n(\vec{r}). \tag{2.13}$$

For the last term in the $\hat{V}_{eff}$ equation, $\mu_{xc}(n)$ is by definition the exchange and correlation part of the chemical potential in a uniform electron gas:

$$\mu_{xc}(n) = \frac{d(n\epsilon_{xc}(n))}{dn}. \tag{2.14}$$

Finally, the density is represented by summing the occupied solutions to the Kohn-Sham equation:

$$n(\vec{r}) = \sum_{i}^{N} |\psi_i(\vec{r})|^2. \tag{2.15}$$

The KS scheme is a self-consistent procedure that the Hamiltonian is determined by the charge density, which is a product of wave functions determined by the Hamiltonian. The problem can be solved iteratively. As the solution reaches convergence, the total energy can be obtained as

$$E = \sum_{i}^{N} \epsilon_i - \frac{1}{2}\int \vec{r}\int \vec{r'}\frac{n(\vec{r})n(\vec{r'})}{|\vec{r} - \vec{r'}|} + \int d\vec{r}[\epsilon_{xc}(n(\vec{r})) - \mu_{xc}(n(\vec{r}))]n(\vec{r}), \tag{2.16}$$

where ϵ_i is the eigenvalue of the KS equation. It has to be pointed out that the eigenvalues and eigenfunctions of the KS equation only have a mathematical meaning. The highest occupied eigenvalues can be equal to the ionization energy only if the "exact" exchange-correlation functional is employed.

2.1.3 Exchange-Correlation Functional

By definition, the exchange-correlation functional consists of exchange and correlation parts: $E_x(n)$ and $E_c(n)$. The exchange contribution $E_x(n)$ within the LDA can be calculated from the Dirac exchange-energy functional, while the correlation energy $E_c(n)$ of a uniform electron gas is determined by fitting the Monte Carlo results for a number of different densities to a suitable analytic interpolation formula.

Various generalized-gradient approximations (GGAs) have been developed with improvements over LDA in many aspects. In GGA, the functional includes the density n and its gradient ∇n as input parameters. Methods have been proposed to ensure that the functional preserves the desired properties in various limits. Examples of the GGA functionals include forms of Perdew and Wang (PW91) [63] and of Perdew, Burke, and Enzerhof (PBE) [59]. In this thesis, we use GGA with the PW91 functional.

2.2 Plane-Wave Pseudopotential Calculations

For a better computational performance in the DFT calculation, one of the major efforts is associated with the development of a highly efficient and easy-to-use implementation. It is convenient to use plane waves for solving the Kohn-Sham equation when periodic boundary conditions are applied to a system. However, the oscillatory terms of the valence wave functions in the core region require a large number of plane waves which makes the computation extremely slow. To overcome this inefficiency, the solution using the pseudopotential method is needed.

2.2.1 *ab initio* Pseudopotential Method

The idea of the pseudopotential approximation is that the electrons in a core region of an atom are inert to the atomic environment regarding binding and the low-energy excitation. In the core region, the valence wave function oscillates rapidly and requires a large number of plane waves in the calculation. The pseudopotential approach is applied in order to generate a substitute potential for which the wave function is smooth inside the core region and

coincides with the all-electron wave function outside the region. The *ab initio* pseudopotential is to calculate core-electron states with density functional theory and to construct the pseudopotential without fitting to experiments. These *ab initio* pseudopotentials are designed to be smooth with good accuracy under different chemical environments by adjusting the core radius (r_c). One procedure to generate pseudopotentials with a good transferability is through the norm-conserving method [56, 57]. This type of pseudopotential obeys the following conditions:

(1) The pseudo wave function contains no nodes, and the smooth function needs only a small number of plane waves in the expansion;

(2) The pseudo wave function (PS) is equal to the all-electron wave function (AE) beyond the chosen core radius r_c:

$$\phi_l^{PS}(r) = \phi_l^{AE}(r) \qquad \text{at } r > r_c; \tag{2.17}$$

(3) The valence pseudopotential and all-electron eigenvalues are equal:

$$\epsilon_l^{PS} = \epsilon_l^{AE}; \tag{2.18}$$

(4) The charges enclosed inside r_c for the two wave functions are equal:

$$\int_0^{r_c} dr|\phi_l^{PS}(r)|^2 = \int_0^{r_c} dr|\phi_l^{AE}(r)|^2. \tag{2.19}$$

The last condition ensures that the scattering properties matches in these two cases. In other words, the wave functions that have the same integrated charge inside a sphere of radius r have the identical energy variation to the first order for their scattering phase shifts at r. Since ϕ^{PS} equals ϕ_l^{AE} at $r > r_c$, the scattering properties of the pseudopotential and all-electron wave functions have the same energy variation at $r > r_c$, too. Thus, the pseudopotential is expected to be transferable in other atomic environments where the external potential has changed.

Satisfying the aforementioned requirements means that a different pseudopotential is needed for each angular momentum. Traditionally, the pseudopotentials are split into a long-ranged local part and a short-ranged semi-local part:

$$\hat{V}_l(\vec{r}) = V_{local}(\vec{r}) + \sum_{lm} |Y_{lm}\rangle \delta V_l(r) \langle Y_{lm}|, \tag{2.20}$$

where V_{local} is a coulomb-like potential that decays as r^{-1}. The second term is a semi-local potential, the radial part of which has a local character, while the angular projections depend on the angular momentum values. The calculation of this type of potential is tedious and time-consuming. A more convenient way was introduced by Kleinman and Bylander [54] to use a non-local form for the pseudopotential:

$$\hat{V}_l(\vec{r}) = V_{local}(\vec{r}) + \sum_{lm} \frac{|\psi_{lm}^{PS} \delta V_l\rangle \langle \delta V_l \psi_{lm}^{PS}|}{\langle \psi_{lm}^{PS} | \delta V_l | \psi_{lm}^{PS} \rangle}, \tag{2.21}$$

where $|\psi_{lm}^{PS}\rangle$ is the atomic pseudo-wavefunction for the reference state. This non-local form is computationally more efficient than the semi-local term. In addition, the formula can be evaluated in either reciprocal space or real space. In the real space calculation, which uses a spherical grid, the matrix elements need to be evaluated only within the core radius r_c. For a larger system, the calculation of the non-local form is faster in real space than in reciprocal space.

2.2.2 Projector Augmented-Wave (PAW) Method

The projector augmented-wave (PAW) method, which unifies the concept of pseudopotential and the augmented-plane-wave (APW) methods was first introduced by Blöchl in 1994[62]. The algorithm of the PAW method divides the wave function in the real space such that the wave function consists of both a partial-wave expansion within an atom-centered sphere and a smooth wave function expanded by plane waves outside the sphere. This atom-centered sphere is referred to as the augmentation region. The projector function which has the partial-wave form is designed to probe the character of the pseudo (PS) wave function inside the augmentation region. In the PAW formulation, the all-electron (AE) wave function is

accessible from the PS wave function through a transformation operator. Therefore, the all electron density is accessible and the accuracy is well-controlled. This method also has a considerable improvement of the former norm-conserving pseudopotentail (NCPP) method in the computational performance. The cut-off energy is around 400 eV for a plane waves convergence, and one or two partial waves per atomic site and angular momentum are sufficient to represent the wave function in the augmentation region.

To generate a PAW wave function, an all-electron self-consistent solution of the Schrödinger-like equation for a reference atom or ion $|\Psi^{AE}\rangle$ is first calculated. It is assumed that the total electron density can be divided into a core electron density and a valence electron density such that the core electrons are assumed to be "frozen" in the same form in the atom as they are in solids. Similar to the pseudopotential method, a pseudo wave function $|\Psi^{PS}\rangle$ is created in the PAW method. This pseudo wave function is equal to the all-electron wave function outside the augmentation region, and is smooth without nodal structures inside the augmentation region. A transformation operator $\hat{T}$ is applied between the two wave functions:

$$|\Psi^{AE}\rangle = \hat{T}|\Psi^{PS}\rangle, \tag{2.22}$$

and the operator by nature is an identity plus a local contribution inside the augmentation sphere:

$$\hat{T} = 1 + \hat{T}_R, \tag{2.23}$$

where $\hat{T}_R$ denotes that an operator operates only around the atom within a radius of R. Inside this region, both wave functions are expanded into a set of partial waves, $|\phi_i\rangle$ where the label i denotes quantum numbers n, l, and m at the atomic site. These partial waves are logarithmic radial functions multiplied with spherical harmonics on radial grids. For each of the AE partial waves, an auxiliary PS partial wave is chosen to satisfy the transformation property:

$$|\phi_i^{AE}\rangle = (1 + \hat{T}_R)|\phi_i^{PS}\rangle. \tag{2.24}$$

A set of projector functions $|p_i\rangle$ are defined such that

$$|\Psi^{PS}\rangle = \sum_i |\phi_i^{PS}\rangle\langle p_i|\Psi^{PS}\rangle, \tag{2.25}$$

with

$$\sum_i |\phi_i^{PS}\rangle\langle p_i| = 1. \tag{2.26}$$

It can be shown by insertion that the relation between projectors and PS partial waves satisfies

$$\langle p_i|\phi_j^{PS}\rangle = \delta_{ij}. \tag{2.27}$$

Note that neither the projectors nor the partial waves need to be orthogonal among themselves. Finally, the transformation described in Eq. 2.23 can be expressed in the form of partial waves and projector functions:

$$\hat{T} = 1 + \sum_i (|\phi_i^{AE}\rangle - |\phi_i^{PS}\rangle)\langle p_i|, \tag{2.28}$$

and the AE wave function can be expressed as the PS wave function plus the AE wave function in the augmentation region, $|\Psi_R^{AE}\rangle$, subtracted by the PS wave function in the same region, $|\Psi_R^{PS}\rangle$:

$$|\Psi^{AE}\rangle \;\; = \;\; |\Psi^{PS}\rangle + |\Psi_R^{AE}\rangle - |\Psi_R^{PS}\rangle, \tag{2.29}$$

with

$$|\Psi_R^{AE}\rangle = \sum_i |\phi_i^{AE}\rangle\langle p_i|\Psi^{PS}\rangle, \tag{2.30}$$

$$|\Psi_R^{PS}\rangle = \sum_i |\phi_i^{PS}\rangle\langle p_i|\Psi^{PS}\rangle. \tag{2.31}$$

Given the constructed basis functions $|p_i\rangle$, $|\phi_i^{AE}\rangle$, and $|\phi_i^{PS}\rangle$ for the reference atoms, we can extend the calculation in the periodic system. For periodic solids, the one-electron eigenstates of the Kohn-Sham Hamiltonian (Eq. 2.12) are represented in the PAW method such that

$$|\Psi_{nk}^{AE}\rangle = |\Psi_{nk}^{PS}\rangle + \sum_i (|\phi_i^{AE}\rangle - |\phi_i^{PS}\rangle)\langle p_i|\Psi_{nk}^{PS}\rangle, \tag{2.32}$$

where the indices n and k stand for a band number and a k-point, respectively. The index i represents the atomic site and the atomic quantum numbers (n,l,m). The pseudo wave function is an envelope function expanded on a plane wave basis set:

$$|\Psi_{nk}^{PS}\rangle = \sqrt{\frac{1}{\Omega}} \sum_{\vec{G}} c_{nk}(\vec{G}) e^{i(\vec{k}+\vec{G})\cdot\vec{r}}, \tag{2.33}$$

with Ω the volume of the unit cell and $\vec{G}$ the reciprocal lattice vectors.

To evaluate the quantity of an operator $\hat{A}$ of the system, we need to calculate the expectation value of the operator:

$$\langle A\rangle = \sum_{n,k} f_n \langle \Psi_{nk}^{AE}|A|\Psi_{nk}^{AE}\rangle, \tag{2.34}$$

where f_n denotes the occupancy of the state n. In the pseudo wave functions representation, the pseudo operator becomes

$$\begin{aligned} \hat{A}^{PS} &= \hat{T}^\dagger \hat{A} \hat{T} \\ &= \hat{A} - \sum_{i,j} |p_i\rangle (\langle \phi_i^{AE}|\hat{A}|\phi_j^{AE}\rangle + \langle \phi_i^{PS}|\hat{A}|\phi_j^{PS}\rangle)\langle p_j|, \end{aligned} \tag{2.35}$$

where the variables i and j represent the atomic index and its quantum numbers n, l, and m for projector and partial wave functions. The expectation value is then reformulated as

$$\begin{aligned}\langle A\rangle &= \sum_{n,k} f_n \langle \langle \Psi_{nk}^{PS} | A | \Psi_{nk}^{PS} \rangle \\ &+ \sum_{i,j} D_{i,j} \langle \phi_i^{AE} | A | \phi_j^{AE} \rangle \\ &- \sum_{i,j} D_{i,j} \langle \phi_i^{PS} | A | \phi_j^{PS} \rangle, \end{aligned} \tag{2.36}$$

with the density matrix

$$D_{i,j} = \sum_{n,k} \langle p_j | \Psi_{nk}^{PS} \rangle f_n \langle \Psi_{nk}^{PS} | p_i \rangle. \tag{2.37}$$

Similar to the wave function, the expectation value in the PAW method is divided into three parts: The quantity of the pseudo wave function in total space, plus a term of projected AE partial-waves in the augmentation region, and minus a projected PS partial-waves in the augmentation region. The completeness relation of the projector-partial wave set described in Eq. 2.27 is then used with the above equation to calculate the total valence charge density. In the same formalism, the total energy, force, and stress of the system can be derived accordingly from the charge density result.

2.3 Atomistic Diffusion in Solids

Atomic diffusion in solids at moderate temperature is known to abide the Arrhenius behavior: The logarithm of the diffusivity varies linearly with respect to the ratio of the diffusion barrier to the thermal energy. When the diffusion barrier is comparatively larger than the thermal energy $k_B T$ (about 25 meV at room temperature), the diffusion process is much slower compared to the atomic vibration in the solid (typically 10^{-13} - 10^{-12} s). In the theoretical modeling, it would be very inefficient to apply a molecular dynamics (MD) method to study this type of process since one would have to wait very long for a single process to happen in the simulation. The transition state theory (TST), which uses a statistical approach, is more appropriate for handling this problem. By definition, the transition state

is a state through which the system has to pass to get to another basin on the potential energy surface (PES). For a multi-dimensional surface, a transition state is a first-order saddle point on the minimum energy path (MEP). TST is essentially a semi-classical theory, which applies classical dynamics along the reaction path and uses quantum statistics along the perpendicular directions to define the state probability [55]. In the Boltzmann distribution, the probability of finding a configuration in a state i (with energy E_i) is proportional to $e^{-E_i/(k_BT)}$. With well-defined approximations, the pre-factor in the Arrhenius equation can be evaluated from the TST within the harmonic approximation. To determine the diffusion rate, the major task is then to calculate the transition state energy. Since a diffusion process usually involves the degrees of freedom of multiple atoms, and it is difficult to visualize the multi-dimensional potential surface to find saddle points, the work requires a sophisticated algorithm to search for saddle points in a reliable and efficient way.

The nudged elastic band method (NEB) is a method to find the minimum energy path (MEP) when both the initial (reaction) and final (product) states are known [61]. The MEP by definition is the path with the highest transition probability (which has the lowest energy saddle point) on the multi-dimensional potential surface. A series of intermediate images between the known initial and final states are chosen as an initial guess of an MEP. Each image i (at position $\vec{r}_i$) is virtually connected by springs with a spring constant of K. The energy of the "band" connecting these images is

$$\mathrm{BAND}(\vec{r}_1, \vec{r}_2, ...\vec{r}_N) = \sum_{i=1}^{N} E(\vec{r}_i) + \sum_{i=2}^{N} \frac{K}{2}(\vec{r}_i - \vec{r}_{i-1})^2, \tag{2.38}$$

where $\mathrm{E}(\vec{r}_i)$ is the total energy of image i. The force on each image consists of two terms which are parallel and perpendicular to the tangential direction of the image, respectively:

$$\vec{F}(\vec{r}_i) \quad = \quad \vec{F}_{\perp}(\vec{r}_i) + \vec{F}_{\parallel}(\vec{r}_i), \tag{2.39}$$

where

$$\vec{F}_{\perp}(\vec{r}_i) = -(\nabla E(\vec{r}_i) - (\nabla E(\vec{r}_i) \cdot \hat{\tau}_i)\hat{\tau}_i) \quad (2.40)$$

$$\vec{F}_{\parallel}(\vec{r}_i) = -(\hat{\tau}_i \cdot \nabla \frac{K}{2}(\vec{r}_{i+1} - \vec{r}_i)^2)\hat{\tau}_i, \quad (2.41)$$

with the unit vector of the tangential direction of image i as

$$\hat{\tau}_i = \frac{\vec{r}_{i+1} - \vec{r}_i}{|\vec{r}_{i+1} - \vec{r}_i|}. \quad (2.42)$$

The forces are updated iteratively with a geometry optimization.

Convergence is reached when the perpendicular force $\vec{F}_{\perp}$ becomes zero. The parallel force $\vec{F}_{\parallel}$ is to prevent the images from sliding down towards two minimum points. After convergence is reached, an adaptive force is applied to the image having the highest energy $E(\vec{r}_{i_{max}})$:

$$\vec{F}(\vec{r}_{i_{max}}) = -\nabla E(\vec{r}_{i_{max}}) + 2(\nabla E(\vec{r}_{i_{max}}) \cdot \hat{\tau}_{i_{max}})\hat{\tau}_{i_{max}} \quad (2.43)$$

such that the direction of the force is towards an even higher energy state on the MEP. This approach is known as the climbing image adaptation in the NEB method [66].

CHAPTER III

HELIUM INSIDE PALLADIUM

In many areas of nuclear reactor technology, a topic of considerable importance is the storage of the hydrogen isotope, tritium (^{3}H or T), in metals. One of the major problems for storing tritium is that ^{3}H, which has a half-life of 12.3 years, decays into an electron and a ^{3}He atom inside the metal lattice:

$$^3\mathrm{H} \rightarrow \bar{\nu}_e + \mathrm{e}^- + {}^3\mathrm{He} + 18.6 \text{ keV}. \tag{3.1}$$

The chemically inert He atoms consequently aggregate, leading to a build-up of He nano clusters which damages the physical integrity of the original metal tritides and its storage functionality. It is desirable to understand the mechanism of He cluster formation in metal tritides and, in turn, to elongate the storage lifetime.

As a prototype material for hydrogen (and hydrogen isotope) storage, palladium (Pd) and palladium hydrides have been studied extensively in the past. There are many advantages to use palladium as a storage material. Palladium, which exhibits fast kinetics for absorption and desorption of hydrogen, is resistant to oxidation and poisoning in the environment. In addition, palladium tritide is able to retain He atoms for more than ten years [2, 26].

In this chapter, we use first-principles calculations to study the structure and energetics of interstitial helium clusters inside bulk palladium with and without a lattice vacancy. The site preference and diffusion barrier of one helium atom passing through the interstitial region are calculated. The results are compared with the Pd-H system [77, 71]. Since the electronic interaction for ^{1}H in metals is the same as that for ^{3}H within the standard Born-Oppenheimer approximation, we will use hydrogen in the calculation for all the hydrogen isotopes except for the evaluation of the zero-point energy [65]. We find that interstitial helium atoms favor grouping at nearest octahedral sites and that five helium atoms can spontaneously produce a Frenkel defect with a self-interstitial Pd atom. The formation of

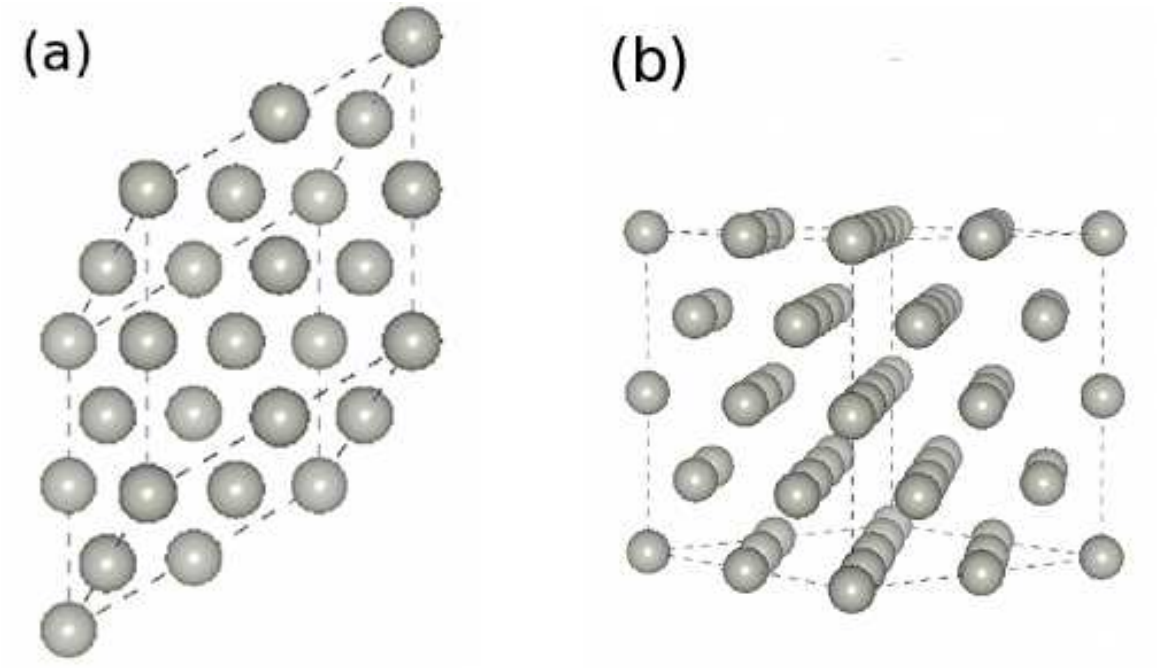

Figure 3.1: (a) Primitive 2x2x2 supercell and (b) conventional 2x2x2 supercell for a face-centered cubic (fcc) lattice.

He clusters in the presence of a vacancy is also investigated. Finally, the cluster growth mechanism is discussed based on the atomistic process examined in this study.

3.1 Computational Methods

Our calculations are performed within the Density-Functional Theory (DFT) formalism using the Vienna *ab initio* Simulation Package (VASP) [69, 60]. The plane-wave basis set is used to solve the Kohn-Sham equations, and the Blöchl's projector augmented wave (PAW) method [62] is employed to better describe the valence-core interaction than the traditional pseudopotential methods. The exchange and correlation functional follows the

Table 3.1: Binding energies, in units of eV, for interstitial H and He atoms as a function of the supercell size m of Pd, showing the convergence of the calculation. The supercells of m=4 and 32 are conventional cubic cells, while those of m=8 and 64 are derived from the primitive cell.

m	4	8	32	64
E^f(H)	-0.08	-0.10	-0.14	-0.14
E^f(He)	4.51	4.01	3.65	3.68

generalized gradient approximation (GGA) by Perdew and Wang[63]. The total energy convergence is within 5 meV per atom with respect to the plane wave energy cutoff and the number of Monkhost-Pack k-points [58] in the Brillouin zone. In this study, the cutoff energy used is 500 eV, and the grid sampling is within 0.01 $\AA^{-1}$. In addition, we employ the supercell approach with periodic boundary conditions and all the calculations are done at the same lattice constant as in the pure Pd bulk with all atomic positions fully relaxed in the supercell. Fig. 3.1 illustrates the unit cells of the supercells with different size. Unless explicitly specified in the text, we use the supercell of 32 Pd atoms in most of the study, which meets the desired accuracy with reasonable computational cost. The convergence test for the cohesive energy of the $Pd_{32}He$ system is shown in Fig. 3.2.

The binding energy of an H impurity defect inside the Pd lattice is evaluated with respect to the energies of bulk Pd and the H_2 molecule (without the zero-point energy):

$$E^b(\mathrm{H}) = E(\mathrm{Pd}_m\mathrm{H}) - mE(\mathrm{Pd}) - \frac{1}{2}E(\mathrm{H}_2), \tag{3.2}$$

where m is the size of the Pd supercell. $E(H_2)$ is the total energy obtained by placing a H_2 molecule in a supercell with a large enough lattice constant and considering only the Gamma point in the Brillouin Zone. E(Pd) is the energy per atom of bulk Pd. On the other hand, the binding energy of a helium impurity defect is evaluated with respect to the energies of bulk Pd (without the zero-point energy) and a free He atom:

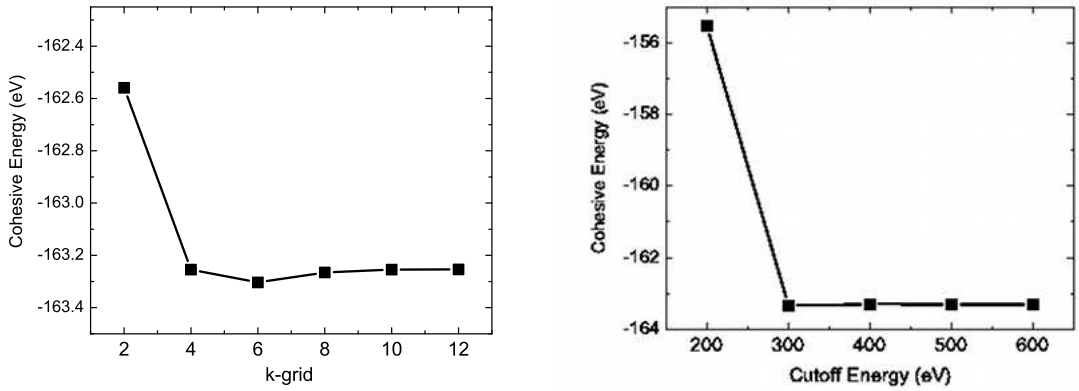

Figure 3.2: Convergence of the cohesive energy with respect to the k-grid and the cutoff energy. Here we plot the cohesive energy of $Pd_{32}He$ as an example.

$$E^b(\mathrm{He}) = E(\mathrm{Pd}_m\mathrm{He}) - mE(\mathrm{Pd}) - E_{\mathrm{atom}}(\mathrm{He}). \tag{3.3}$$

The calculated binding energies for different values of m are listed in Table 3.1, showing a good convergence for a single impurity at $m = 32$. The formation energy of a Pd vacancy defect is defined as follows:

$$E_{\mathrm{vac}} = E(\mathrm{Pd}_{m-1}) - (m-1)E(\mathrm{Pd}). \tag{3.4}$$

The electronic properties, including the density of states and the electronic density change, are analyzed to examine the hydrogen and helium interaction with the metal. To obtain the electronic density change due to the presence of the hydrogen or helium impurities inside the palladium supercell, the charge density of the entire system is subtracted by the sum of the charge density for both the host metal and the interstitial atom:

$$\Delta\rho = \rho(\mathrm{Pd}_m\mathrm{X}) - \rho(\mathrm{Pd}_m) - \rho(\mathrm{X}), \tag{3.5}$$

where X represents either H or He. $\rho(\mathrm{Pd}_m)$ is the charge density of the Pd_m supercell in which all the palladium atoms are frozen at the same positions as those in $\mathrm{Pd}_m\mathrm{X}$, but with the impurity X removed. In this calculation, the isosurface of the charge density change provides direct real-space visualization of the rearrangement of the local electronic density due to the presence of a hydrogen or a helium atom.

To investigate the minimum-energy path and the transition state for the diffusion of interstitial atoms, the Nudged Elastic Band (NEB) method is applied [61]. The NEB method is known to provide a reliable way to find the minimum-energy path when the initial and final states of a process are known. Linearly interpolated atomic configurations between the initial and final positions are connected by springs and relaxed simultaneously to provide the minimum-energy path. All the configurations are relaxed until the maximum force acting on an atom is less than $0.01eV/\mathring{A}$. The relaxation is followed by the image climbing method [66]. Using this approach, the configuration with the highest energy in

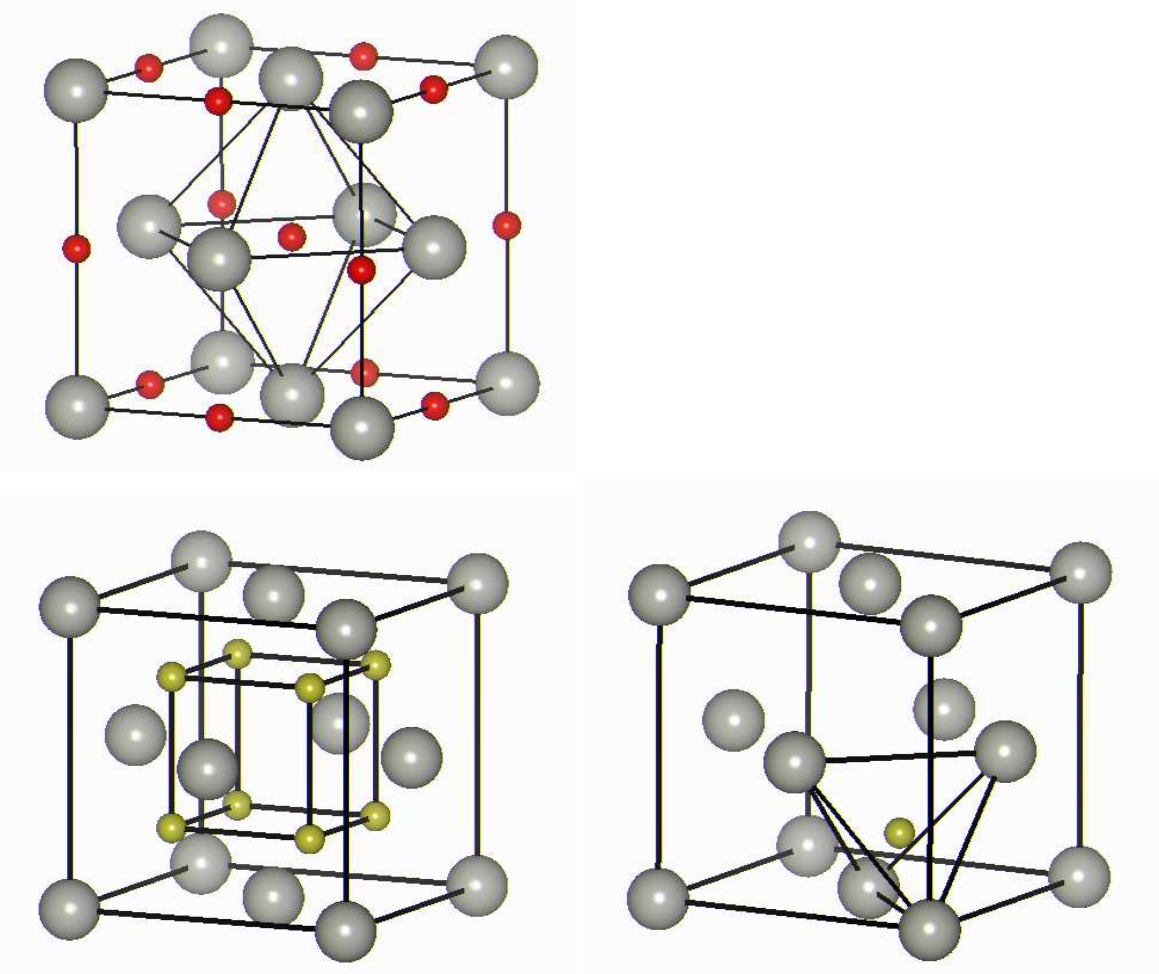

Figure 3.3: Two types of interstitial sites in an fcc Pd lattice. The octahedral sites (red), which are the geometric center of six Pd atoms, form an fcc lattice themselves. The tetrahedral sites (yellow), which are the geometric center of four Pd atoms, form a simple cubic lattice.

the original set of images is used to search for the saddle point along the path in order to determine the diffusion energy barrier.

3.2 Diffusion of Interstitial Atoms

In the face-centered cubic (fcc) Pd lattice, two types of interstitial sites exist: the octahedral and tetrahedral sites, as illustrated in Fig. 3.3. They are the geometric centers of six and four palladium atoms, respectively. Fig. 3.4 shows the potential energy variation for a helium atom in the interstitial region, which is calculated on a real-space grid with the host metal atoms fixed. The results are compared with the hydrogen case in Fig. 3.5.

The potential energy plots illustrate valleys (energy minima), hilltops (energy maxima) and possible passes (saddle points, the transition states) that a hydrogen or helium atom may diffuse from one interstitial site to another. As a result, hydrogen and helium atom have a similar energy distribution in the interstitial region. The site preference is the octahedral over the tetrahedral site, and the minimum energy path of the migration between the octahedral sites is through the nearest tetrahedral site along the $\langle 111 \rangle$ direction in both cases.

The activation energy of the diffusion is calculated in two ways. One is to relax every Pd atom in the system at each intermediate state along the diffusion path. The relaxation is implemented by the nudged elastic band method, in which both the fully-relaxed initial state and the final state are calculated beforehand. Eight linearly-interpolated images between the two states are allowed to relax with the algorithm described in the previous section. The other method is to start from the fully-relaxed energy minima, and to place the hydrogen or helium atom along the diffusion path with the rest of the metal atoms frozen at the initial positions. These two results are presented in Fig. 3.6 for hydrogen and helium atoms, respectively. The data points denoted by circles (stars) correspond to the energies of the intermediate configurations with all the metal atoms relaxed (fixed). The results indicate that the lattice relaxation plays a significant role on the calculated properties. In particular for helium, the diffusion barrier is found to be lowered by 0.77 eV when palladium atoms are fully relaxed during the diffusion. In addition, the local Pd displacements, as shown

Table 3.2: Calculated forces and lattice distortion for H and He impurities at the octahedral (O) and tetrahedral (T) sites in Pd. The force exerted by the impurity atom on the nearest and next-nearest neighboring Pd atoms in an unrelaxed lattice is denoted by F_1 and F_2, respectively. After relaxation, the displacement u_1 of the nearest-neighbor Pd atoms is also listed.

	H		He	
	O site	T site	O site	T site
F_1 (eV/Å)	0.35	1.36	1.90	3.66
F_2 (eV/Å)	0.12	0.11	0.12	0.18
u_1 (Å)	0.02	0.07	0.16	0.25

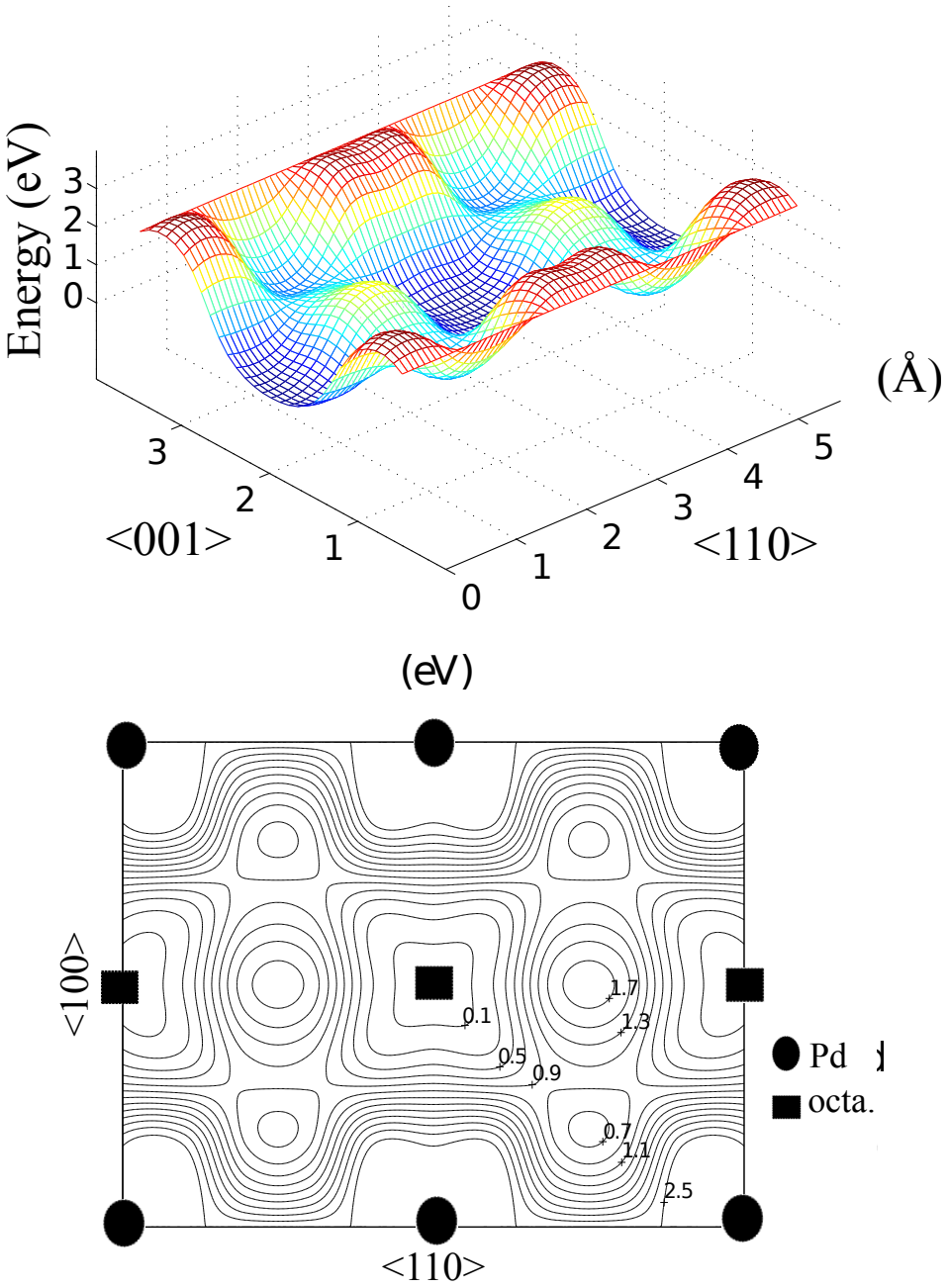

Figure 3.4: The potential energy variation and the energy contour plot for a He atom in the interstitial region on the Pd (110) plane. The energy zero is set at the octahedral site. The potential value is truncated at 2.5 eV to avoid showing high potential regions near the Pd atoms.

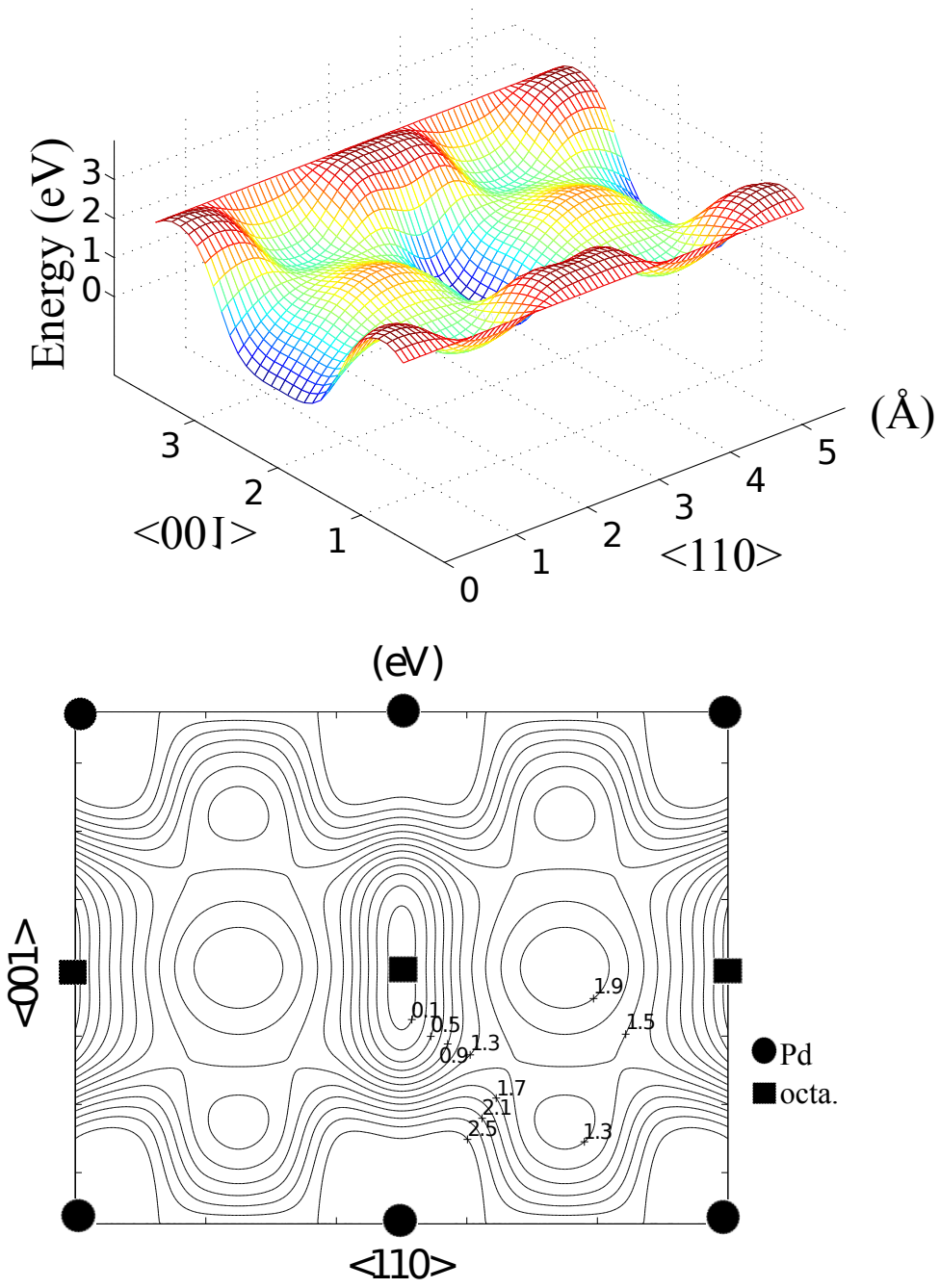

Figure 3.5: The potential energy variation and the energy contour plot for a H atom in the interstitial region on the Pd (110) plane. The energy zero is set at the octahedral site. The potential value is truncated at 2.5 eV to avoid showing high potential regions near the Pd atoms.

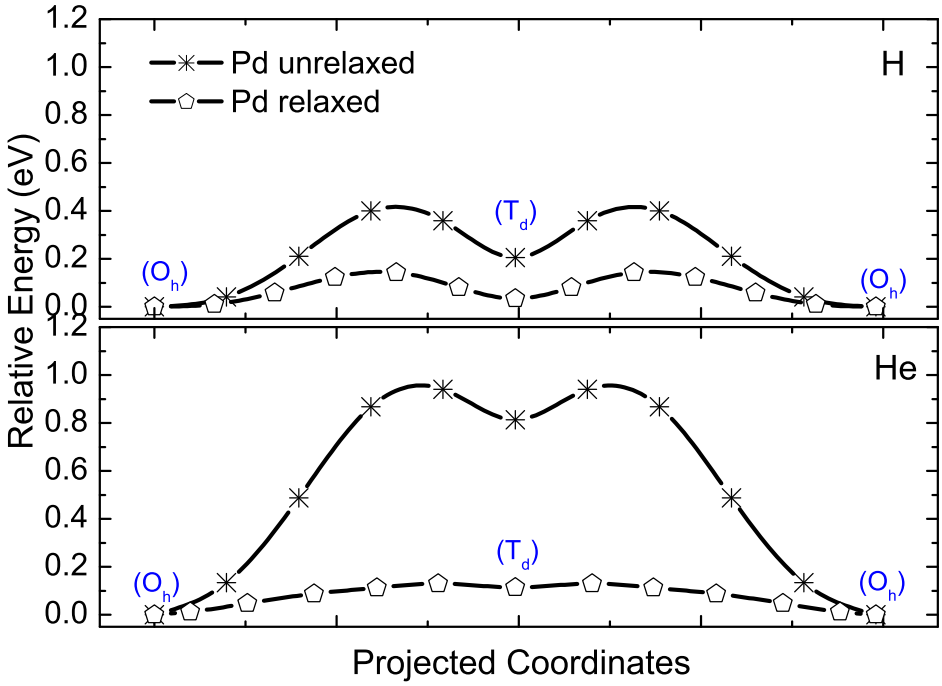

Figure 3.6: Diffusion energy barrier on the (110) plane for the path from an octahedral site to a metastable tetrahedral site along the ⟨111⟩ direction. The result shown is for a H (top) or a He (bottom) atom in a Pd_{32} supercell. The energy zero is set at the octahedral site.

in Table 3.2, are larger around the octahedral helium than those around the octahedral hydrogen [78]. As a result, taking into account proper metal lattice relaxations is necessary to obtain accurate diffusion properties for helium in the metal.

We next examine the zero-point energy (ZPE) corrections to the activation energies of light interstitial atoms from localized vibrations [74]. At each binding site, we numerically estimate the dynamical matrix for the Born-Oppenheimer potential energy surface by creating a small displacement and calculating the second derivative of the energy. It turns out that the ZPE correction has a relatively bigger effect on the diffusion activation energy of ^{1}H and ^{3}H than on that of ^{3}He. The energy barriers for ^{1}H, ^{3}H, and ^{3}He are increased by 0.09 eV, 0.06 eV and 0.01 eV, respectively. Table 3.3 summarizes the results for the binding energies of different interstitial species at the O site, the energy difference between the T

and O sites, and the corresponding diffusion barrier. The results are compared to those with the ZPE corrections.

For helium diffusion in metals at ambient or higher temperature, we did not consider quantum tunneling effect, which is significant for light particles, like hydrogen, diffusion in metals at very low temperature [70].

3.3 Electronic Properties

Further understanding of how helium and hydrogen atoms interact with the palladium metal can be obtained by studying their electronic structures. In Fig. 3.7, the angular-momentum-projected density of states (DOS) are compared between the hydrogen and helium cases when they are located at the O site in the palladium supercell. The solid line represents the projected DOS for the interstitial hydrogen or helium and its nearest neighboring palladium atom, while the dashed line denotes that for pure palladium in the bulk. The energy is referenced to the Fermi energy (E_f) of the system. For hydrogen, the s orbital hybridizes with palladium s, p and d orbitals at the vicinity of -7 eV, and the states near to the E_f are hardly changed. In contrast, the helium impurity, with its $1s$ state at -15 eV, exhibits slightly populated excited states due to the interaction with the palladium d orbital near the Fermi level. The occupation of the excited states outside the closed shell results in an energy increase for the helium atom at the interstitial site in Pd compared with its atomic state. In addition, the states at the palladium site next to helium atom are slightly modified compared to those in pure palladium, possibly due to the noticeable

Table 3.3: Binding energy, E^b, for ^{1}H, ^{3}H, and He at the octahedral (O) site and the tetrahedral (T) site in the Pd lattice. The activation energy, E^a, is calculated from the the difference between the energy at the transition state and at the octahedral site. The values in parentheses are the energies with the zero-point energy corrections included.

	E^b		E^a
(eV)	O site	T site	
^{1}H	-0.06 (-0.16)	-0.01 (0.00)	0.15 (0.24)
^{3}H	-0.06 (-0.20)	-0.01 (-0.09)	0.15 (0.21)
^{3}He	3.60 (3.68)	3.73 (3.81)	0.13 (0.14)

displacements of these Pd atoms induced by the presence of the helium atom.

The contour plots of the charge density change ($\Delta\rho$ defined in Eq. 3.5) when adding a hydrogen or a helium atom to the O site are shown in Fig. 3.8, in which the positions of Pd, He and H atoms are labeled. The contour lines of positive and negative values describe the electron accumulation and depletion, respectively. The presence of interstitial hydrogen pulls a noticeable amount of electrons from surrounding palladium, which corresponds to the DOS plot that new Pd states appear at the lower energy region of the hydrogen orbital. However, the charge density changes due to the presence of a helium atom show that the interstitial helium pushes away a portion of the charge at the interstitial site, which is subsequently transferred to the nearby Pd sites. Part of the interstitial electrons inevitably remain at the helium site, filling the higher-energy $2s$ state near the Fermi level. These characteristics demonstrate that helium and hydrogen interact with the Pd metal in an opposite way.

3.4 He Clusters in Vacancy-Free Pd

The formation of a helium cluster in the vacancy-free system is affected by two factors. One is the mobility of the interstitial helium atom, which is connected with the probability of aggregation of the impurities. The other is the strength of the strain field generated by helium clusters, which affects the process of trapping additional helium atoms. In addition to the diffusion barrier, which we have calculated previously to estimate the mobility of the He atom, the induced strain field and energetics of helium clusters up to seven helium atoms in the interstices of the fcc Pd lattice are evaluated in this section. We model the growth of a helium cluster by introducing one helium atom at a time to the nearest octahedral site of the cluster, followed by fully relaxing the structure. When multiple nearest-neighbor octahedral sites exist, different geometries are tested in order to search for the minimal energy structure.

The binding energy of a cluster of size n is calculated with respect to the reference state of a pure palladium supercell and n isolated interstitial helium atoms:

$$E^b(\mathrm{Pd}_{32}\mathrm{He}_n) = E(\mathrm{Pd}_{32}\mathrm{He}_n) - 32\ E(\mathrm{Pd}) - n\ E_i(He), \tag{3.6}$$

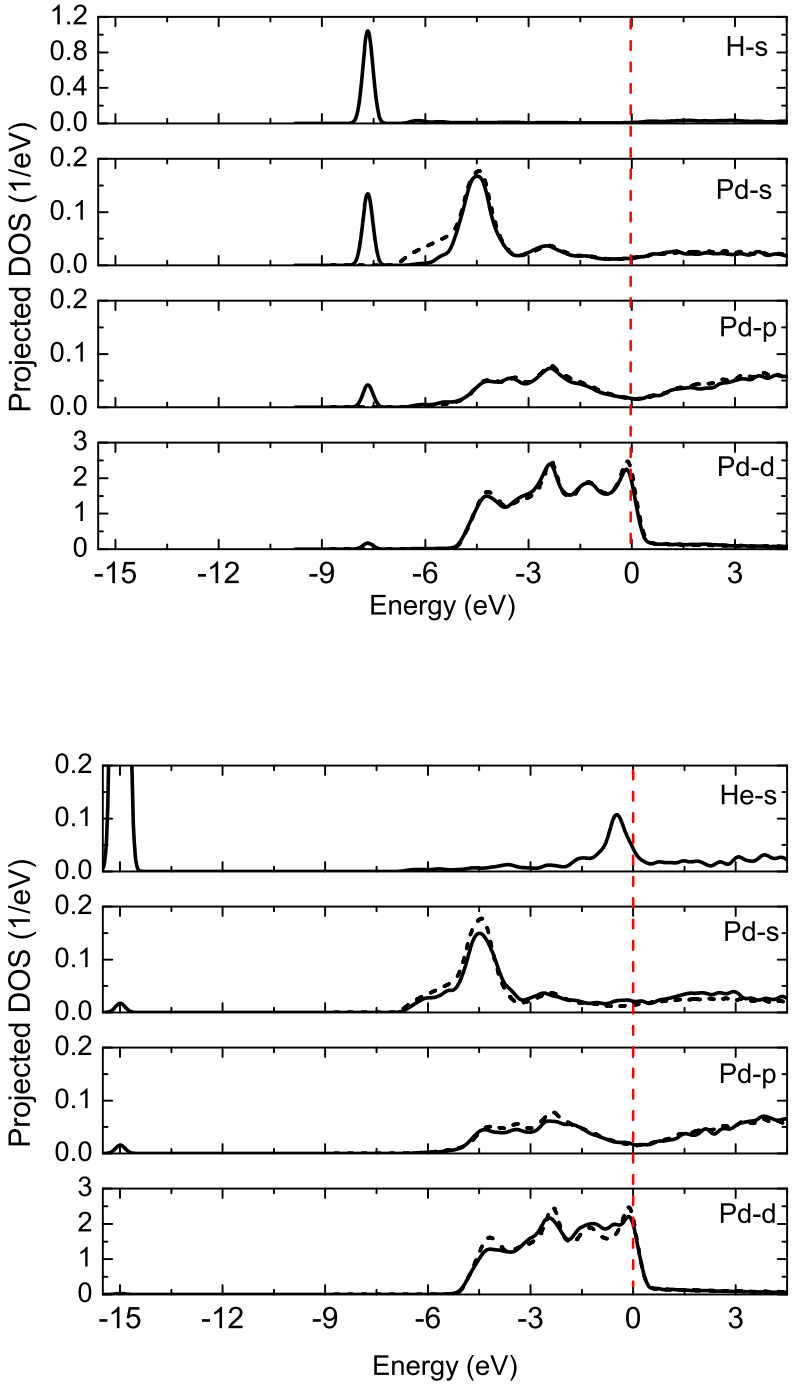

Figure 3.7: Angular-momentum-projected density of states for the s orbital of H and He at the octahedral site and the s, p, and d orbitals of the nearest-neighbor Pd in $Pd_{31}H$ (top) and $Pd_{31}He$ (bottom). The dashed lines represent the DOS of the pure Pd bulk. The Fermi energy level is set to zero.

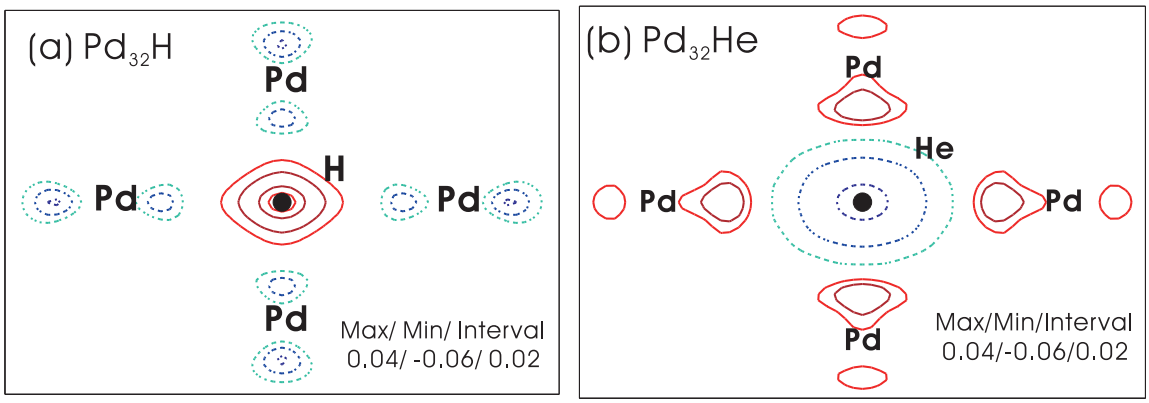

Figure 3.8: The charge density change in the (100) plane due to the presence of H and He impurities at the octahedral site. Solid (dashed) contours represent electron accumulation (depletion) regions. The contour interval is 0.02 electrons / $\mathring{A}^2$.

where

$$E_i(He) = E(\mathrm{Pd_{32}He}) - 32\ E(\mathrm{Pd}). \tag{3.7}$$

And the atomic attachment energy of an n-atom cluster is defined as the energy difference between an n-atom cluster and the combination of an (n-1)-atom cluster and an isolated interstitial helium. It is equivalent to calculating the binding energy difference between the two clusters:

$$E^{Attach}(\mathrm{Pd_{32}He}_n) = E^b(\mathrm{Pd_{32}He}_n) - E^b(\mathrm{Pd_{32}He}_{n-1}). \tag{3.8}$$

The results are listed in Table 3.4. A negative value indicates that it is energetically favorable for the cluster to grow.

The structural configurations of He clusters in the host metal matrix are illustrated in Fig. 3.9. The He dimer favors a dumbbell structure along the $\langle 110 \rangle$ direction between two adjacent octahedral sites. The separation between two He atoms is 1.71 Å, which is comparatively smaller than the octahedral to octahedral distance in the palladium lattice (2.80 $\mathring{A}$). In the trimer, the third atom goes to the common nearest-neighbor O site to the two helium atoms in the dimer. The fourth atom is incorporated by forming a tetrahedron. When the number of helium atoms reaches five or more, the clustering automatically generates a Frenkel defect: a self-interstitial Pd atom and a vacancy defect to accommodate the cluster. The structure consequently serves as a core to trap additional He atoms with

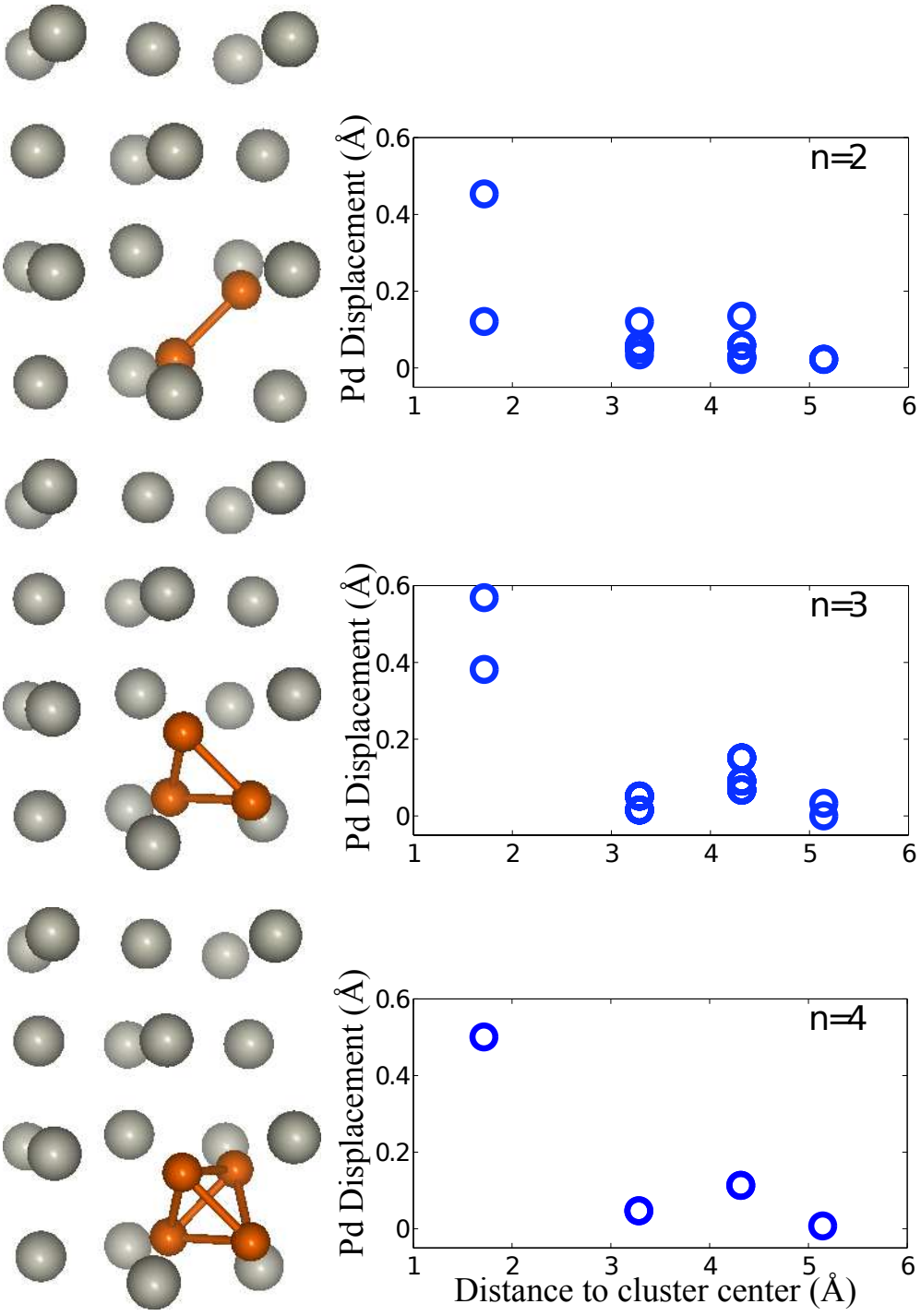

Figure 3.9: The structures of interstitial He clusters of 2, 3, and 4 atoms in the $Pd_{32}He_n$ system. The large (gray) and small (orange) spheres denote Pd and He atoms, respectively. The right panel shows the corresponding Pd displacements. The circles represent the Pd displacement as a function of the distance to the cluster center.

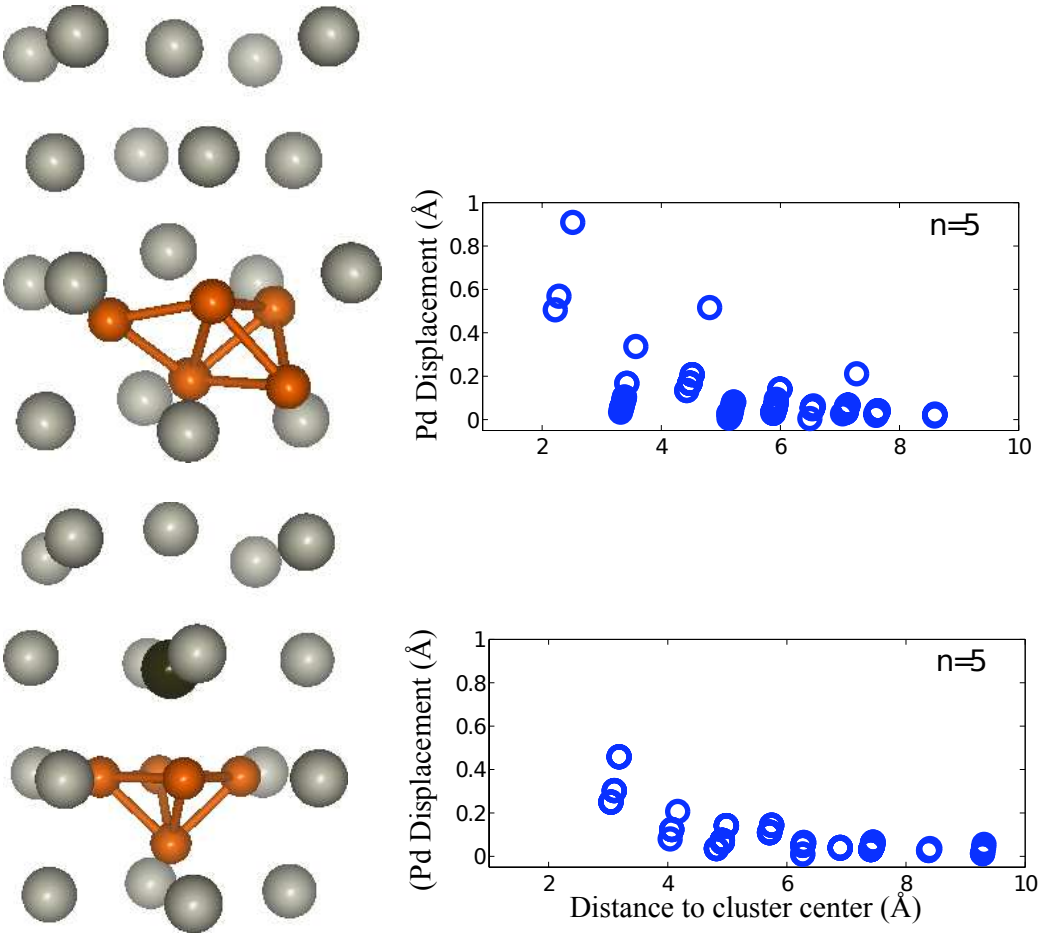

Figure 3.10: The structures of interstitial He clusters of five atoms without and with creation of a self-interstitial atom (indicated by dark color). The large (gray) and small (orange) spheres denote Pd and He atoms, respectively. The right panel shows the corresponding Pd displacements. The circles represent the Pd displacement as a function of the distance to the cluster center.

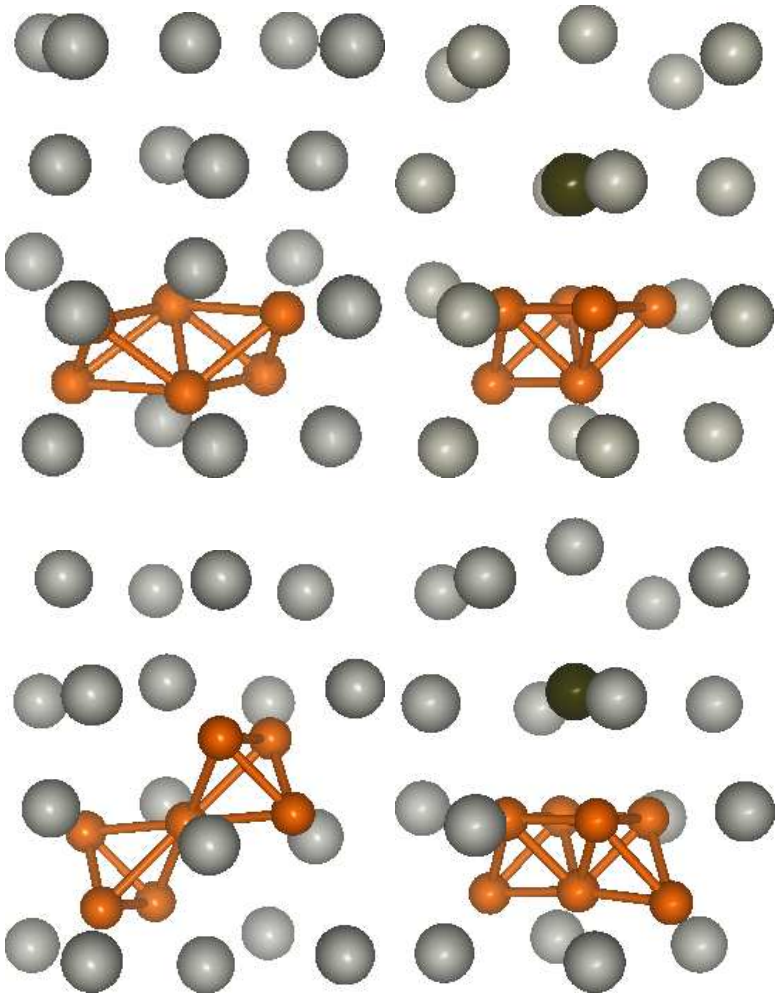

Figure 3.11: The structures of He clusters of 6 and 7 atoms around a Pd-vacancy after the creation of an interstitial Pd atom (indicated by dark color). The large (gray) and small (orange) spheres denote the matrix of Pd atoms and the He atoms, respectively.

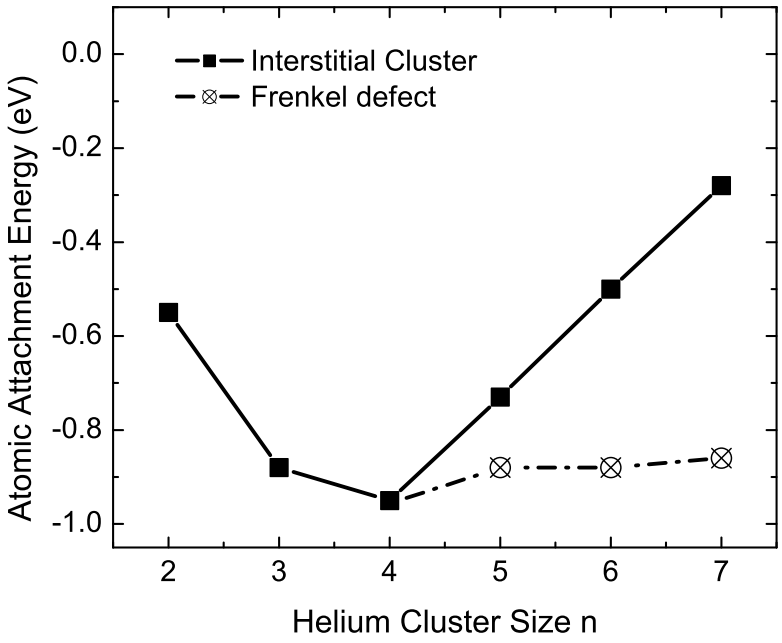

Figure 3.12: Atomic attachment energy as a function of He cluster size n (see text). The solid line corresponds to cluster formation without creating a Pd-vacancy. The dash-doted line corresponds to cluster formation accompanied by generating a self-interstitial Pd and a vacancy, starting at $n = 5$.

a favorable atomic attachment energy. The structure of He clusters of five, six and seven atoms around a Pd-vacancy is shown in Fig. 3.10. Fig. 3.12 presents the atomic attachment energy as a function of cluster size n. The solid and dash-dotted lines represent the configurations with no self-interstitial atom and with self-interstitial atom, respectively. More about He clusters at a vacancy site will be discussed in the next section.

The variation of the atomic attachment energy as a function of cluster size contains three types of contributions: the He-Pd interaction, the Pd strain, and the He-He interaction. The He-He interaction is minimal compared to the other two interactions in the energy scale. In Figs. 3.9 and 3.10, the palladium displacement as a function of the distance to the He cluster center is also plotted to the right of each cluster structure. Each circle represents the Pd displacement in the matrix. The x-coordinate represents the distance of each Pd atom to the symmetric center of defects. The center is chosen at a tetrahedral site for the interstitial clusters and the center is set at the Pd vacancy site when a Pd self-interstitial is formed. It is possible to have multiple Pd atoms corresponding to the same data point due to the symmetry of the cluster structure.

In addition to considering the atomic attachment energy discussed above, the growth of the helium cluster can be further examined by exploring the diffusion path of the interstitial helium atom from an isolated interstitial site to the strained core, which could be an existing atom or cluster. Fig. 3.13 illustrates two of such diffusion paths in a $Pd_{32}He_2$ system. A helium atom will be attracted to the nearest octahedral site of the existing interstitial

Table 3.4: The energetics of the interstitial helium cluster of n atoms in the supercell Pd_{32}. E^b and E^{Attach} are defined in Eq. 3.6 and Eq. 3.8, respectively. The value in parenthesis indicates the results with a Frenkel defect.

n	E^b (eV)	E^b / n (eV)	E^{Attach} (eV)
2	-0.55	-0.28	-0.55
3	-1.43	-0.48	-0.88
4	-2.38	-0.60	-0.95
5	-3.12 (-3.27)	-0.62 (-0.65)	-0.73 (-0.88)
6	-3.62 (-4.14)	-0.60 (-0.69)	-0.50 (-0.88)
7	-3.90 (-5.01)	-0.56 (-0.72)	-0.28 (-0.86)

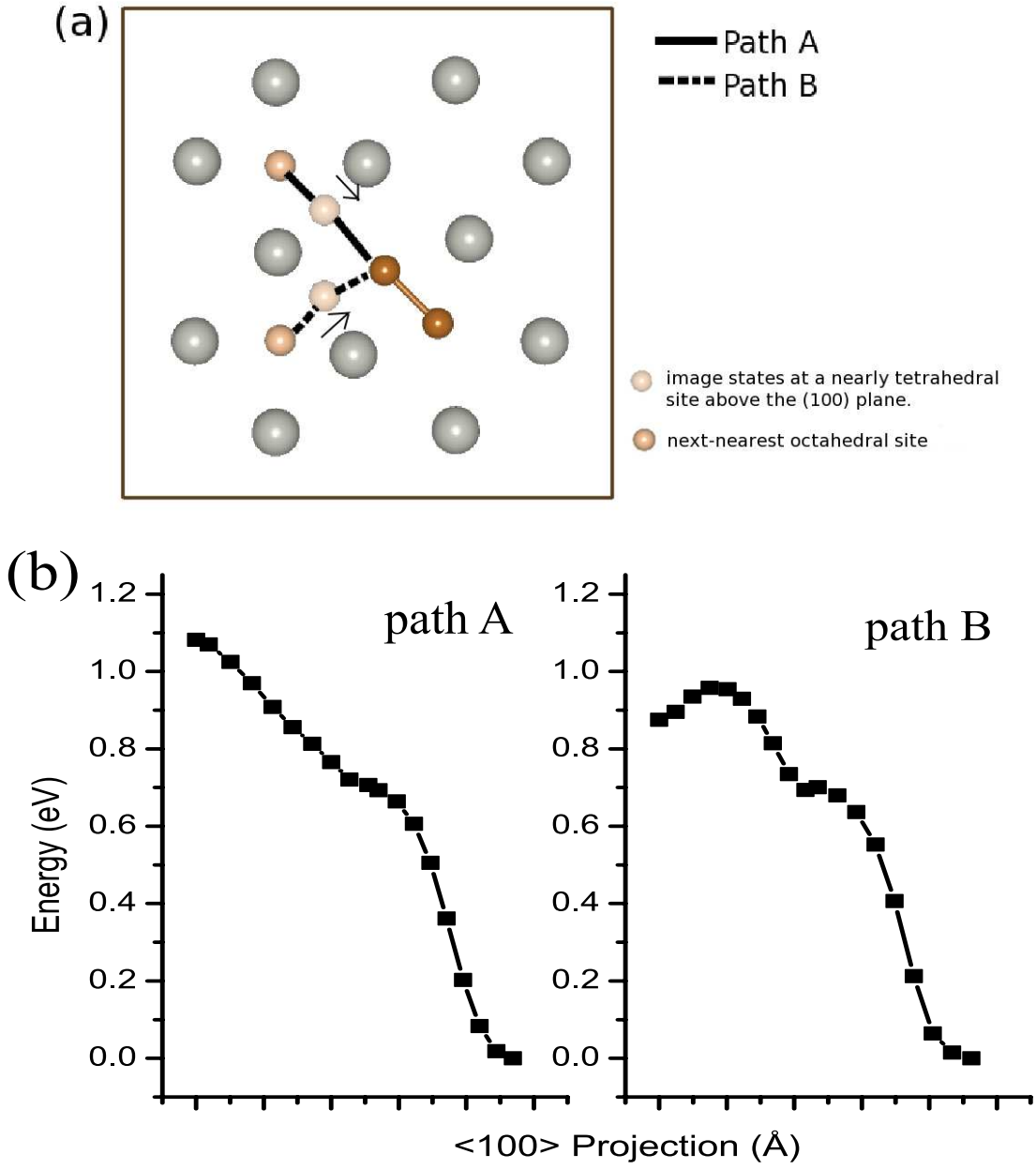

Figure 3.13: (a) Illustration of two diffusion paths projected on the (100) plane for an interstitial He atom being trapped by an existing interstitial He to form a dimer. (b) Calculated diffusion energy along paths A and B using the nudged elastic band method.

helium, and the potential energy along the path is calculated using the nudged elastic band method. Two initial states are investigated: one with the second helium atom located at the third nearest-neighbor octahedral site along the ⟨110⟩ direction with respect to the existing interstitial helium (path A), and the other with a helium atom placed at the second nearest-neighbor O site along the ⟨100⟩ direction (path B). Both paths result in the same final state of a He dimer. The diffusion paths for this clustering process have a lower diffusion barrier compared to that for a normal interstitial helium atom (0.12eV). The diffusion barriers along path A and path B are found to be 0.00 eV and 0.06 eV, respectively.

3.5 He Clusters at a Single Vacancy in Pd

When a Pd-vacancy is generated, the potential energy variation around the vacancy site for hydrogen is very different from that for helium. The calculated results on the (110) plane centered by a Pd-vacancy are shown in Fig. 3.14 and Fig. 3.15. The minimum position for hydrogen is shifted from the octahedral site to the strayed tetrahedral (T′) position. The H atom interacts with the dangling electrons of the surrounding Pd atoms around the vacancy site. On the other hand, the chemically inert He atom, whose minimum energy position is located at the vacancy center, hardly interact with neighboring Pd atoms. In addition, the potential well depth that traps the substitutional He atom is substantial, while that for the H atom is less significant. The jiggling surface at the truncating edge in Fig. 3.14 and Fig. 3.15 is an artifact due to the interpolation between the sharp uphill energy region and the flat truncated energy surface. The energy values are truncated at 2.5 eV and 5.0 eV for H and He, respectively.

The projected DOS for hydrogen or helium near a Pd-vacancy site is also evaluated. In Fig. 3.16, the DOS of the palladium atom next to the lattice vacancy without the presence of a H or He atom (dashed line) is compared with that with the presence of hydrogen or helium at the vacancy site (solid line). The hydrogen atom located near the T site shows a strong hybridization with Pd orbitals [80]. However, the 1s state of the helium atom hardly interacts with the surrounding palladium states. As a result, the binding energy for the He atom located at the vacancy center is lowered mainly due to the space made available by

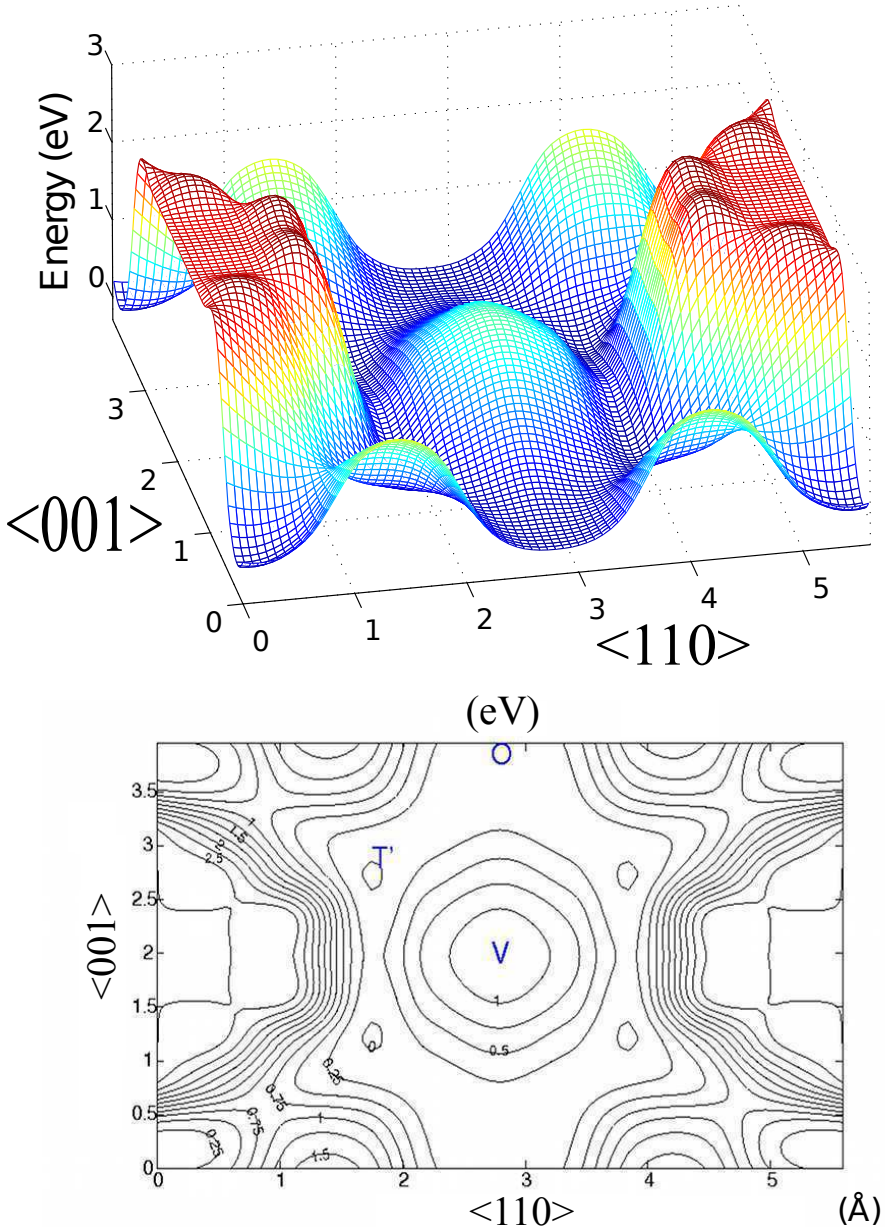

Figure 3.14: The potential energy variation and the energy contour plot for an H atom near a Pd-vacancy site on the (100) plane. The energy zero is set at the shifted tetrahedral site (T′) next to the vacancy. The energy value is truncated at 2.5 eV in order to illustrate the energy variation near the vacancy. The jiggling surface at the truncated edge is the result of the interpolation method.

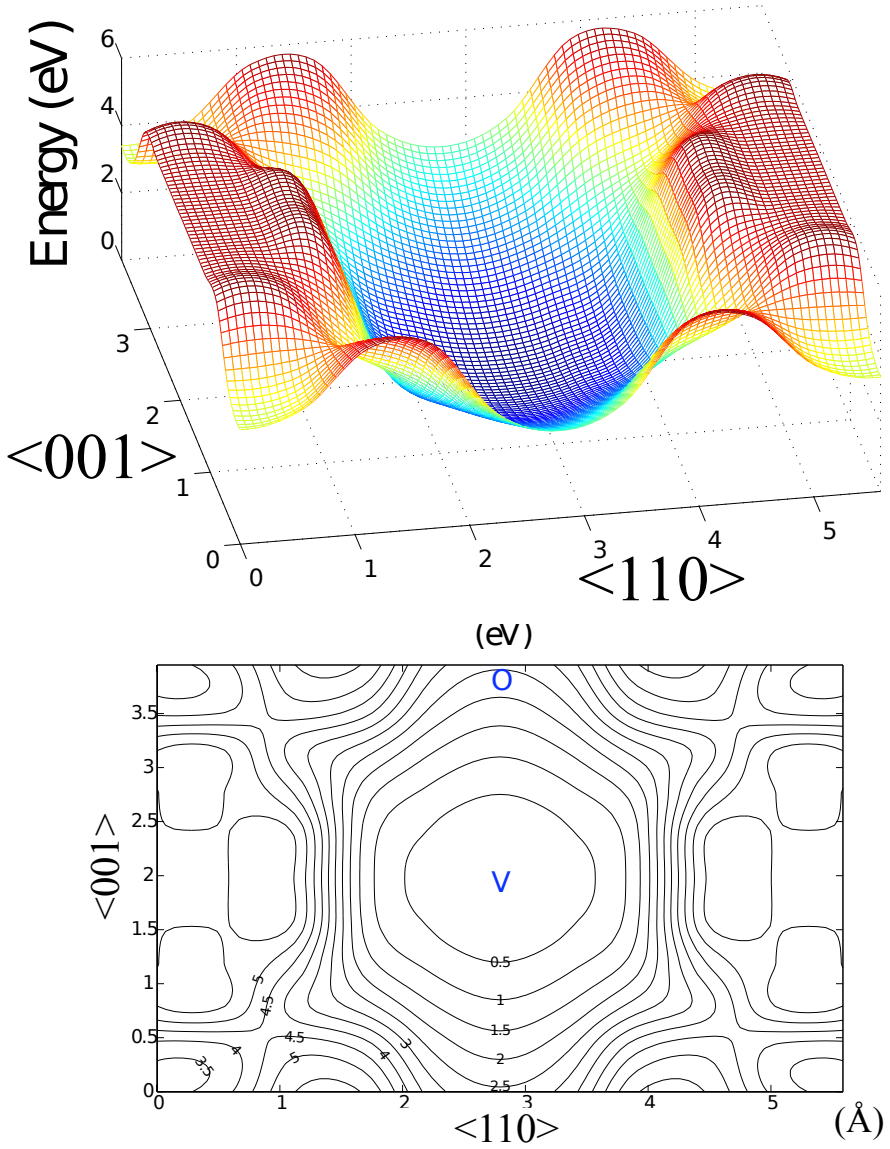

Figure 3.15: The potential energy variation and the energy contour plot for a He atom near a Pd-vacancy site on the (100) plane. The energy zero is set at the vacancy center. The energy value is truncated at 5.0 eV in order to illustrate the energy variation near the vacancy. The jiggling surface at the truncating edge is the result of the interpolation method.

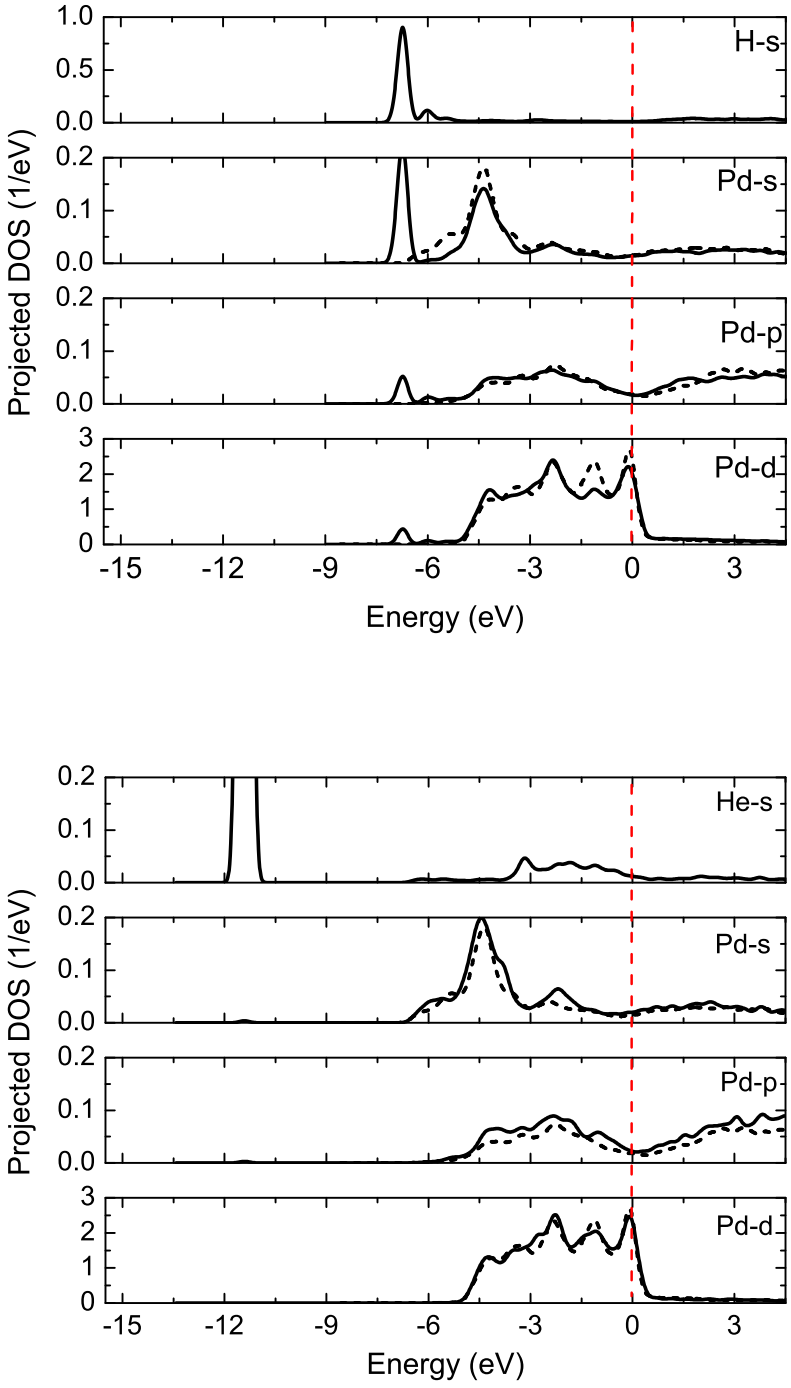

Figure 3.16: Angular-momentum-projected density of states for the s orbital of H and He at the vacancy site and the s, p, and d orbitals of the nearest-neighbor Pd in $Pd_{31}H$ (top) and $Pd_{31}He$ (bottom). The dashed lines represent the DOS of the Pd atom next to the vacancy defect without the presence of hydrogen or helium impurities. The Fermi energy level is set to zero.

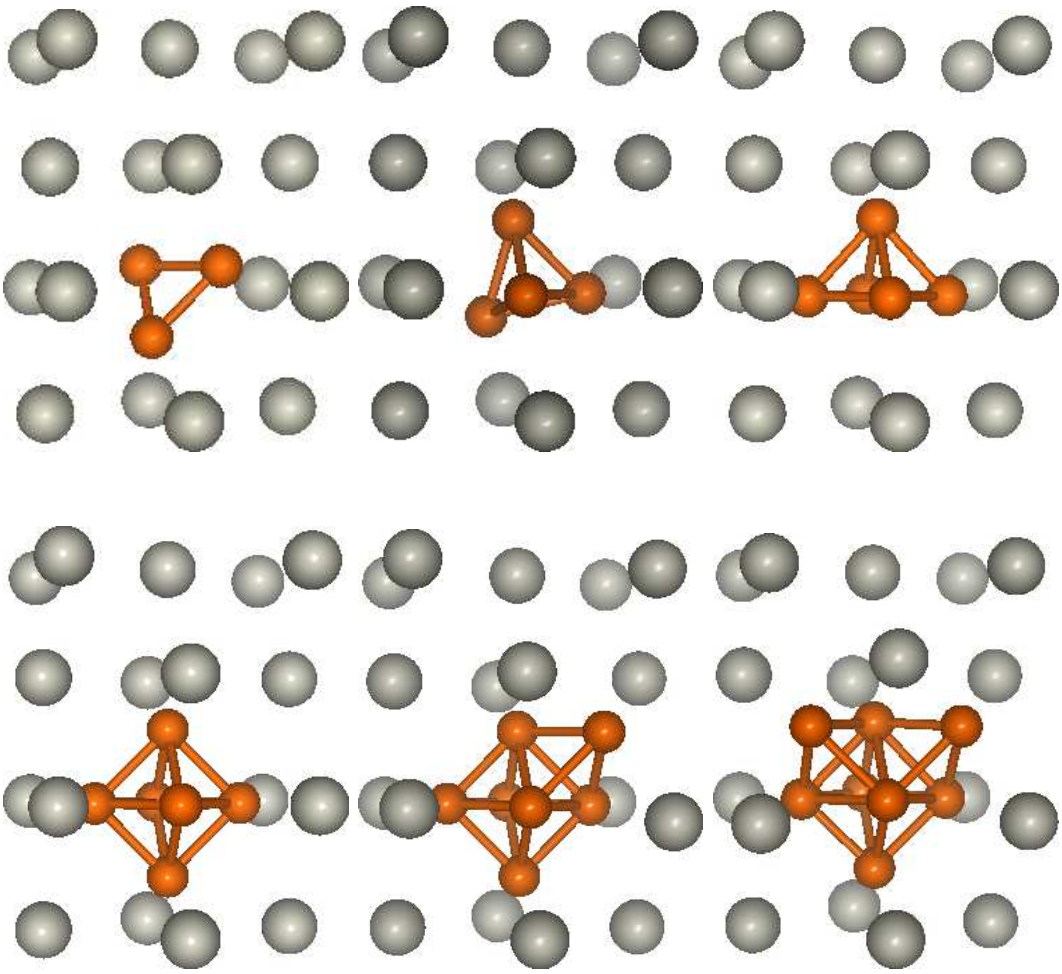

Figure 3.17: The minimum energy structures of He clusters at a Pd-vacancy. The large (gray) and small (orange) spheres denote Pd and He atoms, respectively.

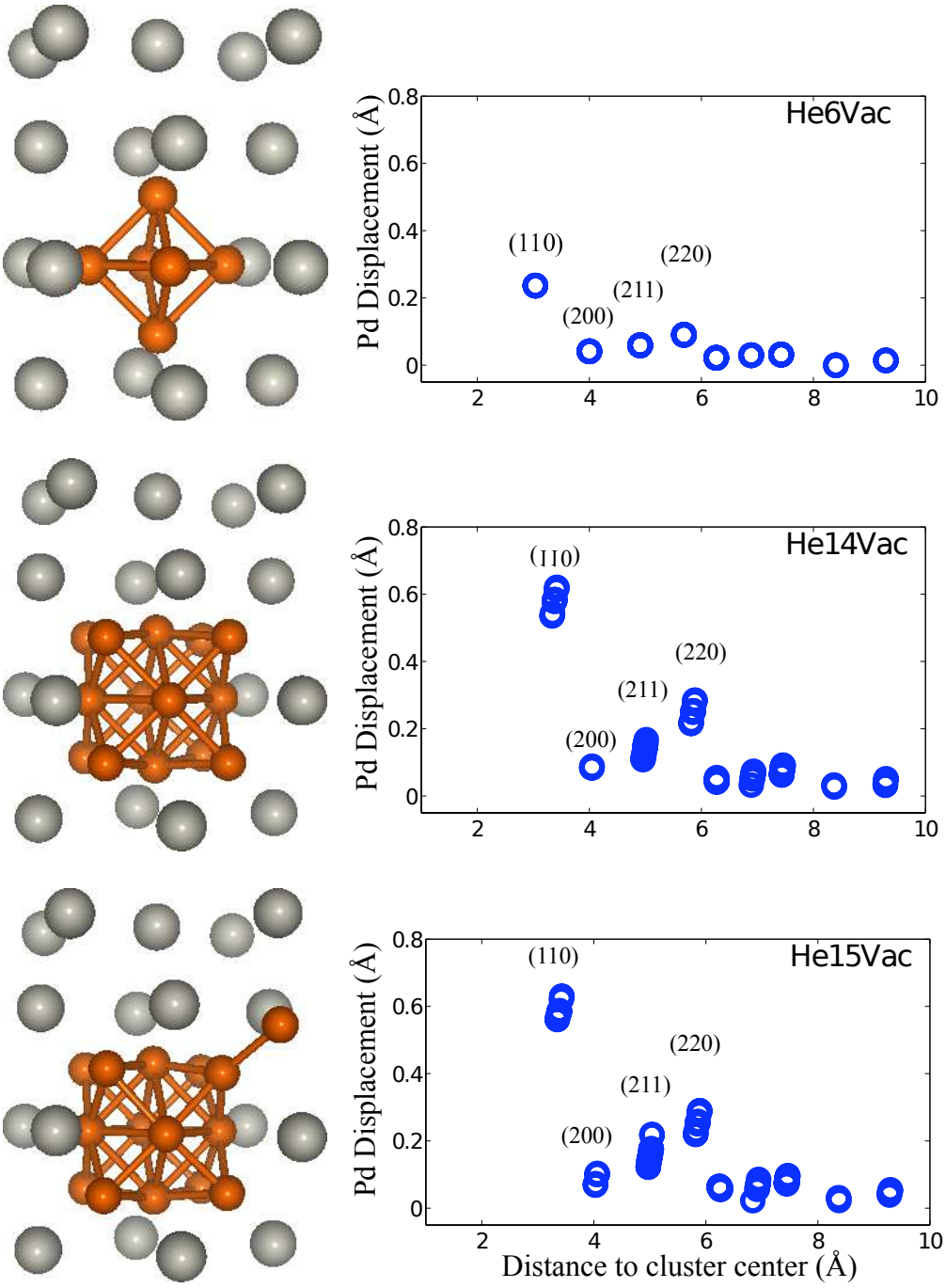

Figure 3.18: Structures of He clusters of 6, 14, and 15 atoms at a vacancy site in a $Pd_{107}He_n$ supercell. The large (gray) and small (orange) spheres denote Pd and He atoms, respectively. The right panel shows the corresponding Pd displacements. The circles represent the Pd displacements as a function of the distance to the Pd-vacancy site. The coordinates (n_1,n_2,n_3) of the neighboring atoms are in units of $a_0/2$.

the vacancy.

With the creation of a self-interstitial palladium atom, the binding of the self-interstitial Pd atom to the He clusters is examined by comparing the corresponding energy of the configuration with a well-separated self-interstitial Pd and a He cluster:

$$E^b_{SI} = (E(\mathrm{Pd_{31}He}_n + \mathrm{Pd}^{SI}) - E(\mathrm{Pd_{31}He}_n) - [\ E(\mathrm{Pd_{32}} + \mathrm{Pd}^{SI}) - 32\ E(\mathrm{Pd})\ ]. \qquad (3.9)$$

The results for n=5, 6, and 7 are listed in Table 3.5. The positive value at $n > 5$ implies that after a palladium atom is pushed away from its lattice site, it is not energetically favorable to stay near the helium cluster. The calculational results indicate that as the cluster is formed by interstitial helium atoms, spontaneous creation of a Pd lattice vacancy will take place at a very early state ($n \approx 5$).

Table 3.6 lists the energetics and the structural properties of helium clusters at the Pd-vacancy site. The binding energy of the clusters at the vacancy site is calculated using the following formulation:

$$E^b(\mathrm{Pd_{31}He}_n) = E(\mathrm{Pd_{31}He}_n) - E(\mathrm{Pd_{31}}) - n\ E_i(\mathrm{He}). \qquad (3.10)$$

The value d_{He-He} is the average distance (with a small variance) from each He atom to their nearest-neighbor He atoms, while u_{Pd} denotes the largest displacement among the surrounding Pd atoms in the supercell. During the growth of the cluster, d_{He-He} remains constant in the vicinity of 1.73$\mathring{A}$. Fig. 3.17 illustrates the geometry of selected clusters of size n= 3 - 8. The geometries for the 6-, 14- and 15-atom clusters at a vacancy site in the $\mathrm{Pd_{107}}$ supercell are illustrated in Fig. 3.18. The palladium displacement as a function of the distance to the He cluster is also plotted to the right of each cluster structure. In the displacement plot, the coordinates (n_1,n_2,n_3) in units of $a_0/2$ indicate the neighboring

Table 3.5: The energy for a self-interstitial Pd atom near the n-helium cluster in the $\mathrm{Pd_{32}}$ supercell with respect to an isolated interstitial. E^b_{SI} is defined in Eq. 3.10.

n	5	6	7
E^b_{SI} (eV)	-0.02	0.84	0.99

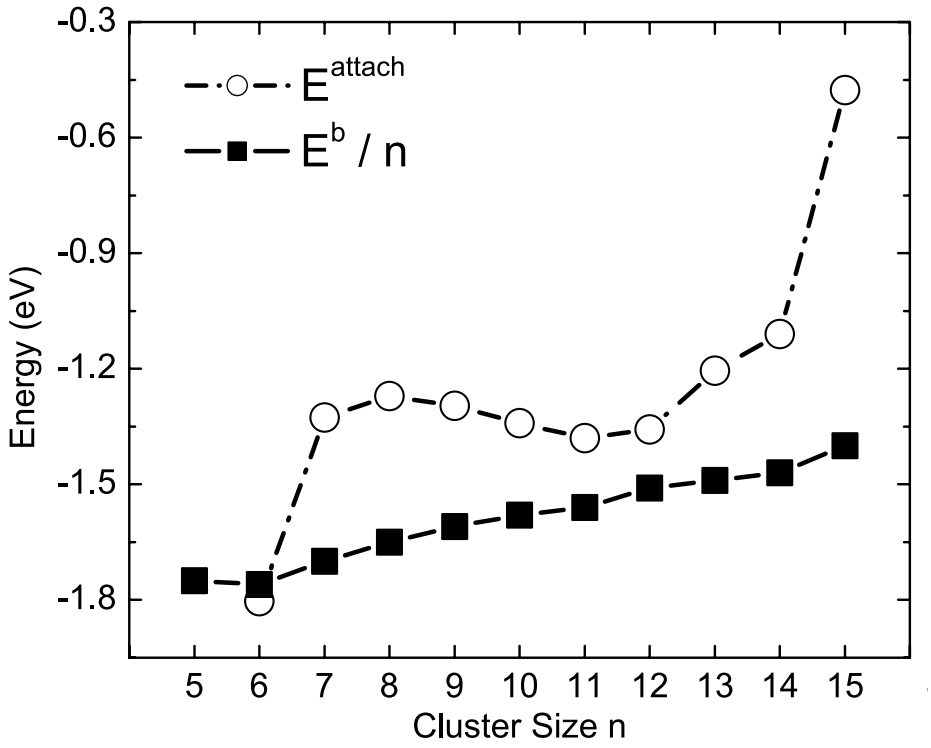

Figure 3.19: Calculated atomic attachment energy (open circle) and the binding energy per atom (solid square) as a function of He cluster size in the Pd_{107} supercell containing a Pd vacancy.

atoms around the vacancy site in the fcc lattice. As a result, we find that one Pd-vacancy can accommodate clusters up to fifteen He atoms without the need to induce an additional Pd vacancy. The atomic attachment energy, and the binding energy per atom as a function of cluster size are plotted in Fig. 3.19. A highly negative atomic attachment energy indicates a strong tendency toward absorbing an additional He atom to the cluster.

Table 3.6: Binding energy of n-atom helium clusters at a Pd-vacancy site in the Pd_{31} and Pd_{107} supercell. The derived binding energy per atom and the atomic attachment energy are listed in columns 3 and 4. Also listed in columns 5 and 6 are the average distance of nearest-neighbor helium d_{He-He} and the largest displacement u_{Pd} for the surrounding Pd atoms, respectively.

n	E^b (eV)	E^b / n (eV)	E^{Attach} (eV)	d_{He-He} ($\AA$)	u_{Pd} ($\AA$)
In Pd_{31} supercell					
2	-4.04	-2.02	-1.54	1.56	0.06
3	-5.60	-1.87	-1.56	1.64	0.12
4	-7.04	-1.76	-1.44	1.71	0.13
5	-8.74	-1.75	-1.70	1.72	0.18
6	-10.48	-1.75	-1.74	1.76	0.19
7	-11.49	-1.64	-1.01	1.75	0.39
8	-12.50	-1.56	-1.00	1.75	0.57
In Pd_{107} supercell					
5	-8.76	-1.75		1.76	0.22
6	-10.56	-1.76	-1.80	1.78	0.24
7	-11.89	-1.70	-1.33	1.78	0.43
8	-13.16	-1.65	-1.27	1.78	0.61
9	-14.46	-1.61	-1.30	1.77	0.62
10	-15.80	-1.58	-1.34	1.76	0.61
11	-16.06	-1.56	-1.38	1.75	0.61
12	-18.22	-1.51	-1.36	1.74	0.62
13	-19.42	-1.49	-1.21	1.74	0.61
14	-20.53	-1.47	-1.11	1.73	0.62
15	-21.01	-1.40	-0.48	1.70	0.63

CHAPTER IV

HELIUM CLUSTER INSIDE PALLADIUM HYDRIDES

Palladium readily forms reversible hydrides at equilibrium pressures under ambient condition[42, 86]. Palladium is often used as a material for the storage and processing of the radioactive element tritium because of its resistance to oxidation and poisoning, its fast kinetics of absorption and desorption, and its ability to retain ^{3}He created by the decay of tritium in the metal [85, 84]. As a result, palladium tritide is commonly found in the nuclear industry as a storage medium. However, the short half-life (12.3 years) of tritium can naturally produce He in the metal lattice, and these He atoms can accumulate and form He nano clusters, which alter the tritide properties during aging. This can be detrimental to the physical integrity and storage functionality of the Pd tritide. Understanding the mechanism of the aging process is of practical interest in relation to the use of metals as tritium storage materials.

Atomistic understanding of helium clusters in metals is an interesting topic in theoretical modeling. First-principles calculations have the capacity to provide accurate formation energies of helium impurities [53] and their diffusion barriers in metal tritides [39]. One of the values of these kinds of calculations is that one can examine in detail the atomic defect configuration, as well as its transition pathway.

In this chapter we present a study of helium behavior considering the co-existence of hydrogen with various concentrations in the fcc palladium lattice. We systematically investigate helium diffusion, and cluster formation in various palladium hydrides with and without considering a vacancy defect. Our calculations show that the helium atom exhibits different energetics and migration mobility when the metal lattice is loaded with hydrogen. The atomistic mechanisms of the He interaction with hydrogen and palladium are investigated by studying the electronic properties. In addition, the formation of small He clusters in the interstitial region with a creation of the Frenkel defect is investigated in the presence

of hydrogen.

4.1 Computational Methods

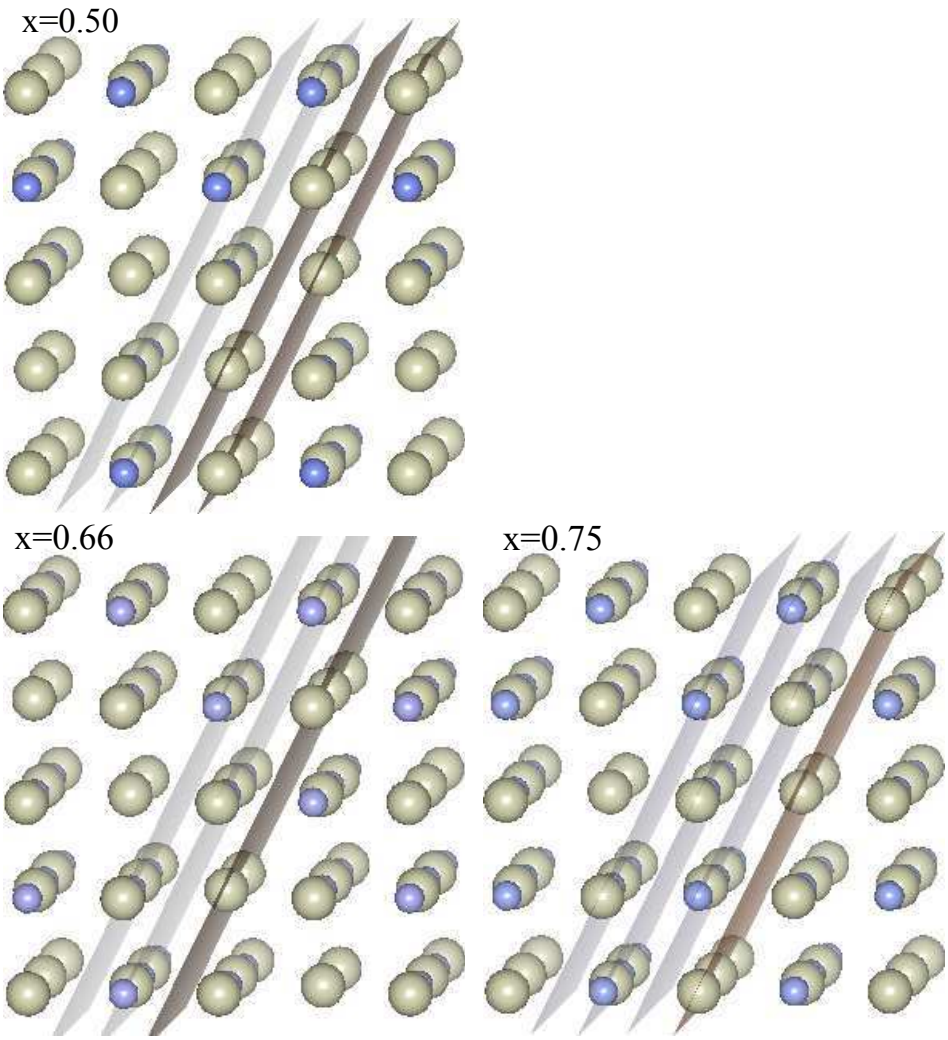

Figure 4.1: The palladium hydride (PdH_x) structures used in the calculations. The (420) lattice planes are highlighted for H concentrations at x=0.50, 0.66, and 0.75. All the octahedral sites on the gray planes are occupied by H, while all octahedral sites on the red planes are empty.

Previous studies on the energetics and H ordering in various Pd hydride systems have determined the low energy configurations of PdH_x at different hydrogen concentrations x [50]. To model helium in the palladium hydrides, we choose a supercell of palladium in which all H atoms occupy octahedral sites in a specified order, as shown in Fig. 4.1. In the hydrides consisting of higher H concentrations, hydrogen atoms have a long-range order in the (420)

Table 4.1: Lattice parameters and symmetry of Pd hydrides at various concentrations. E^b(H) is the calculated binding energy per hydrogen atom as defined in Eq. 4.1.

hydrides	structure	lattice symmetry	(420) sequence	E^b(H)	a_0
$PdH_{0.25}$	$L1_2$	simple cubic	none	-0.17 eV	4.01 Å
$PdH_{0.50}$	NiMo	body-centered tetragonal	AABB	-0.22 eV	4.05 Å
$PdH_{0.66}$	Ni_2Mo	body-centered orthorhombic	AAB	-0.23 eV	4.09 Å
$PdH_{0.75}$	$D0_{22}$	body-centered tetragonal	AAAB	-0.22 eV	4.10 Å

planes [83], which repeats sequently as AABB, AAB, and AAAB for x=0.50, 0.66, and 0.75, respectively. All the octahedral sites on plane A (blue) are occupied by H atoms, while all the octahedral sites are empty on plane B (gray). We perform first-principles calculations with Density-Functional Theory using the Vienna *ab initio* Simulation Pacakge VASP [69, 60]. The plane-wave basis set with Blöchl's projector augmented-wave (PAW) method is applied for the electron-ion interactions with the generalized-gradient approximation (GGA) also implemented in VASP [68]. The supercells for different hydrogen concentrations are fully relaxed to the equilibrium lattice constant. The lattice expansions with respect to pure Pd are shown in Fig. 4.2. In comparison with the experimental measurements[81] and previous DFT calculations[50], our calculations provide reliable results. Table 4.1 summarizes the structural parameters and the symmetries of the hydrides used in our study.

For each Pd hydride, the binding energy of interstitial hydrogen is calculated using the same definition as in the previous DFT work for Pd hydrides[82]:

$$E^b(\mathrm{H}) = \frac{1}{m}[E(\mathrm{Pd}_l\mathrm{H}_m) - lE(\mathrm{Pd}) - \frac{m}{2}E(\mathrm{H}_2)], \tag{4.1}$$

where integers l and m specify the size of the supercell and the H concentration, respectively. For comparison, the binding energy of an interstitial He atom is evaluated with respect to the pure Pd-H system and an isolated helium atom:

$$E^b(\mathrm{He}, \mathrm{Pd}_l\mathrm{H}_m) = E(\mathrm{Pd}_l\mathrm{H}_m\mathrm{He}) - E(\mathrm{Pd}_l\mathrm{H}_m) - E(\mathrm{He}). \tag{4.2}$$

We start with one helium atom in the interstitial site per supercell. The site preference is determined by calculating the binding energy of the helium atom at different interstitial

sites in the hydrides. The diffusion path and the diffusion barrier of the interstitial helium atom are evaluated using the Nudged Elastic Band (NEB) method[66]. The mobility of a helium atom is an important factor which affects cluster formation. He clusters of various size are investigated for four hydride systems. The energetics and structures of the clusters are investigated systematically as the H concentration varies. In addition, the electronic properties are examined to understand the interaction of the He atom with the Pd-H host [15].

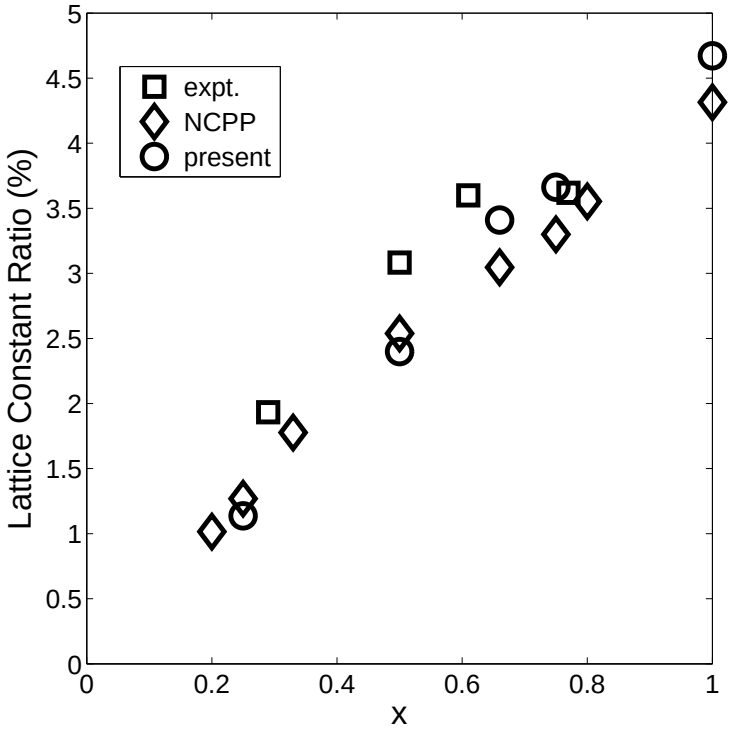

Figure 4.2: The lattice expansion of Pd hydrides with respect to pure Pd at various hydrogen concentration x (=H/Pd). The experimental results (expt.), the norm-conserving pseudopotential calculation results (ncpp), and the present results are plotted for comparison.

4.2 He Clusters in $PdH_{0.25}$

4.2.1 Interstitial Helium

$PdH_{0.25}$ is modeled with a supercell of $Pd_{32}H_8$. H atoms are located at the octahedral sites of the Pd fcc lattice. The arrangement of H corresponds to the $L1_2$ structure with

O_h^1 symmetry. The binding energy of helium at different interstitial positions in $Pd_{32}H_8$ is calculated using Eq. 4.2 with l=32 and m=8. The results for helium at the octahedral and the tetrahedral sites are summarized in Table 4.2. It is found that a helium atom prefers the octahedral site over the tetrahedral site in the $PdH_{0.25}$ matrix.

4.2.2 Helium Diffusion

In $PdH_{0.25}$, each empty octahedral site has 12 nearest-neighbor octahedral sites, eight of which are not occupied by hydrogen atoms. The minimum energy path of helium migration, starting from an octahedral site, is via a tetrahedral site to the nearest unoccupied octahedral site. This is similar to that of helium diffusion in the pure Pd lattice (x=0). The inset of Fig. 4.3(a) illustrates the diffusion path in which the dashed line connects neighboring octahedral sites (solid circles) on one of the (100) planes. The open circles denote nearby tetrahedral sites which are out of the plane. The transition state of the diffusion goes through a position slightly shifted away from the tetrahedral site, as a consequence of the repulsive forces from surrounding hydrogen atoms. The diffusion barrier obtained using the NEB method is shown in Fig. 4.3(b), with the energy zero chosen at the octahedral site. The diffusion coordinate on the x-axis goes from an octahedral site, via the nearby tetrahedral site, to the nearest octahedral site. The diffusion barrier for helium (solid line) is 0.20 eV as shown in the figure, which is higher in $PdH_{0.25}$ than in the Pd metal. For comparison, the diffusion behavior of an interstitial hydrogen is evaluated by adding an additional H atom to the $Pd_{32}H_8$ supercell. It is found that hydrogen moves in the similar path as that of helium, but the diffusion barrier is much smaller at 0.09 eV, as shown by the dashed line in Fig. 4.3(b).

Table 4.2: Energies of a helium atom at the octahedral (O_h) and the tetrahedral (T_d) sites in the $Pd_{32}H_8$ supercell as defined in Eq. 4.2. The number of the nearest-neighbor (NN) H atoms and the He to H distance (d_{He-H}) are also listed.

	E^b(He)	NN H atoms	d_{He-H}
O_h	3.22 eV	4	2.83 Å
T_d	3.36 eV	1	2.35 Å

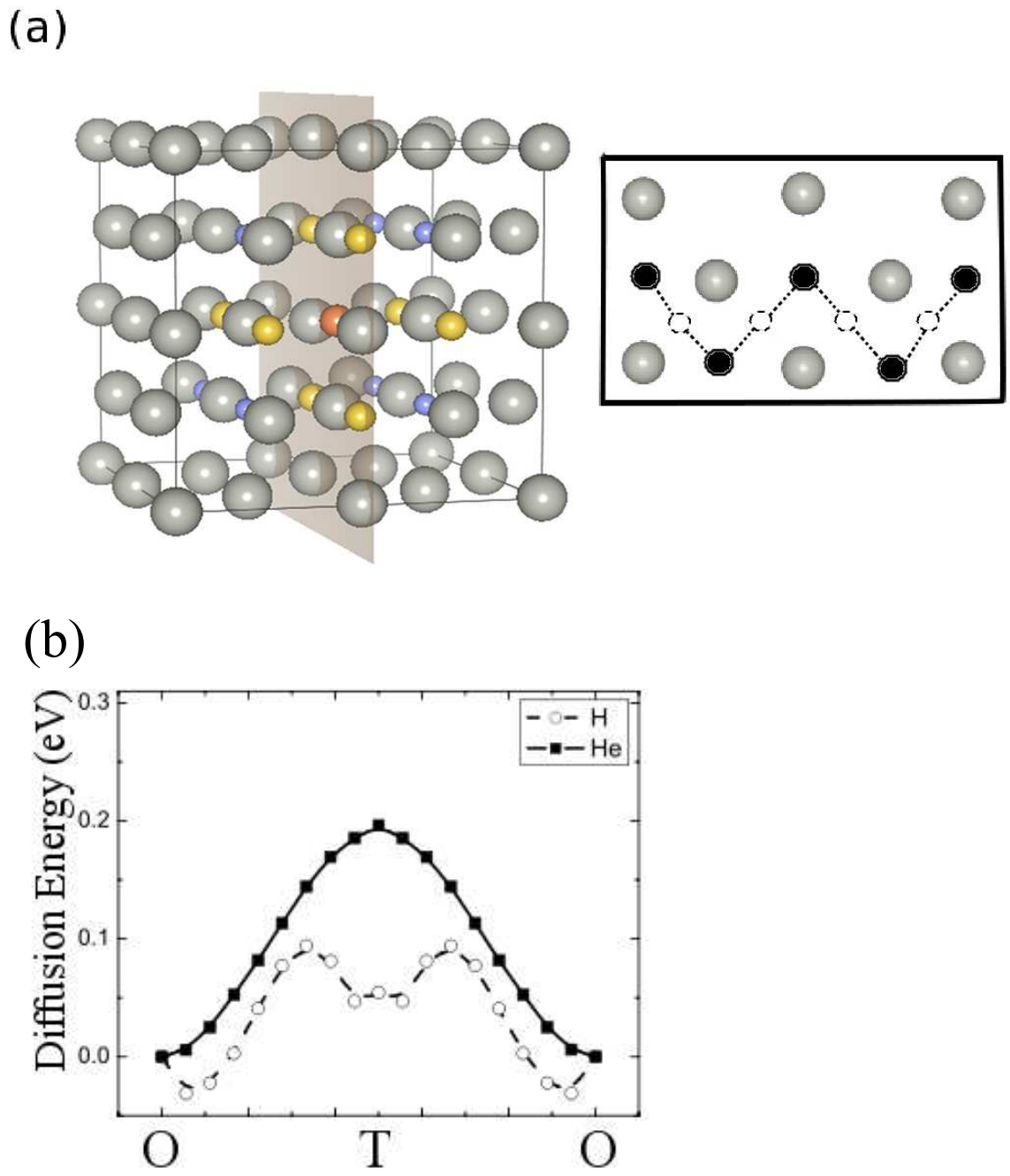

Figure 4.3: (a) An illustration of the He diffusion path in the $Pd_{32}H_8$ supercell. Grey (big) and blue (small) spheres represent Pd and H atoms in the hydride. Orange and yellow spheres represent the He atom and the nearest-neighbor empty octahedral sites. A helium atom diffuses from an octahedral site to another via a tetrahedral site in the $\langle 111 \rangle$ direction. The inset on the right illustrates the diffusion path in which the dashed line connects the neighboring octahedral sites (solid circles) on the (100) plane. The open circles denote nearby tetrahedral sites which are out of the plane. (b) Potential energies of He (solid square) and H (open circle) with respect to the energy at the octahedral site using the NEB method.

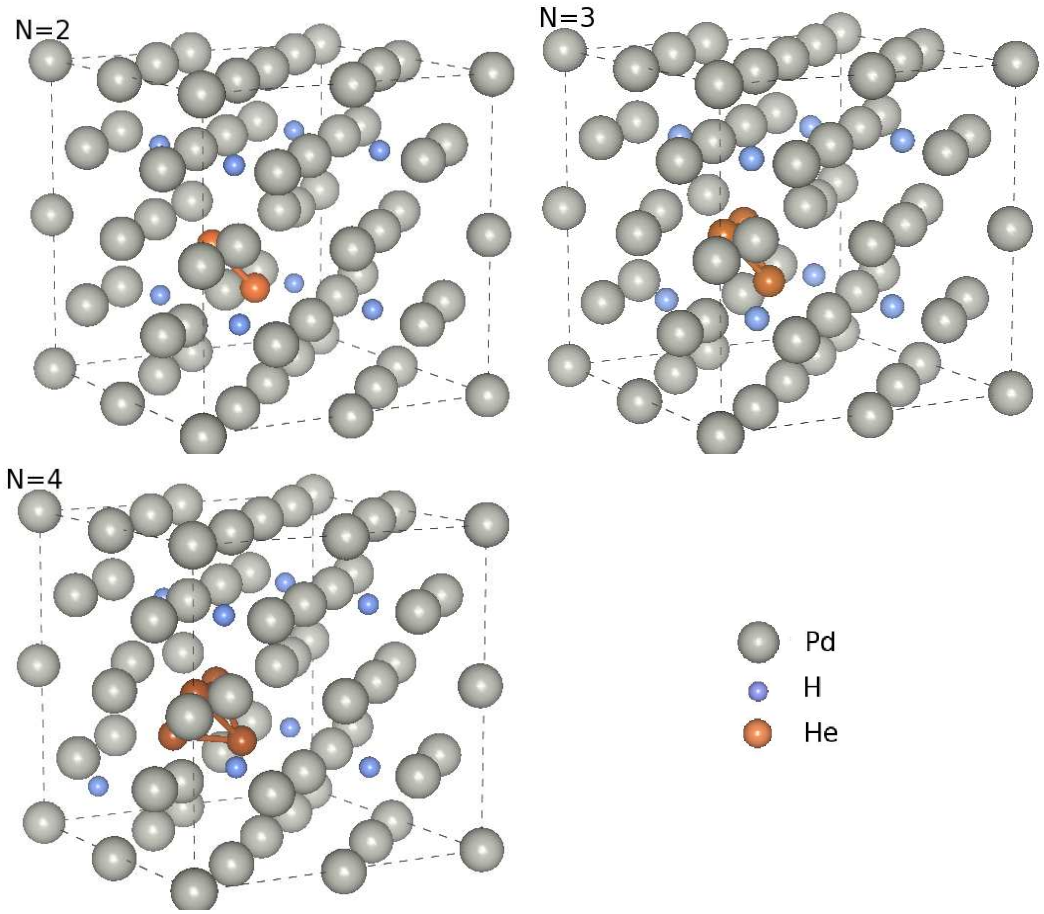

Figure 4.4: Structures of He clusters with two, three, and four He atoms. The atoms aggregate at the neighboring interstitial sites in the $Pd_{32}H_8$ superlcell. The gray (big), blue (small), and orange spheres denote the Pd, H and He atoms, respectively.

4.2.3 Helium Cluster Formation

The energetics of helium clusters is studied by introducing helium atoms one by one to the interstitial region in the $Pd_{32}H_8$ supercell. Each additional helium atom is placed at one nearest octahedral site around the existing clusters. Multiple structures for a cluster of the same size are explored to determine the lowest-energy configuration. The binding energy of the n-atom cluster is calculated with respect to the energy of $Pd_{32}H_8$ and n isolated interstitial He atoms:

$$E^b(\mathrm{He}_n, \mathrm{Pd}_{32}\mathrm{H}_8) = E(\mathrm{Pd}_{32}\mathrm{H}_8\mathrm{He}_n) - E(\mathrm{Pd}_{32}\mathrm{H}_8) - nE^i(\mathrm{He}, \mathrm{Pd}_{32}\mathrm{H}_8), \tag{4.3}$$

Table 4.3: Binding and attachment energies (eV) of He clusters in the interstitial region of the $Pd_{32}H_8$ supercell. The values in the parentheses correspond to the structure in which a Frenkel-like defect is generated together with a self-interstitial Pd atom.

n	E^b	E^b / n	E^{Attach}
2	-0.46	-0.23	-0.46
3	-1.21	-0.40	-0.75
4	-1.95	-0.49	-0.74
5	-2.30 (-2.89)	-0.46 (-0.58)	-0.35 (-0.95)
6	-2.69 (-3.57)	-0.45 (-0.59)	-0.30 (-0.67)

where

$$E^i(\mathrm{He}, \mathrm{Pd_{32}H_8}) = E(\mathrm{Pd_{32}H_8He}) - E(\mathrm{Pd_{32}H_8}). \tag{4.4}$$

The atomic attachment energy is defined as the energy difference between the n- and $(n-1)$-sized helium cluster:

$$E^{Attach}(\mathrm{Pd_{32}H_8He}_n) = E^b(\mathrm{He}_n, \mathrm{Pd_{32}H_8}) - E^b(\mathrm{He}_{n-1}, \mathrm{Pd_{32}H_8}). \tag{4.5}$$

E^{Attach} is a measure of the energy change for adding an interstitial helium atom to an existing $(n-1)$-sized cluster. Figure 4.4 shows the minimum-energy structures of a few small helium clusters (n=2-4) formed in the interstitial region of a $Pd_{32}H_8$ supercell. A pair of helium atoms form a dimer and line up in the $\langle 110 \rangle$ direction at one of the nearest octahedral sites. The separation of two He atoms equals 1.73Å. The angle between the dimer and the third atom is 60.1 °, indicating that the three helium atoms form a nearly perfect triangle. The torsion angle of the four-helium cluster is 69.8 °, giving rise to a tetrahedral structure. No specific orientation is found for these clusters in the minimum-energy configurations. Helium atoms favor the most compact structure in the interstitial region of the $Pd_{32}H_8$ lattice.

The calculated results for larger clusters (n=5, 6) are illustrated in the top row in Fig. 4.5. These structures, however, are metastable because their energy can be further lowered by pushing a nearby Pd atom away from its lattice site. The displacement of Pd produces a pair of Frenkel-like defects and a self-interstitial atom (SIA). The structures for such a condition are shown in the second row in Fig. 4.5, where a self-interstitial Pd

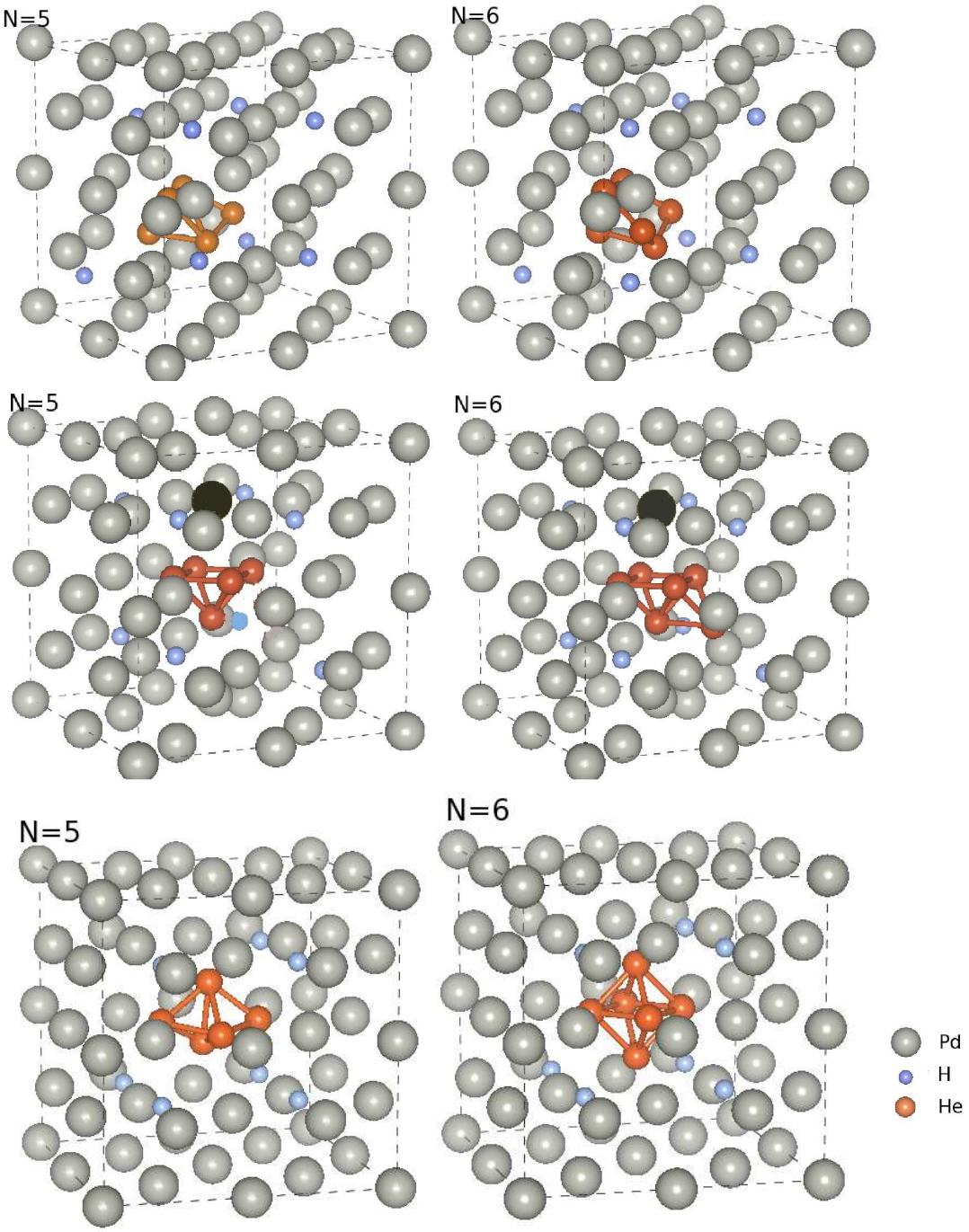

Figure 4.5: Top: The structures of interstitial He clusters of 5 and 6 atoms in the $Pe_{32}H_8$ supercell. Middle: These He atoms accumulate around a vacancy generated by the creation of an interstitial Pd atom (dark sphere) in the supercell. Bottom: The structures of He clusters around a Pd-vacancy in the $Pd_{31}H_8$ supercell.

(dark colored) is moved to an octahedral site next to the vacancy. The cluster reconfigures to a chandelier-like structure, in which four atoms are on the same (100) plane containing the vacancy and one atom is in the middle under the plane. The additional atom is attached to the vacancy site along the $\langle 110 \rangle$ direction. Table 4.3 summarizes the the binding energies and the atomic attachment energies for clusters of the size up to six helium atoms at the interstitial sites. The values in parentheses for $n \geq 5$ are for the structures in which a Frenkel-like defect is generated with a self-interstitial Pd atom. Energies of these configurations are significantly lower compared to that of the defect-free results.

To understand the stability of the Pd atom near the cluster site, the self-interstitial energy is evaluated with respect to the energy of a He cluster located at the Pd-vacancy, $E(\mathrm{Pd_{31}H_8He}_n)$) and the energy of a Pd atom as an isolated interstice:

$$E^b_{SI} = E(\mathrm{Pd_{32}H_8He}_n) - E(\mathrm{Pd_{31}H_8He}_n) - [(E(\mathrm{Pd_{32}H_8} + \mathrm{Pd}^{SI}) - (E(\mathrm{Pd_{32}H_8})]. \quad (4.6)$$

$E(\mathrm{Pd_{32}H_8He}_n)$ is the lowest energy for the n-atom cluster in a $\mathrm{Pd_{32}H_8}$ host. The sign of E_{SI} is an indication if the Pd atom surrounding the He cluster will get away or not. These calculated results are listed in Table 4.4. The positive values of E_{SI} for $n \geq 5$ imply that the Pd atom prefers to be away from the cluster energetically, and the opposite is true for $n \leq 4$. As a result, when the interstitial helium clusters grow big enough, they can create a Pd-vacancy to form a much more stable cluster at the vacancy site. The structures of five- and six-atoms are illustrated in the bottom row in Fig. 4.5.

In the following, we will study the energetics for cluster formation in a system with a Pd-vacancy using a supercell of $\mathrm{Pd_{31}H_8}$. The binding energies of these clusters are calculated

Table 4.4: Energy of a self-interstitial Pd atom induced by an n-atom helium cluster calculated with a $\mathrm{Pd_{32}H_8}$ supercell. E_{SI} is defined in Eq. 4.7 and is in reference to the energy of an isolated self-interstitial Pd.

n	5	6
E_{SI} (eV)	0.19	1.03

Table 4.5: Binding and attachment energies (eV) of He clusters at a Pd-vacancy site calculated with a $Pd_{31}H_8$ supercell.

n	E^b	E^b / n	E^{Attach}
1	-2.35	-2.35	-2.35
2	-3.75	-1.88	-1.40
3	-5.17	-1.72	-1.41
4	-6.69	-1.67	-1.53
5	-7.96	-1.59	-1.26
6	-9.47	-1.58	-1.51

by

$$E^b(\mathrm{He}_n, \mathrm{Pd}_{31}\mathrm{H}_8) = E(\mathrm{Pd}_{31}\mathrm{H}_8\mathrm{He}_n) - E(\mathrm{Pd}_{31}\mathrm{H}_8) - E^i(\mathrm{He}, \mathrm{Pd}_{32}\mathrm{H}_8). \tag{4.7}$$

Table 4.5 summarizes the the binding energies and the atomic attachment energies for clusters of up to six helium atoms at the vacancy site. The attachment energy of each cluster is plotted in Fig. 4.6.

In conclusion, multiple interstitial helium atoms attract each other to form He_n clusters in $PdH_{0.25}$. When $n \geq 5$, the interstitial clusters create a Pd-vacancy by removing a nearby Pd atom to an interstitial site which further lowers the energy. This interstitial Pd atom is likely to diffuse away from the cluster. As a result, the cluster occupies the vacancy site and reconfigures to a lower energy structure. The clusters form in a manner similar to those found in the presence of an intrinsic Pd vacancy.

4.3 He Clusters in $PdH_{0.50}$

4.3.1 Interstitial Helium

$PdH_{0.50}$ is modeled by a supercell with a composition of $Pd_{32}H_{16}$. Hydrogen atoms are located sequentially on the (420) planes in real space with two hydrogen planes (octahedral sites fully occupied by hydrogen) followed by two empty planes. The structure is shown in Fig. 4.7(a) with the (420) lattice plane indicated. The ordering of hydrogen follows the NiMo type lattice with O_{4h}^{19} (or $I4_1/\mathrm{amd}$) symmetry. The calculated equilibrium lattice constant for this concentration is listed in Table 4.1. The He binding energies at different interstitial positions are calculated using Eq. 4.2 with l=32, m=16. The results for helium

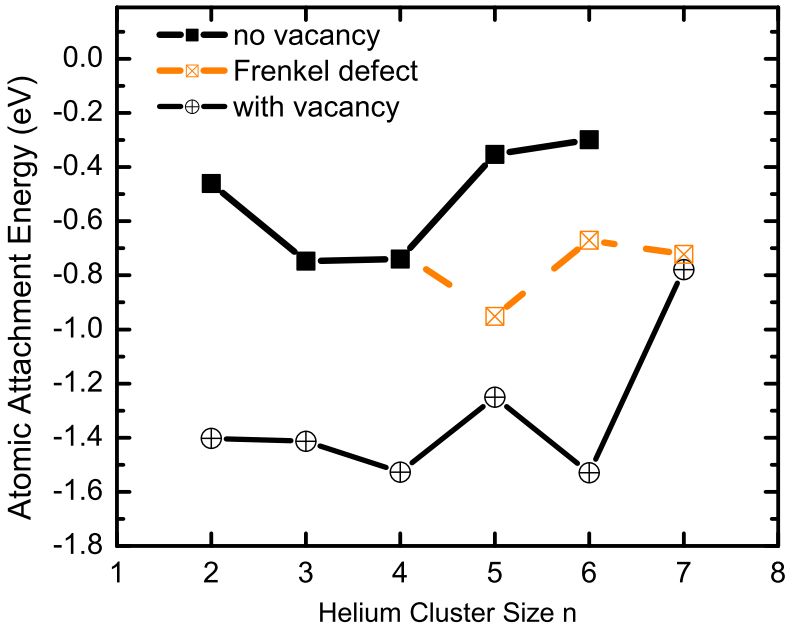

Figure 4.6: Atomic attachment energies for He clusters inside the $Pd_{32}H_8$ (square) and $Pd_{31}H_8$ (circle) supercell. The solid line denotes the case without a Pd-vacancy inside the host matrix, the dash-doted line denotes the case in which one Pd atom is moved to an interstitial site in the supercell.

at the octahedral and tetrahedral sites are summarized in Table 4.6, which shows that a helium atom prefers to occupy the octahedral over the tetrahedral site in $Pd_{32}H_{16}$.

4.3.2 Helium Diffusion

In $PdH_{0.50}$, each empty octahedral site has twelve octahedral sites as the nearest-neighbor, eight of which are occupied by hydrogen atoms. Namely, an empty site is a tetrahedral

Table 4.6: Energies for a helium atom at the octahedral (O_h) and the tetrahedral (T_d) sites in the $Pd_{32}H_{16}$ supercell as defined in Eq. 4.2. The number of the nearest-neighboring (NN) H atoms and the corresponding He to H distance (d_{He-H}) are also listed.

	E^b(He)	NN H atoms	d_{He-H}
O_h	2.99 eV	8	2.86 Å
T_d	3.27 eV	2	2.51 Å

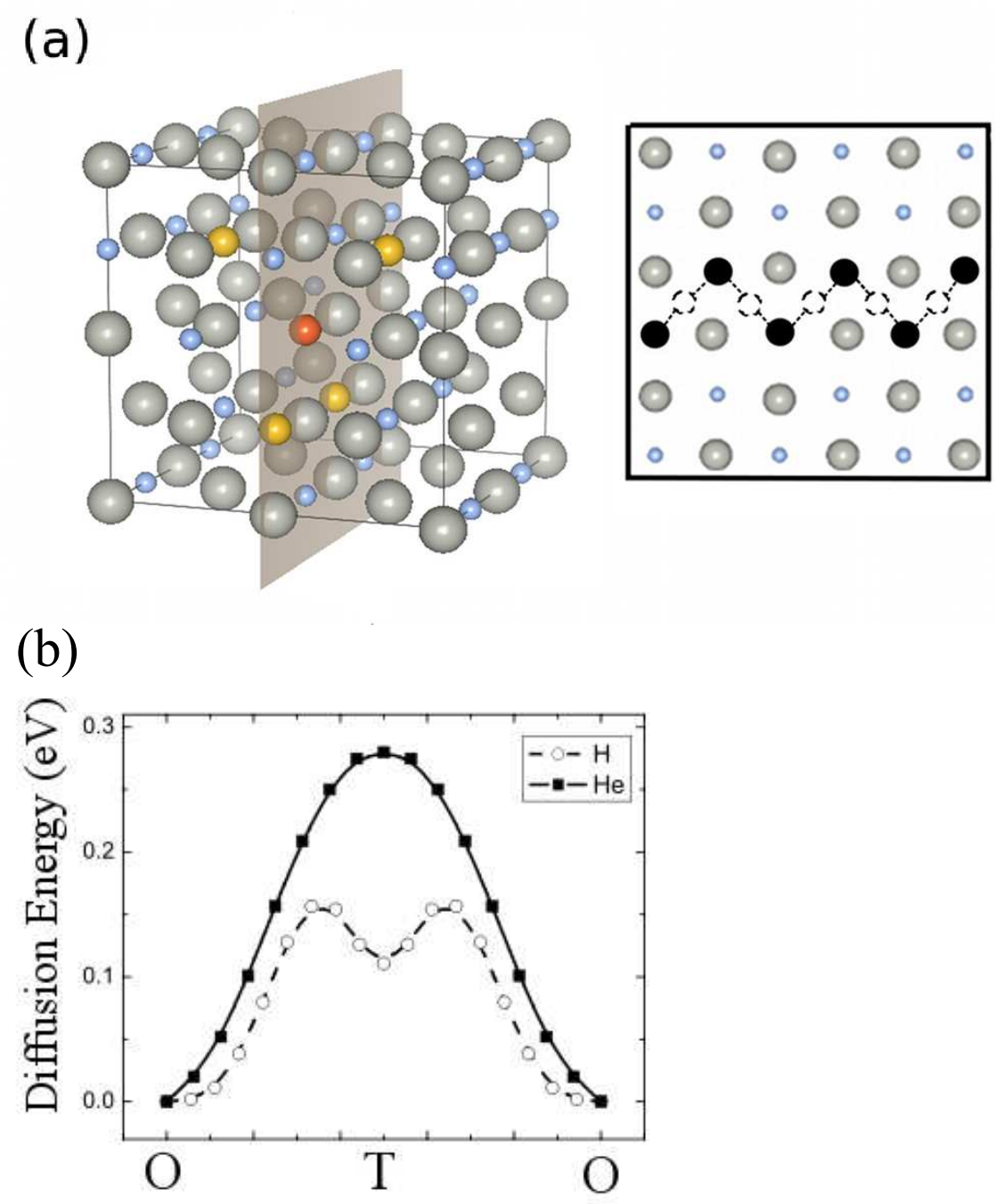

Figure 4.7: (a) An illustration of the He diffusion path in the $Pd_{32}H_{16}$ supercell. Gray (big) and blue (small) spheres represent Pd and H atoms in the hydride. Orange and yellow particles represent the He atom and the nearest-neighbor empty octahedral sites. A helium atom diffuses from an octahedral site to another via a tetrahedral site in the $\langle 111 \rangle$ direction. The inset on the right illustrates the diffusion path in which the dashed line connects the neighboring octahedral sites (solid circles) on the (100) plane. The open circles denote nearby tetrahedral sites which are out of the plane. (b) Potential energies of He (solid square) and H (open circle) with respect to the energy at the octahedral site using the NEB method.

Table 4.7: Binding and atomic attachment energies (eV) of He clusters in the interstitial region of the $Pd_{32}H_{16}$ supercell.

n	E^b	E^b / n	E^{Attach}
2	-0.22	-0.11	-0.22
3	-0.40	-0.06	-0.18
4	-0.49	-0.02	-0.09
5	-1.10	-0.12	-0.62
6	-1.71	-0.10	-0.60

center of the other four empty sites, as illustrated in Fig. 4.7(a). The minimum energy path of the migration is from one octahedral site, via a tetrahedral site, to one of the hydrogen-free octahedral sites. The inset of Fig. 4.7(a) demonstrates a possible diffusion path in which the dashed line connects neighboring octahedral sites (solid circles) on a (100) plane. The open circles denote nearby tetrahedral sites which are out of the plane. The transition state of the diffusion is slightly off the perfect tetrahedral sites due to the repulsive forces from surrounding hydrogen atoms. The diffusion barrier obtained using the NEB method is shown in Fig. 4.7(b) with energy zero set at the octahedral site. The diffusion coordinates on the x-axis goes from an octahedral site, via the nearby tetrahedral site, to the nearest octahedral site. As a result, the diffusion barrier for helium (solid line) is 0.28 eV as shown in the plot. For comparison, the diffusion of interstitial hydrogen is also studied using the same method. It was found that hydrogen follows a similar path as that of helium. However, the diffusion barrier is only 0.15 eV, as shown in the dashed line in Fig. 4.7(b).

4.3.3 Helium Cluster Formation

We further investigated the structure and energetics of helium clusters in the interstitial region in the $Pd_{32}H_{16}$ supercell. The binding energy of an n-atom cluster, as well as the atomic attachment energy for a helium cluster with n-1 atoms, is calculated in the same way as defined in Eq. 4.3 and 4.5 in Section 4.2.3:

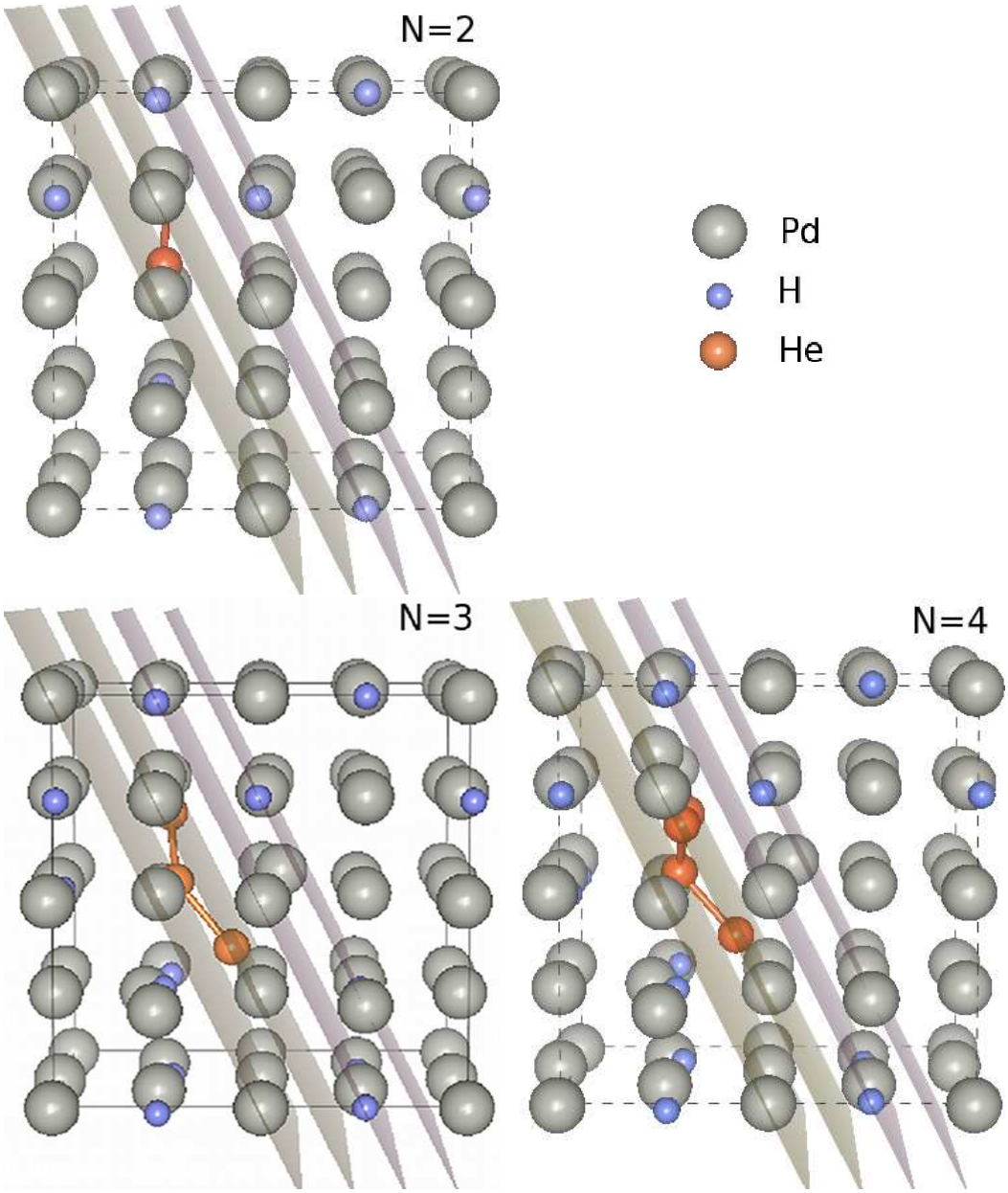

Figure 4.8: Structures of He clusters containing two, three, and four He atoms. The atoms accumulate at neighboring interstitial sites in the $Pd_{32}H_{16}$ superlcell. A set of (420) lattice planes are highlighted showing H-rich (blue) and H-free (gray) regions in the supercell.

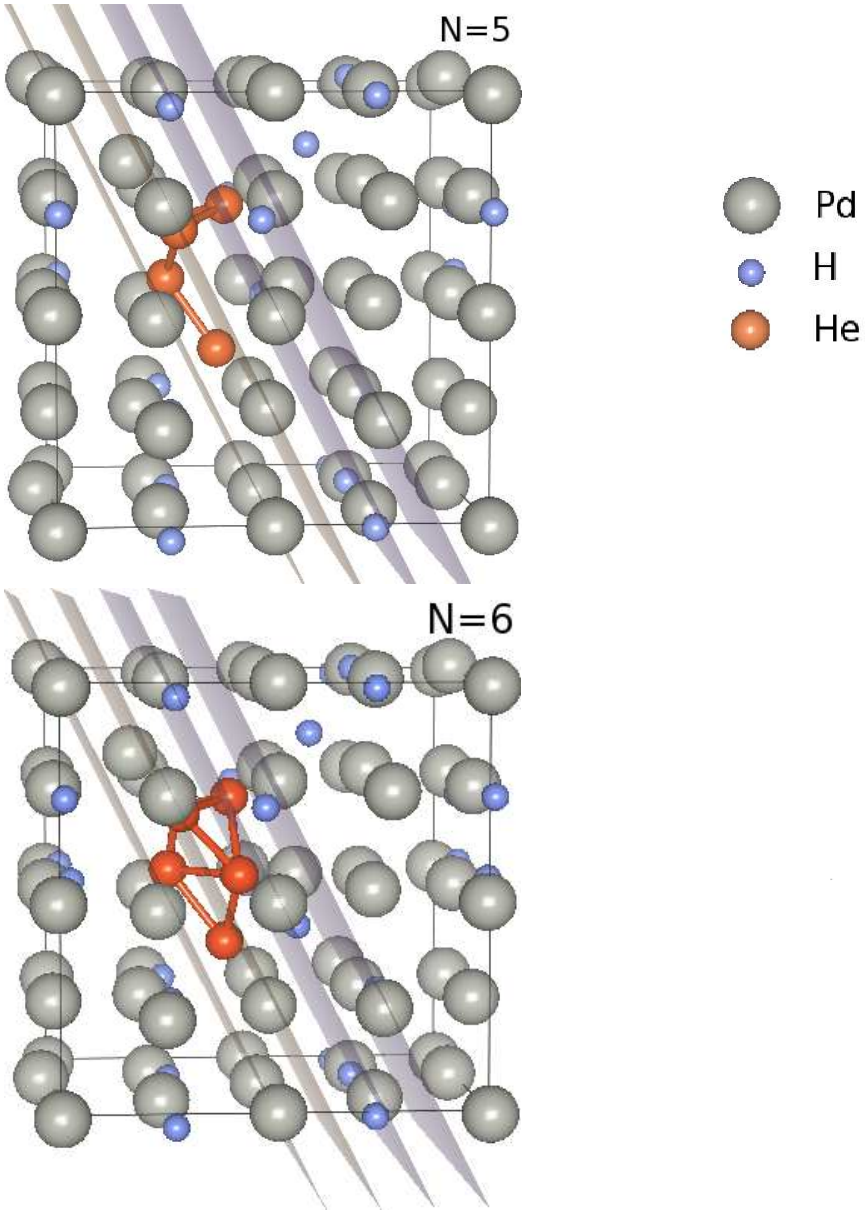

Figure 4.9: Structures of the He clusters containing five and six He atoms. The atoms accumulate at neighboring interstitial sites in the $Pd_{32}H_{16}$ superlcell. A set of (420) lattice planes are highlighted showing H-rich (blue) and H-free (gray) regions in the supercell.

$$E^b(\mathrm{He}_n, \mathrm{Pd}_{32}\mathrm{H}_{16}) = E(\mathrm{Pd}_{32}\mathrm{H}_{16}\mathrm{He}_n) - E(\mathrm{Pd}_{32}\mathrm{H}_{16}) - nE^i(\mathrm{He}, \mathrm{Pd}_{32}\mathrm{H}_{16}), \quad (4.8)$$

$$E^i(\mathrm{He}, \mathrm{Pd}_{32}\mathrm{H}_{16}) = E(\mathrm{Pd}_{32}\mathrm{H}_{16}\mathrm{He}) - E(\mathrm{Pd}_{32}\mathrm{H}_{16}). \quad (4.9)$$

$$E^{Attach}(\mathrm{Pd}_{32}\mathrm{H}_{16}\mathrm{He}_n) = E^b(\mathrm{He}_n, \mathrm{Pd}_{32}\mathrm{H}_{16}) - E^b(\mathrm{He}_{n-1}, \mathrm{Pd}_{32}\mathrm{H}_{16}). \quad (4.10)$$

Figure 4.8 shows the minimum-energy structures of small helium clusters (n=2-4) in the interstitial region of a $Pd_{32}H_{16}$ supercell. A pair of helium atoms form a dimer and line up in the $\langle 110 \rangle$ direction at the nearest octahedral sites. The separation of two He atoms equals 1.78 Å. Unlike the trimer in $PdH_{0.25}$ which forms an equilateral triangle, the third helium atom favors a chain structure in $PdH_{0.5}$. The angle between the third atom and the dimer is 133.2°. For n=4, a flat structure on the (420) plane is favorable over the tetrahedron structure found in $Pd_{32}H_8$. The structure is not completely planar. The torsion angle of the cluster is 124.7°. In conclusion, small helium clusters tend to align with the ordering of H on the (420) plane in $PdH_{0.5}$. The results for the binding energies and the atomic attachment energies of the clusters are listed in Table 4.7.

The calculated structures for clusters containing five and six helium atoms are illustrated in Fig. 4.9. To understand the stability of the Pd atom near the cluster site, the self-interstitial energy is evaluated in analogy to Eq. 4.6:

$$E^b_{SI} = E(\mathrm{Pd}_{32}\mathrm{H}_{16}\mathrm{He}_n) - E(\mathrm{Pd}_{31}\mathrm{H}_{16}\mathrm{He}_n) - [(E(\mathrm{Pd}_{32}\mathrm{H}_{16} + \mathrm{Pd}^{SI}) - (E(\mathrm{Pd}_{32}\mathrm{H}_{16})]. \quad (4.11)$$

The positive sign of E_{SI} is an indication that the Pd self-interstitial tends to move away from the cluster. These calculated results are listed in Table 4.8. For comparison, the

Table 4.8: Energy of a self-interstitial Pd atom induced by an n-atom helium cluster calculated with a $Pd_{32}H_{16}$ supercell. E_{SI} is defined in Eq. 4.11 and is in reference to the energy of an isolated self-interstitial Pd in the host matrix.

n	5	6
E_{SI} (eV)	-0.57	0.22

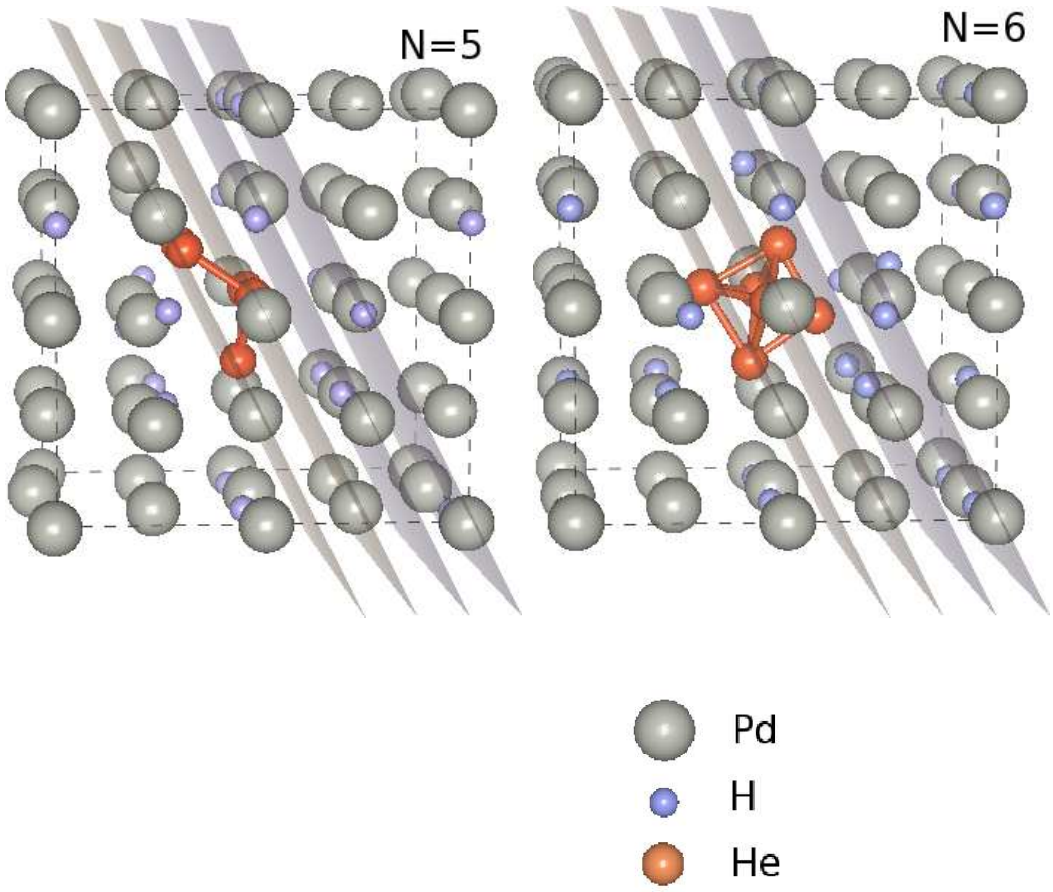

Figure 4.10: Structures of He clusters containing five and six atoms near a Pd-vacancy in the $Pd_{31}H_{16}$ supercell. A set of (420) lattice planes are highlighted showing H-rich (blue) and H-free (gray) region in the supercell.

Table 4.9: Binding and atomic attachment energies (eV) of He clusters at a Pd-vacancy site in the $Pd_{31}H_{16}$ supercell.

n	E^b	E^b / n	E^{Attach}
1	-2.09	-2.09	-2.09
2	-3.39	-1.70	-1.29
3	-4.51	-1.50	-1.12
4	-5.07	-1.27	-0.55
5	-5.44	-1.09	-0.37
6	-6.83	-1.14	-1.39

cluster formation in the presence of a Pd-vacancy is also evaluated. The binding energies of these clusters are

$$E^b(\mathrm{He}_n, \mathrm{Pd}_{31}\mathrm{H}_{16}) = E(\mathrm{Pd}_{31}\mathrm{H}_{16}\mathrm{He}_n) - E(\mathrm{Pd}_{31}\mathrm{H}_{16}) - nE^i(\mathrm{He}, \mathrm{Pd}_{32}\mathrm{H}_{16}). \quad (4.12)$$

This binding energy and the derived atomic attachment energy of the cluster are given in Table 4.9. The structures of clusters containing five and six atoms are illustrated in Fig. 4.10, in which a Pd-vacancy is in the middle of the crystal. The atomic attachment energies are also plotted in Fig. 4.11 to illustrate the process of helium cluster formation in the hydride.

In conclusion, the change of the cluster structures and the binding energies due to the concentration and the long-range ordering of H can be obtained from first-principles calculations. In comparison to the results for $PdH_{0.25}$, the energy gain due to clustering is less significant in $PdH_{0.5}$. After creating a vacancy defect through a self-trapping mechanism, the cluster tends to be more spherically shaped and the atomic attachment energy gets lower, indicating the tendency to form a larger cluster in the presence of a vacancy.

4.4 He in $PdH_{0.75}$

4.4.1 Interstitial Helium

$PdH_{0.75}$ is modeled using a supercell with a combination of $Pd_{32}H_{24}$, inside which hydrogen atoms are located sequentially on the (420) planes in real space with three planes occupied by H followed by one unoccupied plane. This structure is shown in Fig. 4.12(a). The

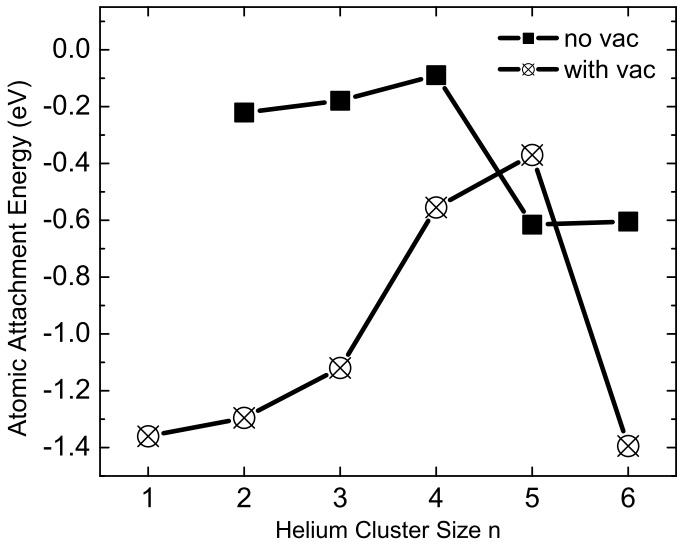

Figure 4.11: Atomic attachment energies for He clusters inside the $Pd_{32}H_{16}$ (solid square) and $Pd_{31}H_{16}$ (open circle) supercell.

ordering of H has the $D0_{22}$ structure with O_{4h}^{19} (or Immm) symmetry. When helium is initially placed at a tetrahedral site, it relaxes back to an octahedral position. However, a metastable state is found at the middle point between the two unoccupied octahedral sites in the system. The metastable state, represented by solid rectangles in the inset of Fig. 4.12(a), is surrounded by two Pd atoms and two H atoms. The distances to the nearest Pd and H atoms are 1.88 Åand 1.92 Å, respectively. The results for helium at different interstitial positions are summarized in Table 4.10.

Table 4.10: Binding energies for a helium atom at the octahedral (O_h) site and a metastable state (D_{4h}) in $Pd_{32}H_{24}$ as defined in Eq. 4.2 with l=32, m=24. The number of the nearest-neighboring (NN) H atoms and the He to H distance (d_{He-H}) are also listed.

	E^b(He)	n.n. H atoms	d_{He-H}
O_h	2.94 eV	12	2.90 Å
D_{4h}	3.78 eV	2	1.92 Å

Table 4.11: Integrated electron charge, in unit of electrons, within a radius of R centered at an octahedral site in the the Pd hydrides with various H concentrations.

	Total electrons at an octahedral site			
R (Å)	pure Pd	$PdH_{0.25}$	$PdH_{0.50}$	$PdH_{0.75}$
0.5	0.07	0.06	0.06	0.05
0.6	0.13	0.12	0.12	0.11
0.7	0.24	0.20	0.19	0.18
0.8	0.37	0.33	0.32	0.29
0.9	0.59	0.52	0.50	0.48
1.0	0.91	0.83	0.75	0.72
1.1	1.41	1.25	1.16	1.09
1.2	2.13	1.86	1.74	1.64

4.4.2 Helium Diffusion

In $PdH_{0.75}$, every empty octahedral site is surrounded by 12 hydrogen atoms at the nearest octahedral site, and the next unoccupied octahedral site is the neighbor at the (211) coordinate with a separation of $\sqrt{5}a_0$ / 2 (= 4.58 Å). The inset of Fig. 4.12(a) illustrates a possible diffusion path in which the dashed line connects the unoccupied octahedral sites (circles) and transition states (rectangles) on the (420) plane. The potential energy of the diffusion path obtained using the NEB method is shown in Fig. 4.12(b). The energy zero is chosen at the octahedral site. The diffusion coordinate on the x-axis ranges from an octahedral site, via the transition state, to the next octahedral site along the $\langle 420 \rangle$ direction. The calculated diffusion barrier is 0.78 eV, which is much higher than those found in $PdH_{0.25}$ and $PdH_{0.5}$.

4.5 Electronic Properties

For the He atom, with its closed-shell electronic structure, a lower charge density at the interstitial sites yields a lower binding energy for helium at that site. Table 4.11 lists the integrated electronic charges within a radius of R centered at an octahedral site in each hydride. It is clearly shown that the charge density around the octahedral site is decreasing when the H concentration becomes higher. This trend is consistent with the binding energies of He found in these hydrides.

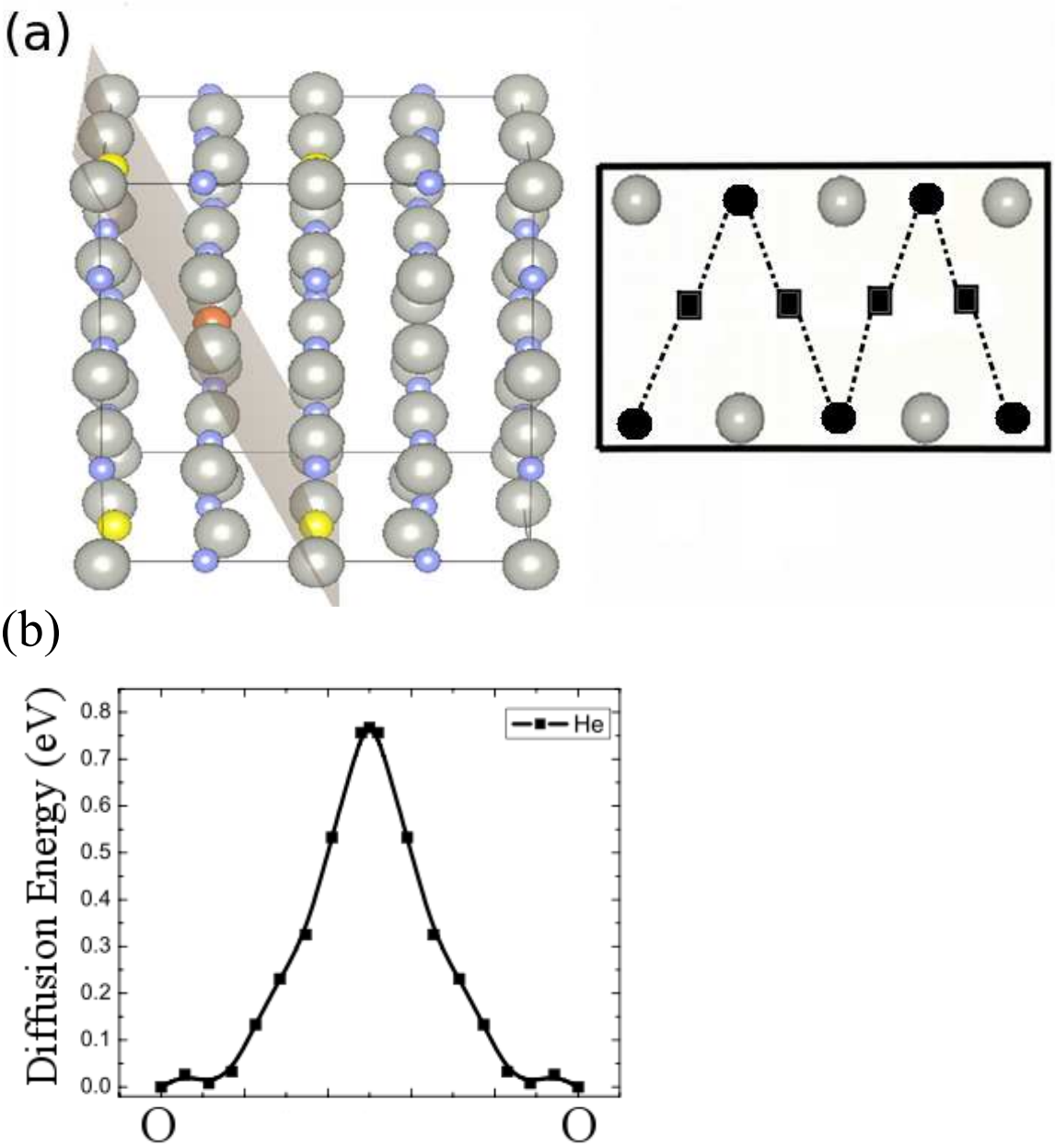

Figure 4.12: (a) An illustration of the He diffusion path in the $Pd_{32}H_8$ supercell. Grey (big) and blue (small) spheres represent Pd and H atoms in the hydride. Orange and yellow spheres represent the He atom and the nearest-neighbor empty octahedral sites. A helium atom diffuses directly between two empty octahedral sites in the $\langle 420 \rangle$ direction. The inset on the right illustrates the diffusion path in which the dashed line connects the neighboring octahedral sites (solid circles) on the (420) plane. The solid rectangles denote for saddle points on the plane. (b) Potential energies of He with respect to the energy at the octahedral site using the NEB method.

(a) (110) plane

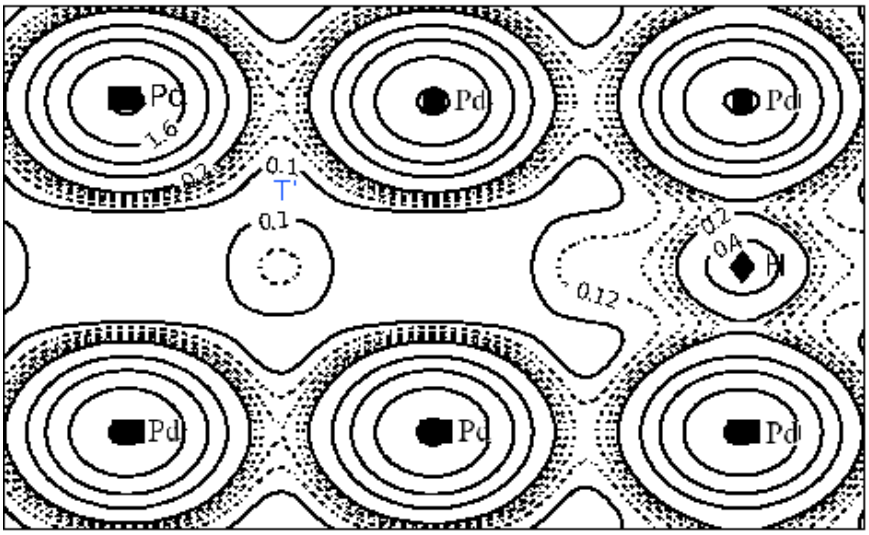

(b) (420) plane

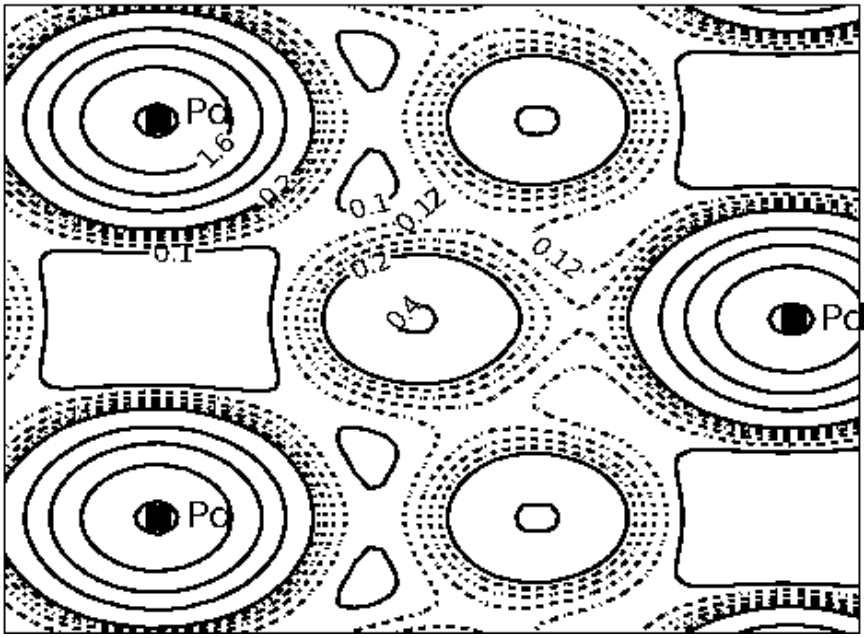

Figure 4.13: Charge density plot, in unit of electrons/Å^3, of the $Pd_{32}H_{16}$ supercell on the (a) (110) and (b) (420) planes. The solid squares, diamonds, and circles represent Pd atoms, H atoms, and empty octahedral sites, respectively. The ratio of two consecutive solid contours is 2.0. Between the contours of 0.1 and 0.2, dash-doted contours with a separation of 0.02 are added.

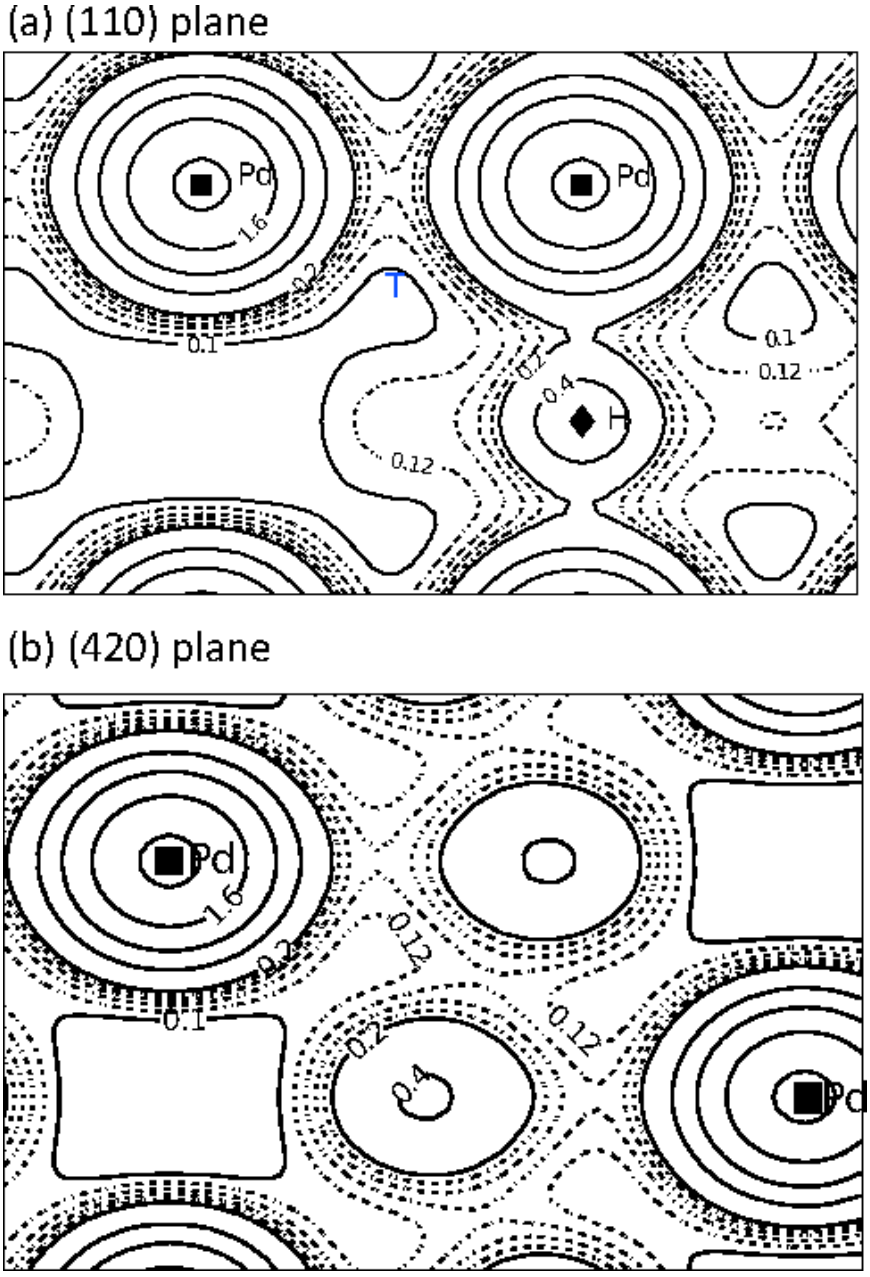

Figure 4.14: Charge density plot, in unit of electrons/Å^3, of the $Pd_{32}H_{24}$ supercell on the (a) (110) and (b) (420) planes. The solid squares, diamonds, and circles represent Pd atoms, H atoms, and empty octahedral sites, respectively. The ratio of two consecutive contours is 2.0. Between the contours of 0.1 and 0.2, dash-doted contours with a separation of 0.02 are added.

The change of the charge density in the interstitial region other than octahedral site is important for helium diffusion in the hydrides. The total charge density plots on the (110) and (420) planes for the $PdH_{0.5}$ and $PdH_{0.75}$ systems are illustrated in Fig. 4.13 and 4.14, respectively. In Fig. 4.13, charge density around the position close to a tetrahedral site on the (110) plane is comparatively lower than that around the transition state between two minimal positions on the (420) plane . For $PdH_{0.75}$, as shown in Fig. 4.14 (a), no tunnel of low charge density region between the minimal positions is found on the (110) plane. The charge density along the diffusion path on the (420) plane in this tritide is shown in Fig. 4.14 (b).

To understand the binding properties of a He atom in these Pd hydrides, we further calculate the projected density of state (PDOS) and the charge distribution for an He atom inside the Pd-H supercells. The angular momentum decomposed DOS is projected on individual atoms. We chose atomic radii R = 1.43 Å, 0.60 Å, and 0.85 Åfor Pd, H, and He atoms, respectively. The results are demonstrated in Fig. 4.15 for three H concentrations. The electronic states can be divided into three energy regions below the Fermi levels E_f. A lower energy band, from -15 to -13 eV, mainly consists of the He 1s-state. A middle energy band, from -10 to -5 eV, is a mixture of H s-state and Pd states. And a high energy band, from -5 eV to E_f, consists of mainly Pd states with a small amount of excited He 2s-states. H attracts electrons originally associated with Pd states to form mainly an s-orbital around its site. The overall density of states is far below the Fermi level. For Pd hydrides, the down-shift of electron states leads to a better alignment of Pd d-states with He 2s-states, and in turn lowers the He binding energies found in these hydrides.

To quantify the charge distribution at the He site, a band-decomposed charge density is calculated for the lowest and highest levels in the PDOS plots. Table 4.12 lists the integrated charge inside a sphere of radius R for the lowest band and highest band on the He site in the three hydrides. As a result, part of the electrons at the He site are excited to the higher energy level in the interaction with the Pd orbitals, and the population of the excited states at the helium site declines as the H concentration x goes higher from 0.25 to 0.75.

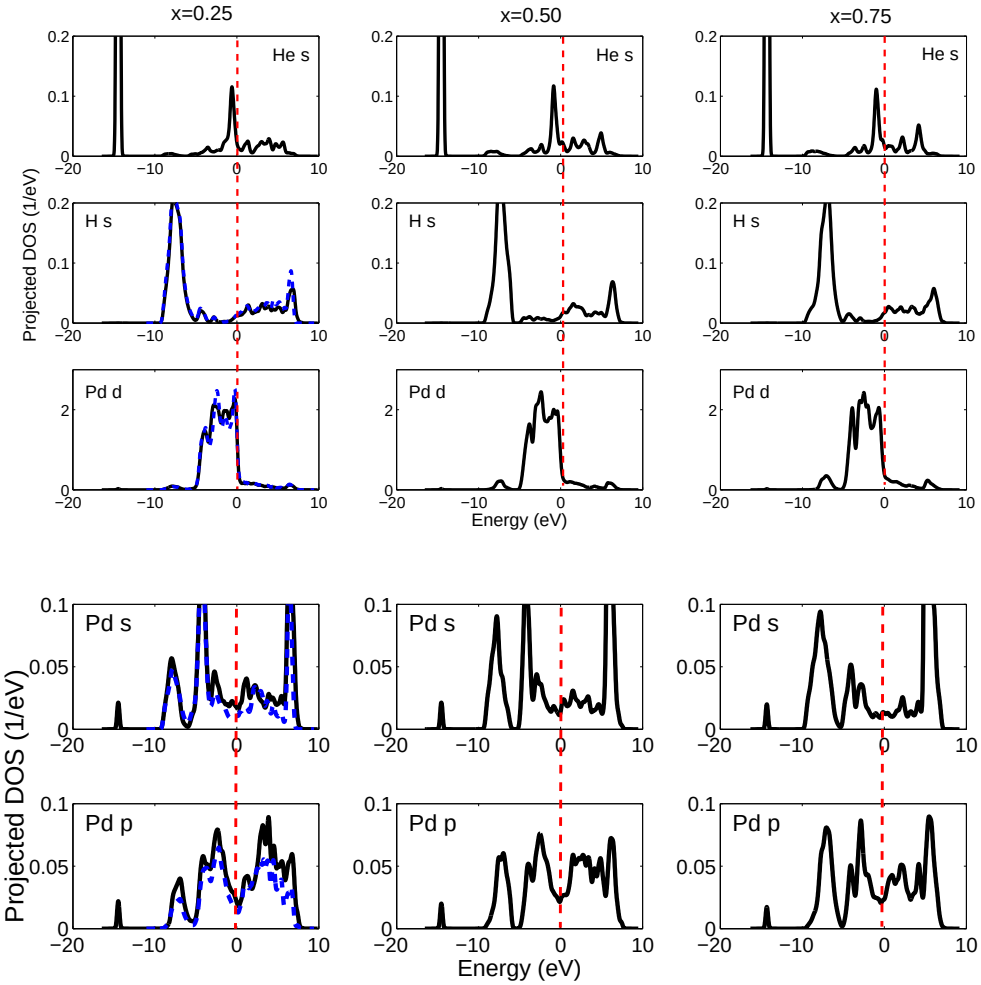

Figure 4.15: Angular momentum decomposed electronic density of states projected onto individual atoms for $Pd_{32}H_8He$ (left), $Pd_{32}H_{16}He$ (middle), and $Pd_{32}H_{24}He$ (right). The Fermi level is set to zero.

Table 4.12: Calculated electronic charge, in units of electrons, for the $1s$ and $2s$ bands at the He site in Pd hydrides with various H concentrations.

		$Pd_{32}H_8$		$Pd_{32}H_{16}$		$Pd_{32}H_{24}$	
R (Å)	He atom	$1s$	$2s$	$1s$	$2s$	$1s$	$2s$
0.5	1.08	0.97	0.11	0.98	0.10	0.97	0.10
0.6	1.31	1.22	0.14	1.23	0.14	1.22	0.13
0.7	1.52	1.38	0.17	1.39	0.16	1.40	0.16
0.8	1.65	1.53	0.22	1.54	0.21	1.52	0.20
0.9	1.76	1.64	0.29	1.64	0.28	1.64	0.27
1.0	1.83	1.72	0.41	1.72	0.39	1.72	0.36
1.1	1.88	1.78	0.59	1.79	0.58	1.78	0.52
1.2	1.92	1.83	0.86	1.84	0.86	1.83	0.77

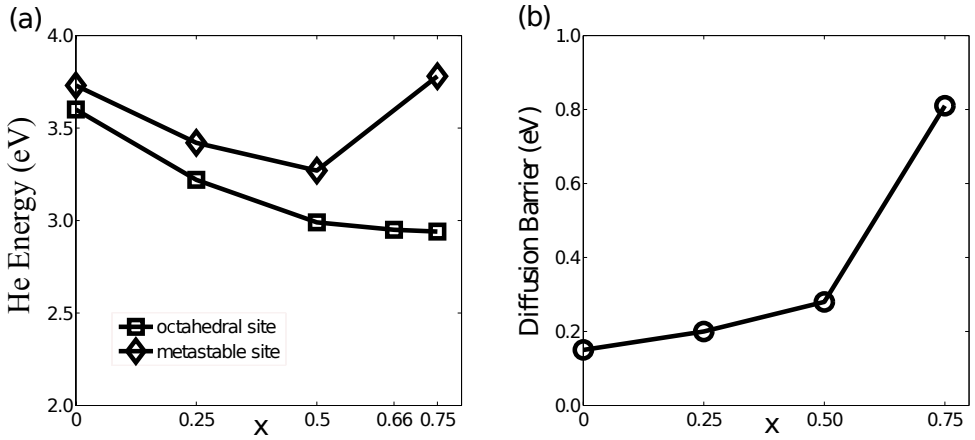

Figure 4.16: Energetics of an interstitial helium atom in palladium hydrides PdH_x with various hydrogen concentrations. The energies of a helium atom at different interstitial sites relative to that of a free atom are compared for concentrations $x = 0.25$, 0.50, 0.66, 0.75. The diffusion barriers of interstitial helium are evaluated for $x = 0.25$, 0.50, and 0.75.

In conclusion, the role of H in the Pd-H-He system is to modify the Pd electronic states through the interactions with the metal hosts. Little direct interaction between He and H is found. The electronic structure of He itself hardly changes at various H concentrations.

4.6 Summary

We have calculated helium defects including a single helium atom and helium clusters inside palladium hydrides PdH_x with various hydrogen concentrations. The binding energies of a helium atom at different interstitial sites are compared for concentrations $x = 0.25$, 0.50,

0.66, 0.75. The diffusion barriers of interstitial helium are evaluated for $x = 0.25$, 0.50, and 0.75. The results are shown in Fig. 4.16. The interaction between Pd and H produces a different electronic environment for He inside the Pd hydrides in comparison with the pure palladium bulk. The energy of He at the octahedral site is lowered in the system with a higher hydrogen concentration. The charge density at the octahedral site also decreases. The existence of ordered hydrogen atoms affects the helium diffusion dynamics due to a repulsive interaction between hydrogen and helium. We find the diffusion barrier increases from 0.13 eV to 0.78 eV as the H concentration goes from $x = 0$ to 0.75.

We have investigated the structure and the growth of helium clusters up to six atoms at x=0.25 and x=0.50. We find both the binding and the atomic attachment energies for the cluster decreases in the hydride with increasing hydrogen concentration. It may indicate that the cluster form more easily in the lattice when fewer hydrogen atoms are around. A Frenkel defect produced by a cluster of n helium atoms when $n > 5$ is found in these two Pd hydrides. The cluster then occupies the vacancy and reconfigures to a lower energy structure. The cluster formed in such a way has a similar structure as those found in the system starting with the presence of a Pd vacancy.

CHAPTER V

HELIUM INSIDE PALLADIUM ALLOYS

In addition to understanding the behavior of helium in the pure Pd system, we extend our study to explore how the helium properties are modified in binary Pd alloys. In particular, we focus on the elements which are close to Pd in the periodic table, such as Cu, Ag, Au, and Pt. These alloys have drawn both theoretical and application interests for their solubility and mechanical strength in the context of hydrogen processing and storage [41, 86, 95, 97]. These alloys also provide better elastic properties, which helps to reduce the embrittlement damage in absorption and desorption of hydrogen atoms, and hence improves the operational lifetime [87, 91, 92]. These advantages of palladium alloys can also be applied to facilitate the storage and processing of the radioactive hydrogen isotope, tritium (^{3}H). However, the understanding of the alloying effect on the retention of helium bubbles created from tritium decay in the alloyed tritide is relatively limited to date.

In a recent experimental study, Thiebaut et al. [43] investigated the aging behavior of $Pd_{90}Pt_{10}$ and $Pd_{90}Rh_{10}$ tritides for tritium storage. They found that fewer He bubbles with induced dislocation loops are generated in $Pd_{90}Pt_{10}$; the aging behavior is mostly unchanged in $Pd_{90}Rh_{10}$, in comparison with that in the pure Pd lattice. Atomic simulation is thus required to understand the interaction between He and different alloying atoms [52].

A few first-principles calculations have been conducted recently for metal alloys and alloyed tritides. Henriksson [88] calculated the energetics of the configuration of multiple He and Fe atoms in bulk Cr. The substitution of Fe yields strongly-bound states for He atoms in the Cr-Fe alloy. Wu et al. [90, 89] studied He and He dimers in TiT_2 alloying with 3d and 4d metal atoms. The energetics of the system is found to be related to the bond order between He and the alloying elements. Although these studies all concluded that He binds strongly with the alloying elements in the metals, we find that it is not necessarily the criterion to retain He atom in some systems. In addition, the diffusion of He atoms in

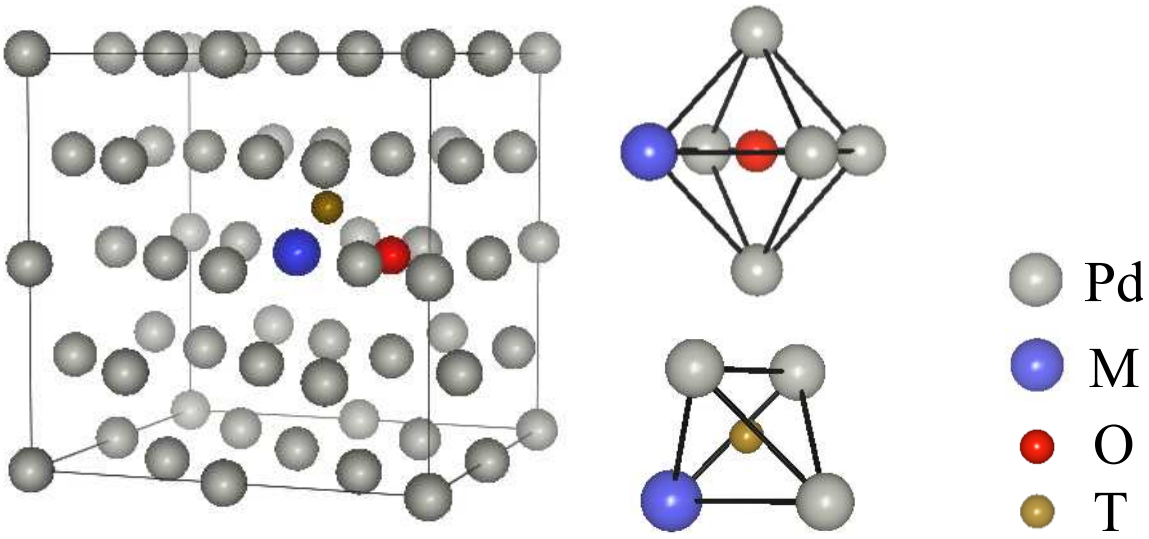

Figure 5.1: The structure of the dilute model $Pd_{31}M$, which has one substitutional alloying atom (M) in a 32-Pd supercell. The gray and blue spheres represent Pd and alloying atoms, respectively. The octahedral and tetrahedral sites near the alloying atom are denoted by red and yellow spheres, respectively.

the alloys, to the best of our knowledge, has not been considered in the literature.

In this chapter, we use first-principles calculations to study the properties of He in various Pd alloys at different concentrations. For comparisons, we also examine similar properties for the H atom inside Pd alloys. The binding energy for a helium or hydrogen atom essentially depends on the alloying element and the alloy concentrations. Elements like Pt or Au are found to increase the activation energy of He migration, which can hinder the mobility of helium atoms and prevent He atoms from clustering. The results are supportive of previous experiment as findings and provide a good understanding of He retention properties in Pd-based alloys.

5.1 Computational Methods

Our calculations are performed within the density functional theory (DFT) formalism using the Vienna *ab initio* Simulation Package VASP [69, 60]. The plane-wave basis set with Blöchl's projector augmented wave (PAW) method [62] is also implemented in VASP [68] to solve the Kohn-Sham equations. The configurations of Pd $5s^1 4d^9$, Pt $6s^1 5d^9$, Cu $3d^{10} 4p^1$,

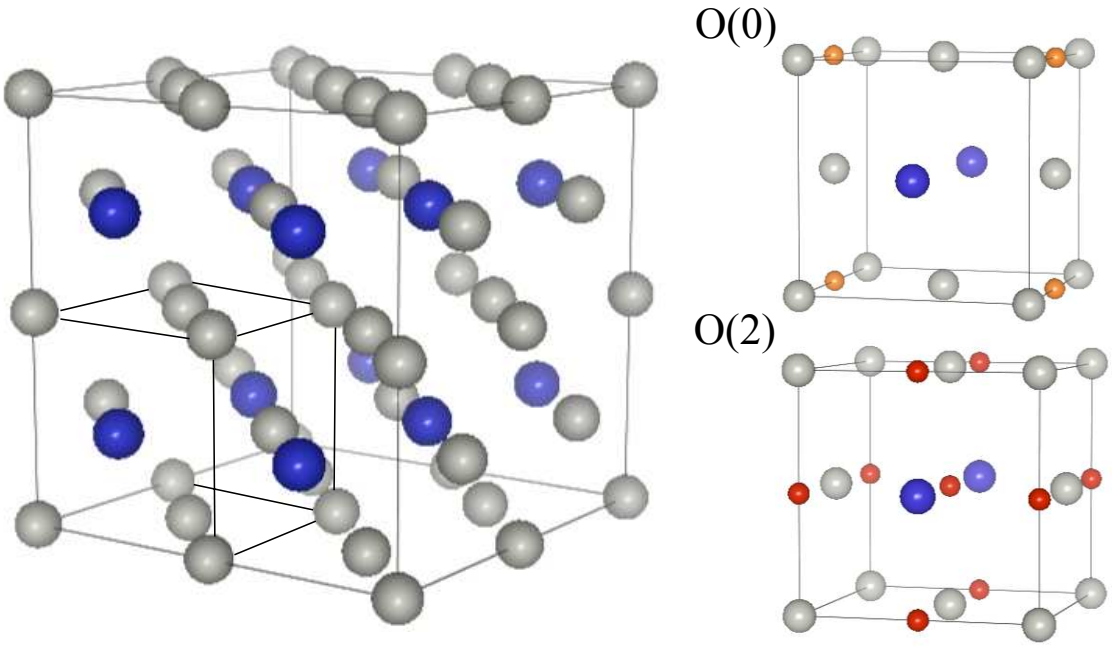

Figure 5.2: The structure of an ordered Pd alloy system with the $L1_2$ symmetry. It consists of 25 at. % of the alloying element (M). The gray and blue spheres represent the Pd and alloying atoms, respectively. O(0) (dark orange) is the octahedral site surrounded by Pd atoms only, and O(2) (light orange) is surrounded by two alloying atoms and four Pd atoms.

Ag $5s^1 4d^{10}$, and Au $6s^1 5d^{10}$ are treated as valence states. All the metal alloys are studied with non-spin-polarized calculations. Exchange and correlation functionals are within the generalized gradient approximation (GGA) of the Perdew and Wang (PW91) functional [63]. The plane wave energy cutoff and the k-point sampling [58] are properly chosen in order to have an energy convergence within 1 meV per atom. In this study, the energy cutoff is 500 eV, and the k-grid sampling is within 0.01 $\mathring{A}^{-1}$. The supercell approach is applied to model a single He atom or a He cluster defect in the system. The calculations are done with all atomic positions fully relaxed in the supercell.

In this study, we consider two models with different alloying concentrations. The first one is a dilute model with one substitutional foreign atom in a Pd_{32} supercell. A structure of $Pd_{31}M$ is shown in Fig. 5.1, where the gray spheres represent Pd atoms and the blue ones represent the alloying metal (M). The nearest octahedral (O) and tetrahedral (T) sites to the alloying element are illustrated in the figure. The lattice constant is kept the same as

that of pure Pd metal. The long range interaction of foreign atoms is expected to be small due to the dimension of the supercell. The second model is an ordered structure with 25 % of the alloying element. We choose the $L1_2$ structure for the calculation, as illustrated in Fig. 5.2. Each alloy is fully relaxed to its equilibrium lattice constant. The interstitial regions in this configuration become less homogeneous. There are two types of octahedral sites, O(2) and O(0), and one type of tetrahedral site, T(1). The number in parenthesis indicates the coordination number of the alloying element. O(2) is surrounded by four Pd and two alloying atoms, and O(0) is surrounded by six Pd atoms. The ratio of O(0) to O(2) is 1:3.

The formation enthalpy of binary Pd alloys, which determines the stability of the system, is defined as follows:

$$\Delta H(\mathrm{Pd}_{1-x}\mathrm{M}_x) = E(\mathrm{Pd}_{1-x}\mathrm{M}_x) - (1-x)E(\mathrm{Pd}) - xE(\mathrm{M}), \tag{5.1}$$

where $E(\mathrm{Pd}_{1-x}\mathrm{M}_x)$ is the total energy of the $\mathrm{Pd}_{1-x}\mathrm{M}_x$ alloy, and $E(\mathrm{Pd})$ and $E(\mathrm{M})$ are total energies per atom of bulk Pd and M, respectively. We start with one helium atom in the interstitial site per supercell. The binding energy of a hydrogen or a helium atom is given relative to the energy of the host metal and of an isolated hydrogen molecule or an isolated helium atom, respectively:

$$\begin{aligned} E^b(\mathrm{H}) &= E(\mathrm{Pd}_l\mathrm{M}_m\mathrm{H}) - E(\mathrm{Pd}_l\mathrm{M}_m) - \frac{1}{2}E(\mathrm{H}_2) \\ E^b(\mathrm{He}) &= E(\mathrm{Pd}_l\mathrm{M}_m\mathrm{He}) - E(\mathrm{Pd}_l\mathrm{M}_m) - E_{\mathrm{atom}}(\mathrm{He}), \end{aligned} \tag{5.2}$$

where the values of l and m determine the supercell size and the concentration of the metal atoms M.

The diffusion barriers of interstitial H and He atoms are determined by transition state search using the Climbed Image Nudged Elastic Band (CI-NEB) method[61]. Atomic attachment energy, E^{Attach}, is a measure of the energetics for forming an interstitial He dimer. The energy is calculated with respect to the energy of an interstitial He atom:

$$E^{attach}(He_2) = E(\mathrm{Pd}_{24}\mathrm{M}_8\mathrm{He}_2) + E(\mathrm{Pd}_{24}\mathrm{M}_8) - 2E(\mathrm{Pd}_{24}\mathrm{M}_8\mathrm{He}), \tag{5.3}$$

Table 5.1: The heat of formation ΔH for the $Pd_{31}M$ alloys and the calculated binding energy of an interstitial H or He atom at the octahedral (O) and tetrahedral (T) sites next to the alloying elements.

		dilute Pd alloys				pure
		Cu	Ag	Au	Pt	Pd
ΔH (eV)		-0.20	-0.04	-0.15	-0.10	
E^b (eV)						
H	O	-0.09	-0.06	0.01	0.00	-0.12
	T	-0.07	0.03	0.13	0.04	0.08
He	O	3.27	3.59	3.68	3.79	3.60
	T	3.35	-	-	-	3.73

where E ($Pd_{24}M_8He_2$) is the total energy with a He dimer along the $\langle 110 \rangle$ direction in the $Pd_{24}M_8$ supercell.

5.2 H and He atoms in Dilute Pd Alloys $Pd_{31}M$

To understand the energetics of tritium and helium due to the alloying effect, we calculate the H and He binding energies in the alloyed system. The heat of formation ΔH of the alloy compounds is first examined. A negative value of ΔH indicates that Pd and the alloying elements are thermodynamically mixable. The calculated results, as listed in Table 5.1, show Pd can form stable alloying compounds $Pd_{31}M$ with M = Cu, Ag, Pt and Au. The binding energy E^b for an H or He atom at the octahedral and tetrahedral sites are also tabulated in Table 5.1. The energy for H at the octahedral site next to the alloying atom is higher in comparison with that in pure Pd. But the energy difference between the octahedral and tetrahedral sites is reduced around the foreign atom. For the He atom, the substitutional Cu atom can trap He to the interstitial sites next to it. In Pd-Pt and Pd-Au alloys, it is energetically preferable for He atoms to stay at the Pd-rich interstices. The Ag atom has a minimal impact on the He binding energy in bulk Pd. The energy of an H or He atom at the octahedral site next to the alloying element is plotted in Fig. 5.3, in which the energy zero is chosen at the binding energy of an H or He atom in the pure Pd supercell.

To lower the energy of the system, the He atom located at some stable site will distort the positions of the surrounding metal atoms. Table 5.2 lists the displacements of the metal

atoms around helium at the minimum energy configuration. The listed value is the distance between the He atom to the surrounding metal atoms (five Pd and one M atom) in terms of the distance in the Pd bulk, d_0=2.14 $\AA$. The results are consistent with the He energy listed in Tabel 5.1. The Cu atom, with a smaller atomic radius, attracts He at the nearby interstitial site, while the Au and Pt atoms have the opposite effect.

5.3 H and He atoms in Ordered Pd Alloys $Pd_{24}M_8$

5.3.1 Sites Preference

The site preference of an H or He atom is determined in the systems of $Pd_{24}M_8$, with M=Cu, Ag, Pt, and Au. Table 5.3 lists the heat of formation and the equilibrium lattice constant for the Pd alloys. The negative value of the heat formation indicates that these alloy compounds are energetically favorable compared with individual metals. Alloying with Cu causes a contraction of the lattice constant, while substituting Ag or Au causes a lattice expansion. $Pd_{24}Pt_8$ has the minimal change of the lattice constant.

Binding energies for both H and He atoms at the three different interstitial sites using Eq. 5.2 are listed in Table 5.4. For all four alloys, the H atom favors occupying O(0) over O(2). The energy changes at the O(0) site is found to be correlated with lattice constant of the alloys, indicating that the geometry effect determines the H energy. In comparison, the energy at the O(2) site follows the same trend as that in the dilute alloy, indicating that the ligand effect (from the neighboring atoms) is most important at this interstitial site.

The energy of helium in the alloys has a different trend. In $Pd_{24}Ag_8$, $Pd_{24}Pt_8$, and $Pd_{24}Au_8$ alloys, He has a similar site preference to occupy the O(0) site over the other interstitial sites, indicating that the atom is energetically favorable to stay around Pd atoms

Table 5.2: The distance change between the He atom and the surrounding metal atoms in $Pd_{31}MHe$ in comparison with that in pure Pd bulk, d_0 = 2.14 $\AA$.

	dilute Pd alloys			
d / d_0	Cu	Ag	Au	Pt
M-He	0.90	1.01	1.08	1.08
Pd-He	1.03	1.00	1.01	1.00

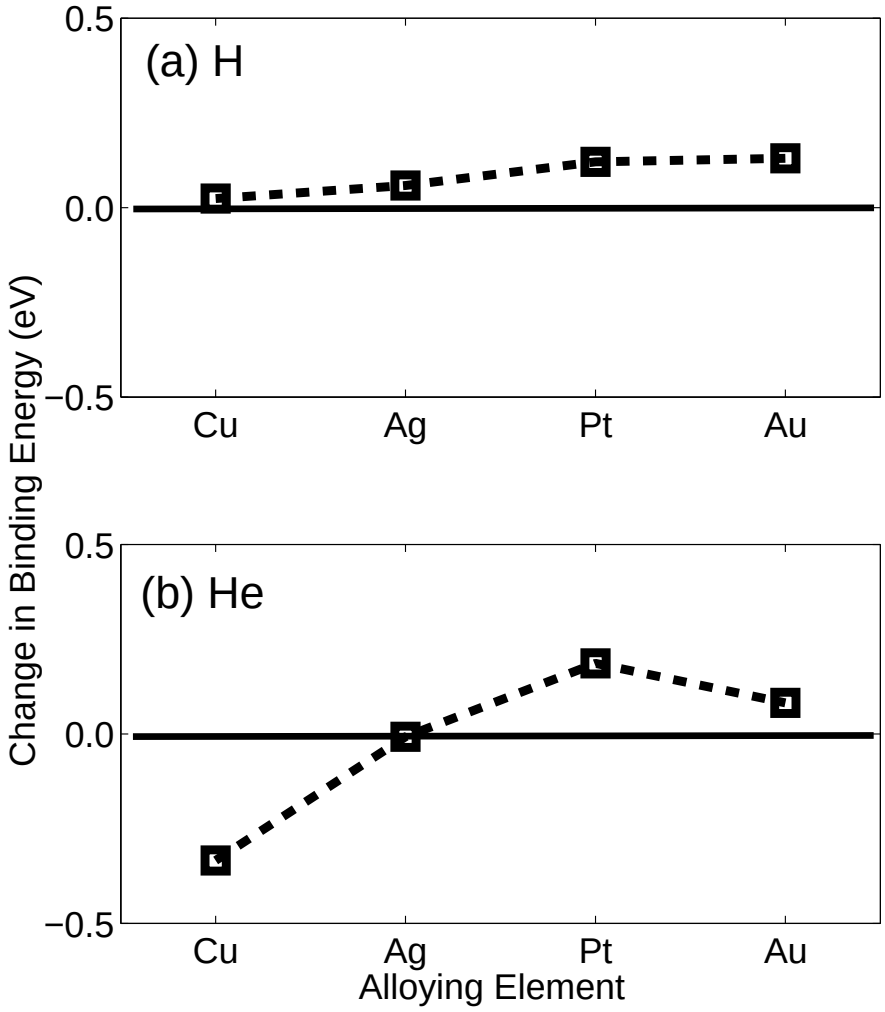

Figure 5.3: The energy change for (a) H and (b) He in the $Pd_{31}M$ alloys with M = Cu, Ag, Au, and Pt. The energy zero is set to be the H or He energy in pure Pd.

Table 5.3: The heat of formation of $Pd_{24}M_8$ and the corresponding lattice constant relative to that of pure Pd, $a_0 = 3.96$ $\mathring{A}$

	Alloying Elements			
	Cu	Ag	Au	Pt
Δ H (eV)	-2.14	-0.74	-1.57	-0.55
lattice constant (a/a_0)	0.98	1.01	1.01	1.00

rather than the alloying elements Ag, Pt, and Au. In $Pd_{24}Cu_8$, however, He prefers to occupy O(2) site energetically. This is consistent with the finding that the Cu atom lowers the He energy in the dilute model. The results of the energy changes for H and He atoms in the Pd alloys are summarized in Fig. 5.4, where the reference energy is chosen at the H/ He energy in pure Pd. The circles and squares represent the energies at O(0) and O(2) sites, respectively.

We further analyze the metal displacements due to the insertion of the He atom. The metal atoms surrounding the He atom are found to shift away from the original lattice position. A larger Pd-He distance is created for the interstitial He atom in $Pd_{24}Ag_8$, $Pd_{24}Pt_8$, and $Pd_{24}Au_8$, but a smaller value is found in $Pd_{24}Cu_8$. Table 5.5 lists the distance between He and the neighboring metal atoms after ionic relaxation. The values are in terms of the He-Pd distance (d_0) in pure Pd.

Table 5.4: The binding energy of an interstitial H or He atom in the ordered $Pd_{24}M_8$ alloys (M=Cu, Ag, Au, and Pt).

		Alloying Elements			
	E^b (eV)	Cu	Ag	Au	Pt
H	O (2)	0.02	0.05	0.14	0.10
	O (0)	-0.02	-0.20	-0.18	0.01
	T (1)	0.06	-0.07	-0.01	0.07
He	O (2)	3.51	3.42	3.64	3.93
	O (0)	4.02	3.22	3.16	3.69
	T (1)	3.64	-	-	4.03

Table 5.5: The nearest-neighbor distance between He and surrounding metal atoms. The value is in terms of the He-Pd distance d_0 in the pure Pd system ($d_0 = 2.14$ $\mathring{A}$).

		Alloying Elements			
	d / d_0	Cu	Ag	Au	Pt
O (2)	He-M	1.00	1.02	1.04	1.03
	He-Pd	0.99	1.01	1.00	1.00
O (0)	He-Pd	0.96	1.02	1.02	1.00

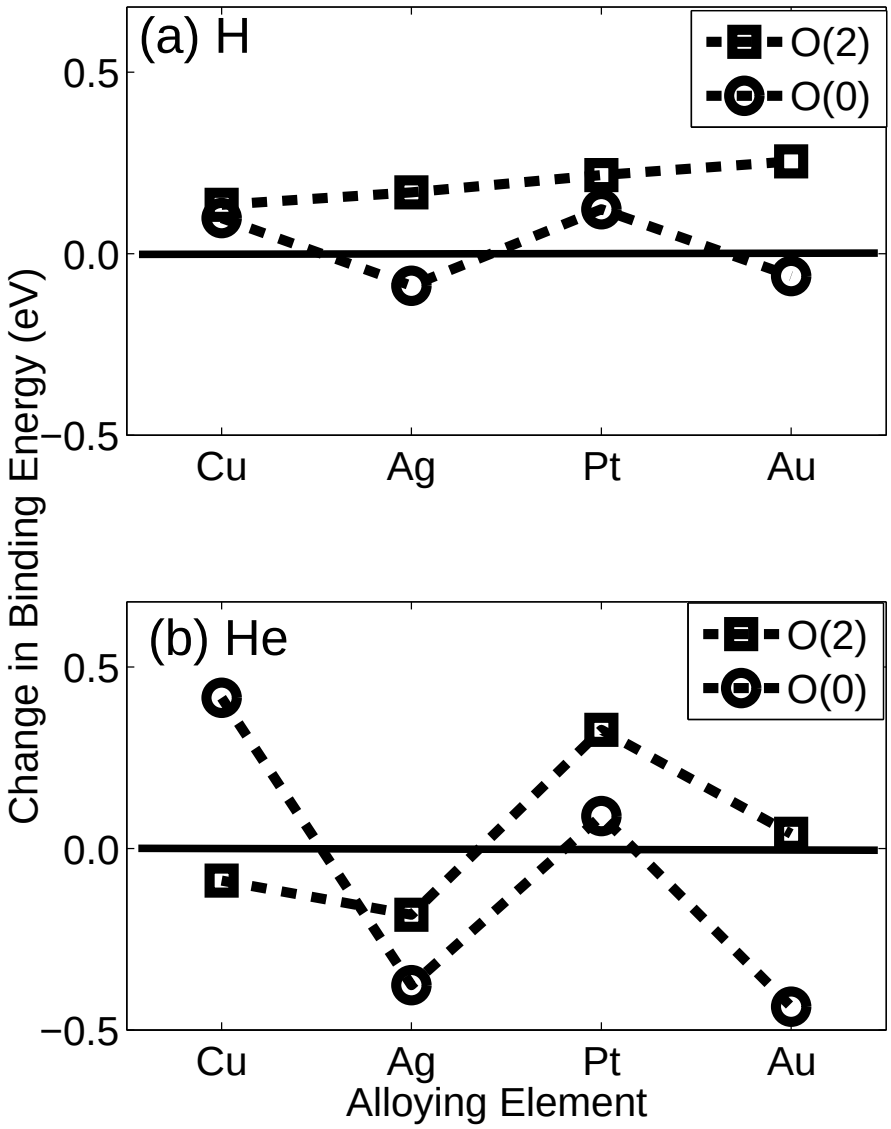

Figure 5.4: The binding energy change for (a) H and (b) He in the ordered $Pd_{24}M_8$ alloys. M stands for the alloying atoms of Cu, Ag, Au, and Pt. The results for two types of octahedral sites O(2) and O(0) are illustrated by squares and circles, respectively. The reference energy is set at the H/ He binding energy in pure Pd.

5.3.2 Valence Charge Distribution

The change of the binding energy for He in Pd alloys can be related to the charge density redistribution at the interstitial sites due to interaction of Pd and alloying elements. Table 5.6 lists the averaged charge density at the two octahedral sites in the relaxed $Pd_{24}M_8He$ systems. The valence electron charge at these sites is calculated by integrating over a sphere of a radius of 1.0, 1.1, and 1.2 $\mathring{A}$. As a result, the averaged charge density is lower at O(2) than O(0) site in $Pd_{24}Cu_8$, hence the He atom energetically prefers to occupy the O(2) site. In the other three alloy systems, the averaged density values are higher at O(2) than O(0), and the He atom prefers to occupy the O(0) site. The relationship for the calculated helium binding energy, He to Pd distance, and charge density distribution at the O(0) sites in the Pd alloys is summarized in Fig. 5.5. The He-Pd distance is in terms of that in the Pd bulk (d_0 = 2.14 $\mathring{A}$). The electron charge density is the calculated density average within the sphere of 1 $\mathring{A}$ radius of the O(0) site, in which the surrounding atoms are frozen at the relaxed structure due to the insertion of an He atom at the site.

5.3.3 Diffusion

The diffusion barriers for H and He atoms in the Pd alloys are determined by the saddle point search using the CI-NEB method. According to the site preference, O(0) over O(2) for H in the $Pd_{24}M_8$ alloys, H prefers Pd rich areas and avoids the alloying elements. Thus, we consider the diffusion processes that allowed H to hop from an O(0) site to another

Table 5.6: The averaged valence charge density (integrated over a sphere of various radii) at the octahedral site in the strained Pd alloys due to the presence of interstitial He.

		Alloying Elements				Pure
ρ (e / $\mathring{A}^3$)	radius (Å)	Cu	Ag	Au	Pt	Pd
	1.0	0.12	0.12	0.12	0.13	
O (2)	1.1	0.13	0.13	0.14	0.15	
	1.2	0.15	0.15	0.16	0.17	
	1.0	0.17	0.12	0.11	0.13	0.13
O (0)	1.1	0.19	0.13	0.12	0.15	0.15
	1.2	0.22	0.15	0.14	0.17	0.18

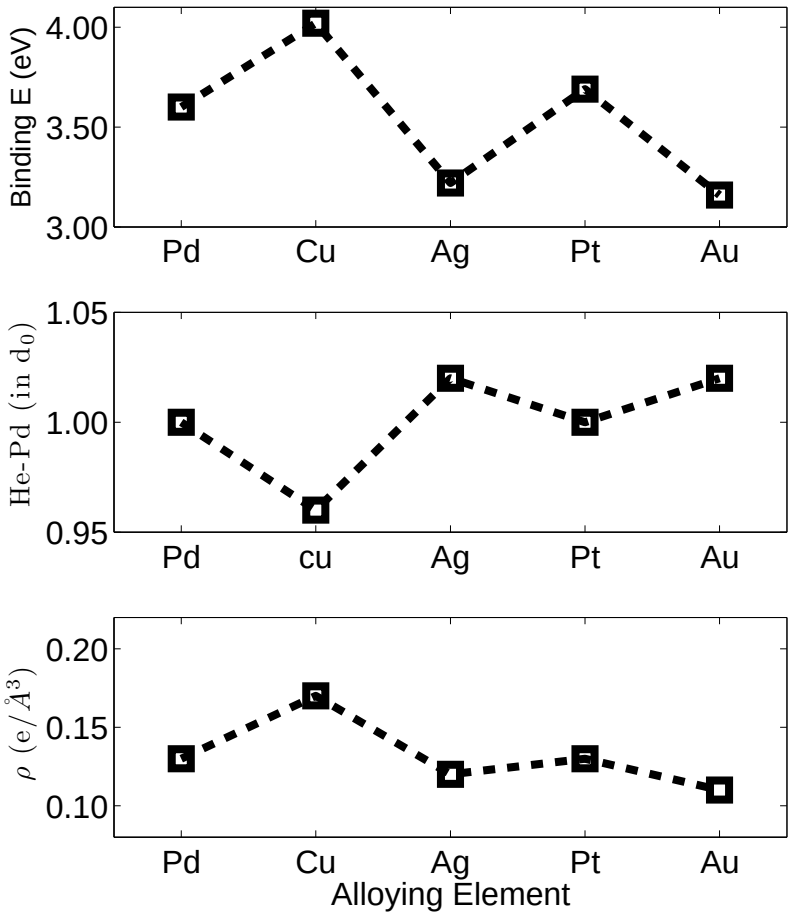

Figure 5.5: The binding energy of an He atom at the O(0) site (top), the corresponding lattice displacement (middle), and averaged charge density (within a radius of 1 Å) (bottom), in Pd and various Pd alloys.

neighboring O(0) site. It is found that H at O(0) first hops to the nearest T(1) along the $\langle 111 \rangle$ direction, goes to a nearby O(2) along one of the other $\langle 111 \rangle$ direction, and then hops to a neighboring O(0) via T(1) in a similar process. This diffusion path is illustrated by the dashed line *a* in Fig. 5.6. The activation energy and diffusion path for each alloy are summarized in Table 5.7.

Since the site preference differs in different alloys, He migrates along different paths from the H diffusion. In $Pd_{24}Cu_8$, the most energetically stable site is O(2). The minimum energy path is the O(2) to T(1) path. Because the barrier from T(1) to O(0) is too high

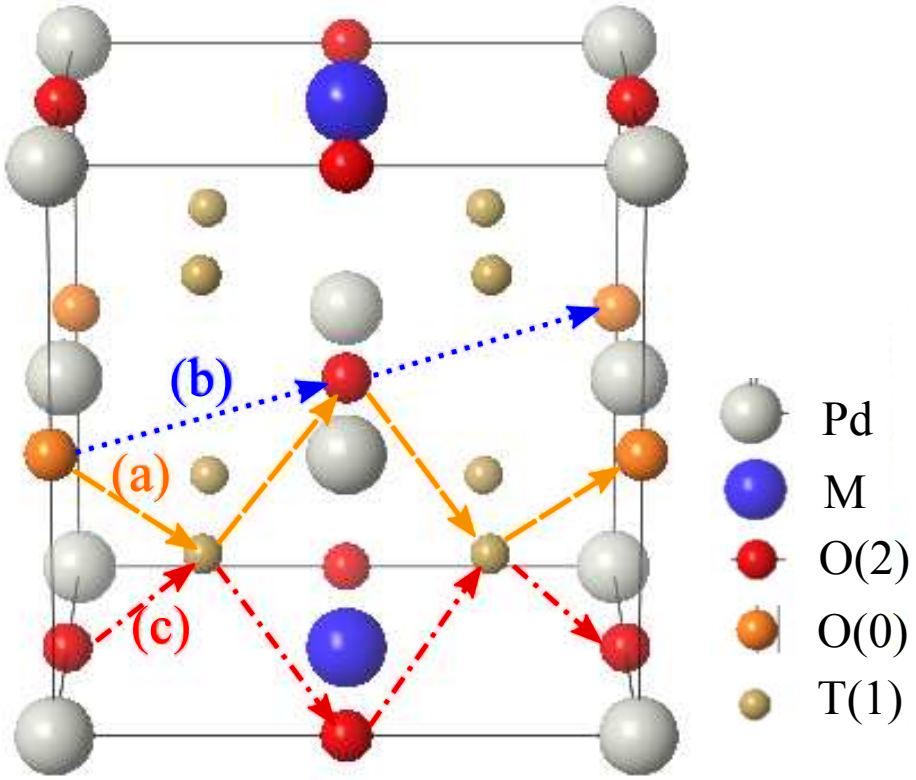

Figure 5.6: Three possible diffusion paths for an interstitial atom in the $Pd_{24}M_8$ matrix: (a) Yellow (dashed) lines denote the path O(0)-T(1)-O(2)-T(1)-O(0), (b) blue (dotted) lines denote the path O(0)-O(2)-O(0), and (c) red (dash-dotted) lines denote the path O(2)-T(1)-O(2).

Table 5.7: The effective activation energies for H and He atoms diffusing through interstitial sites in Pd alloys.

	$Pd_{24}M_8$	E^a (eV)	Diffusion Path
H	Cu	0.08	a
	Ag	0.13	a
	Au	0.17	a
	Pt	0.06	a
He	Cu	0.13	c
	Ag	0.19	b
	Au	0.48	b
	Pt	0.34	a

compared to that from T(1) to O(2), He would not diffuse through O(0) at any appreciable

rate. The atom hops form O(2) to T(1) to O(2) repetitively, as illustrated by the dash-dotted lines (c) in Fig. 5.6. In $Pd_{24}Ag_8$ and $Pd_{24}Au_8$, the configuration of He at T(1) is found to be unstable after ionic relaxations; the He atom migrates from O(0) to O(2) along the $\langle 110 \rangle$ direction. In the NEB calculation no transition state is found between O(0) and O(2) sites in both alloys. Thus, the activation energy is the energy difference between the two octahedral sites. At O(2), He subsequently jumps to O(0) along one of the $\langle 110 \rangle$ directions. The geometry of the path are shown in by the dotted line (b) in Fig. 5.6. In $Pd_{24}Pt_8$, the energetically preferred diffusion path is O(0)-T(1)-O(2)-T(1)-O(0), which is the same as that of an H atom. The results of the He atom diffusion in the alloys are summarized in Table 5.7. The activation energy for He in $Pd_{24}Au_8$ and $Pd_{24}Pt_8$ are found to be 0.48 eV and 0.34 eV, respectively, which are relatively high in the metal alloys in comparison with the other alloys and pure Pd bulk.

5.3.4 Small He Cluster Formation

The interstitial He atom generates a strain field in the alloys which has impact on trapping another He atom in the bulk. The trapping mechanisms of two He atoms forming a He dimer is investigated using the CI-NEB method. The initial states of the two He atoms at octahedral sites are set apart by a distance of $\sqrt{2}\ a_0$ along the $\langle 110 \rangle$ direction. The diffusion path is chosen as one of the He atom moving towards to the other He along the $\langle 110 \rangle$ direction. The energy along the diffusion path in the Pd alloys are shown in Fig. 5.7 with the energy zero set to the initial state energy. The activation energy is found to be 0.14 eV and 0.13 eV in $Pd_{24}Au_8$ and $Pd_{24}Pt_8$, respectively. In $Pd_{24}Cu_8$, $Pd_{24}Ag_8$, and pure Pd, however, the activation energy is found close to 0 eV . The He atomic attachment energy, or pairing energy, of adding a second He atom to form a He dimer of $\langle 110 \rangle$ is shown in Fig 5.8. The straight line represent the He pairing energy in pure Pd. As a result, the atomic attachment energy in the Pd alloys are higher than that in pure Pd, indicating a tendency to suppress cluster formation.

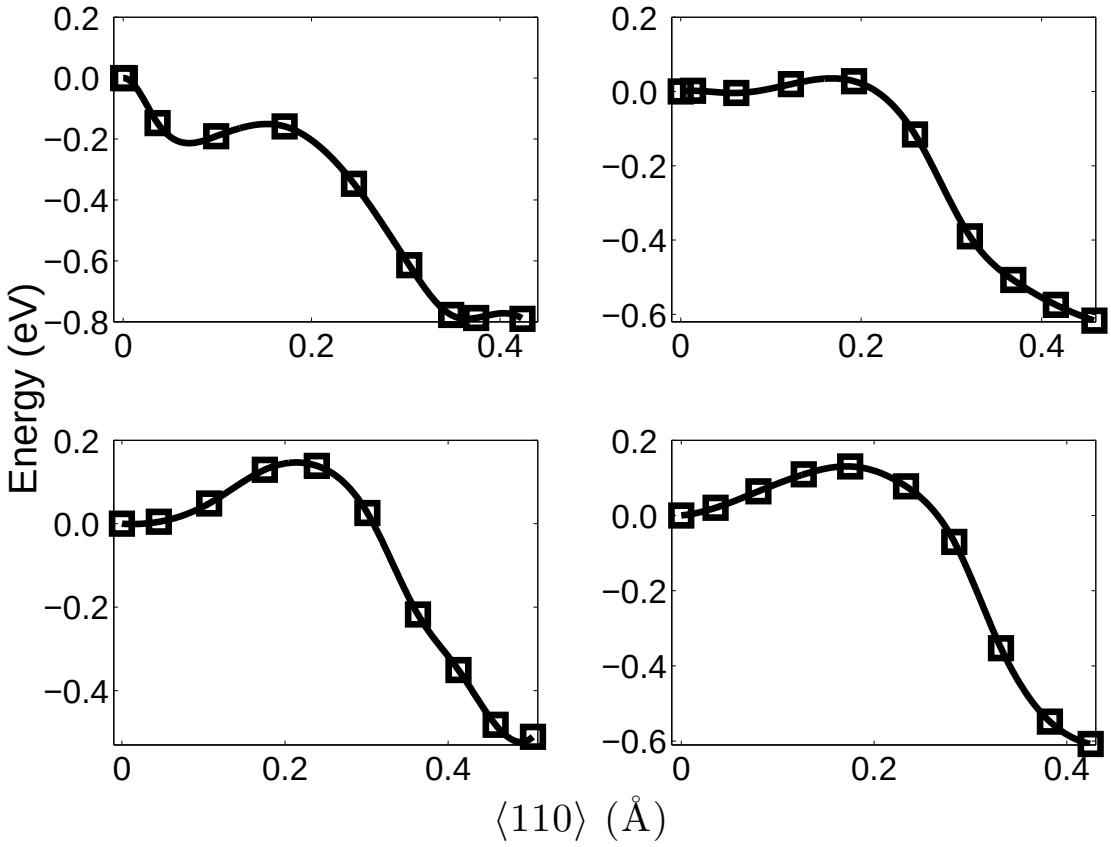

Figure 5.7: Diffusion path of a helium atom moving toward another atom to form a dimer in Pd alloys $Pd_{24}M_8$ (M=Cu, Ag, Au, and Pt) using the CI-NEB method.

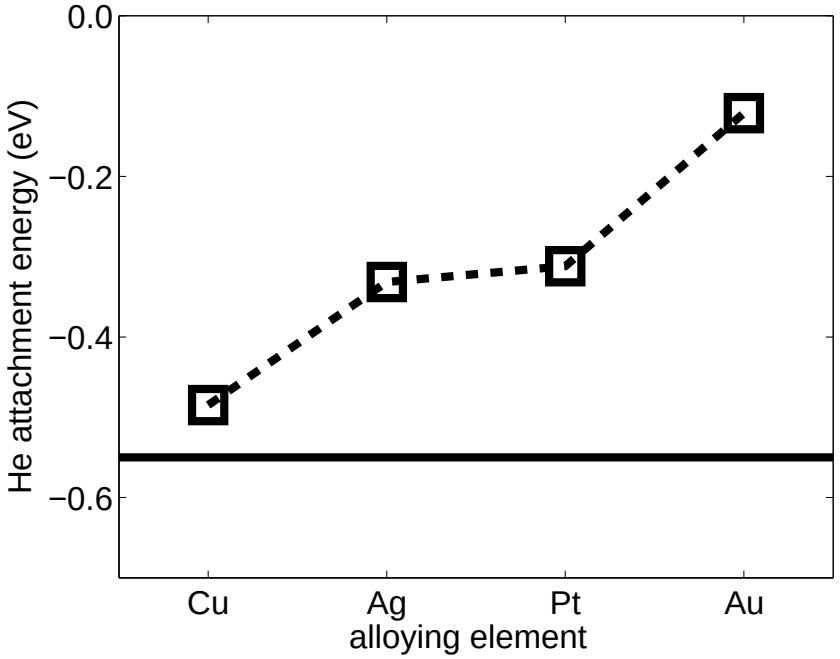

Figure 5.8: The atomic attachment energy of helium atoms defined in Eq. 5.3 to form a helium dimer in $Pd_{24}M_8$ with M = Cu, Ag, Pt, and Au. The solid line represents the value for pure Pd.

5.4 H and He atoms in $Pd_{87.5}Pt_{12.5}$

5.4.1 Structure

To understand the experimental results for the $Pd_{90}Pt_{10}$ system, we use a model of a homogeneous Pd-Pt alloy with 12.5 % of Pt. The Pt atoms are uniformly distributed in the matrix. The structure is illustrated in Fig. 5.9. Due to the different composition of the surrounding metal atoms, two distinct octahedral and tetrahedral sites are found in this alloy. O(1) and O(0) are octahedral centers surrounded by five Pd and one Pt atoms and by six Pd atoms, respectively. The distribution of the O(0) site in this alloy is exactly the same as O(0) in $Pd_{24}Pt_8$, which has the cubic symmetry and accounts for 25 % of total octahedral sites in the solid. T(1) and T(0) are tetrahedral centers of three Pd and one Pt atoms and of four Pd atoms, respectively.

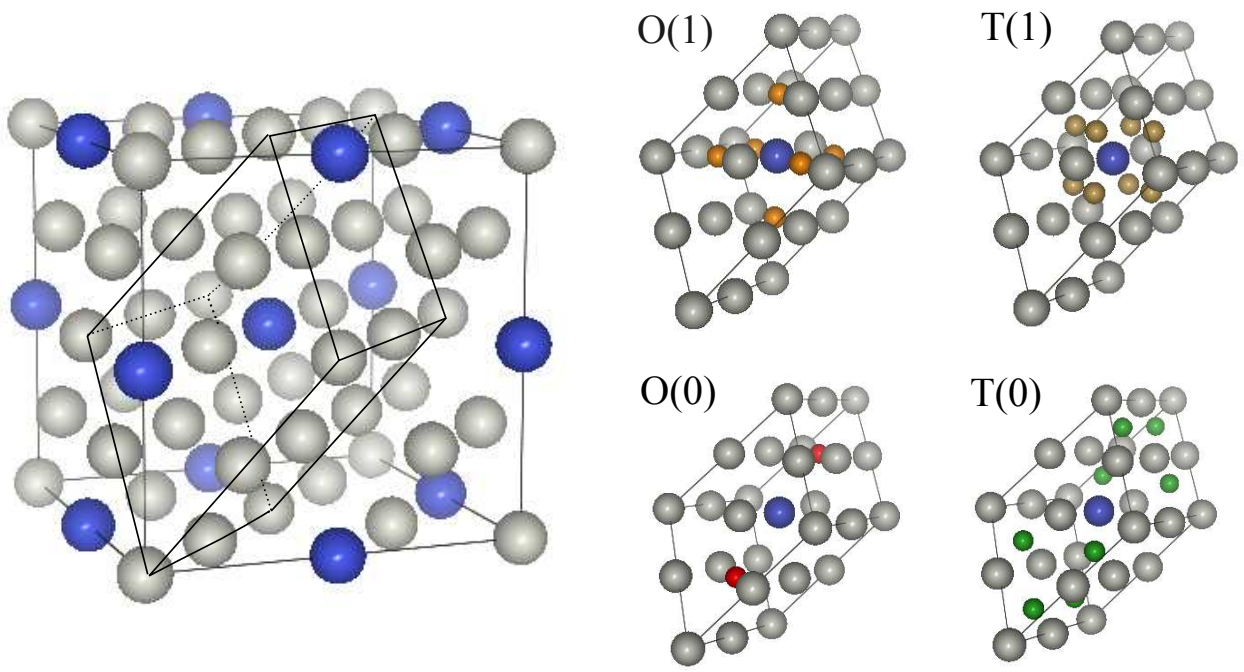

Figure 5.9: The model of a homogeneous Pd-Pt alloy with 12.5 % of Pt. The gray and blue spheres represent the Pd and Pt atoms, respectively. The figure illustrates two distinct octahedral O and tetrahedral T sites due to the different composition of the surrounding atoms. O(1) and O(0) are octahedral centers surrounded by five Pd and one Pt atoms and by six Pd atoms, respectively. T(1) and T(0) are tetrahedral centers of three Pd and one Pt atoms and of four Pd atoms, respectively.

5.4.2 Site Preference and Diffusion

The binding energy E^b of a hydrogen and helium at interstitial sites in the Pd_7Pt alloy is examined for various supercell size. The results are listed in Table 5.8. It is found

Table 5.8: Calculated binding energy for H and He atoms at each interstitial site in $Pd_{87.5}Pt_{12.5}$.

supercell (atoms)		8	32	64
E^b(H)	O(1)	-0.01	0.01	
	O(0)	-0.07	-0.04	
	T(1)	0.11	0.05	
	T(0)	0.02	-0.03	
E^b(He)	O(1)	4.21	3.76	3.82
	O(0)	4.08	3.69	3.75
	T(1)	-	4.03	4.07
	T(0)	-	3.82	3.86

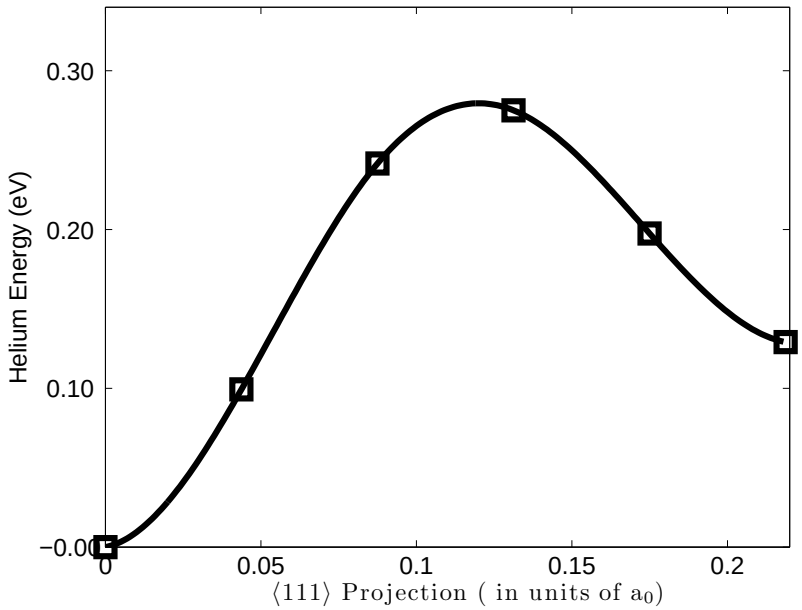

Figure 5.10: Calculated energy along a diffusion path of a helium atom from O(0) to T(0) in the $Pd_{28}Pt_4$ alloy using the NEB method. The effective activation energy is found to be 0.28 eV.

that the octahedral site surrounded by Pd, O(0), is the most favorable state for H and He atoms. The diffusion barrier for the He atom can be then determined by searching saddle points between O(0) and neighboring T(0) or T(1) sites. Using the CI-NEB method, the calculated activation energies from O(0) to T(1) and from O(0) to T(0) are 0.35 eV and 0.28 eV, respectively. The result of the lowest activation energy is illustrated in Fig. 5.10. These diffusion barriers are increased compared with the value of 0.13 eV in the pure Pd bulk. As a result, the He migration rate can be hindered by the presence of Pt atoms. With a reduced diffusion for the He atom, the formation of He clusters can be suppressed. The results are consistent with the experimental observations reported for the $Pd_{90}Pt_{10}$ alloy.

5.5 Summary

We have studied the energetics and diffusion properties of H, He, and He dimer in the fcc Pd alloys with Cu, Ag, Pt, and Au. Two models of a dilute solution and an ordered structure with 25 % of alloying elements are investigated with first-principles calculations. The He binding energy largely depends on the alloying elements and the alloy concentration. In

the high concentration structure, the kinetics of diffusion and the activation energy are discussed. Similar properties for H are also investigated for comparison. The activation energy of He migration is found to be significantly increased in $Pd_{24}Au_8$ and $Pd_{24}Pt_8$, indicating that the atom may be trapped at its origin site in these alloys. In addition, the alloying effect on the formation of a He dimer is investigated through its effective activation energy of formation and its pairing energy. A special case study of $Pd_{87.5}Pt_{12.5}$ demonstrates that a higher He activation energy is realized, consistent with recent experimental findings in the $Pd_{90}Pt_{10}$ system.

REFERENCES

[1] Donnelly, S. E. and Evans, J. H., *Fundamental Aspects of Inert Gases in Solids*, NATO ASI Series, 1990.

[2] Lasser, R., *Tritium and Helium-3 in Metals*, Springer, Berlin, 1989.

[3] Zinkle, S. J., Phys. Plasmas **12** (2005) 058101.

[4] Morishita, K., de la Rubia, T. D., Alonso, E., Sekimura, N., and Yoshida, N., J. Nucl. Mater. **283-287** (2000) 753.

[5] Victoria, M. et al., Fusion Engineering and Design **82** (2007) 2413.

[6] Kurtz, R. J., Heinisch, H. L., and Gao, F., J. Nucl. Mater. **382** (2008) 134.

[7] Mansur, L. K. and Coghlan, W. A., J. Nucl. Mater. **119** (1983) 1.

[8] Evans, J. H., Veen, A. V., and Caspers, L. M., Nature **291** (1981) 310.

[9] Iwakiri, H., Yasunaga, K., Morishita, K., and Yoshida, N., J. Nucl. Mater. **283-287** (2000) 1134.

[10] Henriksson, K., Nordlund, K., Krasheninnikov, A., and Keinonen, J., Appl. Phys. Lett. **87** (2005) 163113.

[11] Sharafat, S., Takahashi, A., Nagasawa, K., and Ghoniem, N., J. Nucl. Mater. **389** (2009) 203.

[12] Wilson, W. D., Baskes, M. I., and Bisson, C. L., Phys. Rev. B **13** (1976) 2470.

[13] Evans, J. H., J. Nucl. Mater. **79** (1979) 249.

[14] Schober, T., Dieker, C., and Trinkaus, H., J. Appl. Phys. **65** (1989) 117.

[15] Blaschko, O., Pleschiutschnig, J., Glas, R., and Weinzierl, P., Phys. Rev. B **44** (1991) 9164.

[16] Schober, T. and Farrell, K., J. Nucl. Mater. **168** (1989) 171.

[17] Snow, C. S. et al., J. Nucl. Mater. **374** (2008) 147.

[18] Knapp, J. A., Browning, J. F., and Bond, G. M., J. Appl. Phys. **105** (2009) 053501.

[19] Abell, G. C. and Attalla, A., Phys. Rev. Lett. **59** (1987) 995.

[20] Cowgill, D. F., Fusion Science and Technology **48** (2005) 539.

[21] Montheillet, F., Delaplanche, D., Fabre, A., Munier, E., and Thiébaut, S., Materials Science & Engineering A **494** (2008) 407.

[22] Thiébaut, S. et al., J. Alloys Compd. **446-447** (2007) 660.

[23] Bowman, R. C., Nature **271** (1978) 531.

[24] Thomas, G. J., Radiat. Eff. **78** (1983) 37.

[25] Thomas, G. and Mintz, J., J. Nucl. Mater. **116** (1983) 336.

[26] Abell, G. C., Matson, L. K., Steinmeyer, R. H., Jr., R. C. B., and Oliver, B. M., Phys. Rev. B **41** (1990) 1220.

[27] Abell, G. C. and Cowgill, D. F., Phys. Rev. B **44** (1991) 4178.

[28] Fabre, A. et al., J. Nucl. Mater. **342** (2005) 101.

[29] Trinkaus, H., J. Nucl. Mater. **323** (2003) 229.

[30] Jung, P. and Lässer, R., Phys. Rev. B **37** (1988) 2844.

[31] Petersen, M., Wilke, S., Ruggerone, P., Kohler, B., and Scheffler, M., Phys. Rev. Lett. **76** (1996) 995.

[32] Seletskaia, T., Osetsky, Y., Stoller, R. E., and Stocks, G. M., Phys. Rev. Lett. **94** (2005) 046403.

[33] Wilson, W. D., *Fundamental Aspects of Radiation Damage in Metals*, Springfield, 1979.

[34] Nielsen, B. B. and van Veen, A., J. Phys. F **15** (1985) 2409.

[35] Seletskaia, T., Osetsky, Y., Stoller, R. E., and Stocks, G. M., Phys. Rev. B **78** (2008) 134103.

[36] Zu, X. T. et al., Phys. Rev. B **80** (2009) 054104.

[37] Fu, C.-C. and Willaime, F., Phys. Rev. B **72** (2005) 064117.

[38] Becquart, C. S. and Domain, C., Phys. Rev. Lett. **97** (2006) 196402.

[39] Wixom, R. R., Browning, J. F., Snow, C. S., Schultz, P. A., and Jennison, D. R., J. Appl. Phys. **103** (2008) 123708.

[40] Alefeld, G. and Volkl, J., *Hydrogen in Metals I: Basic Properties*, Springer, Berlin, 1978.

[41] Fukai, Y., *The Metal-Hydrogen System: Basic Bulk Properties*, Springer-Verlag, 1993.

[42] Flanagan, T. and Oates, W., Annual Review of Materials Science **21** (1991) 269.

[43] Thiébaut, S. et al., Phys. Rev. B **57** (1998) 10379.

[44] Chan, C. T. and Louie, S. G., Phys. Rev. B **27** (1983) 3325.

[45] Henkelman, G., *Methods for Calculating Rates of Transitions with Application to Catalysis and Crystal Growth*, Thesis, 2001.

[46] Wilson, W. D., Bisson, C. L., and Baskes, M. I., Phys. Rev. B **24** (1981) 5616.

[47] Baskes, M. I. and Wilson, W. D., Phys. Rev. B **27** (1983) 2210.

[48] Elsässer, C., Ho, K. M., Chan, C. T., and Fähnle, M., J. Phys.: Condens. Matter **4** (1992) 5207.

[49] Vekilova, O., Bazhanov, D., Simak, S., and Abrikosov, I. A., Phys. Rev. B **80** (2009) 024101.

[50] Wang, Y., Sun, S. N., and Chou, M. Y., Phys. Rev. B **53** (1996) 1.

[51] Goodhew, P. J., Tyler, S. K., and Waldron, M. B., J. Nucl. Mater. **103** (1982) 1151.

[52] Thiébaut, S., Décamps, B., Pénisson, J., Limacher, B., and Guegan, A. P., J. Nucl. Mater. **277** (2000) 217.

[53] Gupta, R. P. and Gupta, M., Phys. Rev. B **66** (2002) 014105.

[54] Kleinman, L. and Bylander, D. M., Phys. Rev. Lett. **48** (1982) 1425.

[55] Jensen, F., *Introduction to Computational Chemistry*, John Wiley & Sons, 1999.

[56] Hamann, D. R., Phys. Rev. B **40** (1989) 2980.

[57] Troullier, N. and Martins, J. L., Phys. Rev. B **43** (1991) 1993.

[58] Monkhorst, H. J. and Pack, J. D., Phys. Rev. B **13** (1976) 5188.

[59] Perdew, J. P., Burke, K., and Ernzerhof, M., Phys. Rev. Lett. **77** (1996) 3865.

[60] Kreese, G. and Furthmuller, J., Comput. Mater. Sci. **6** (1996) 15.

[61] Sheppard, D., Terrell, R., and Henkelman, G., J. Chem. Phys. **128** (2008) 134106.

[62] Blöchl, P. E., Phys. Rev. B **50** (1994) 17953.

[63] Perdew, J. P. and Wang, Y., Phys. Rev. B **45** (1992) 13244.

[64] Hohenberg, P. and Kohn, W., Phys. Rev. **136** (1964) B 864.

[65] Sholl, D., J. Alloys Compd. **446-447** (2007) 462.

[66] Henkelman, G., Uberuaga, B. P., and Jónsson, H., J. Chem. Phys. **113** (2000) 9901.

[67] Kohn, W. and Sham, L. J., Phys. Rev. **140** (1965) A 1133.

[68] Kresse, G. and Joubert, D., Phys. Rev. B **59** (1999) 1758.

[69] Kreese, G. and Furthmuller, J., Phys. Rev. B **54** (1996) 11169.

[70] Sundell, P. and Wahnström, G., Phys. Rev. Lett. **92** (2004) 155901.

[71] Kamakoti, P. and Sholl, D., Journal of Membrane Science **225** (2003) 145.

[72] Nabi, Z., Vitos, L., Johansson, B., and Ahuja, R., Phys. Rev. B **72** (2005) 172102.

[73] Seletskaia, T., Osetsky, Y., Stoller, R., and Stocks, G., J. Nucl. Mater. **351** (2006) 109.

[74] Wolverton, C. and Asta, M., Phys. Rev. B **69** (2004) 144109.

[75] Montheillet, F., Delaplanche, D., Fabre, A., Munier, E., and Thiébaut, S., Materials Science & Engineering A **494** (2008) 407.

[76] Siegel, D. J. and Hamilton, J. C., Phys. Rev. B **68** (2003) 064105.

[77] Elsässer, C., Ho, K. M., Chan, C. T., and Fähnle, M., Phys. Rev. B **44** (1991) 10377.

[78] Sundell, P. G. and Wahnström, G., Phys. Rev. B **70** (2004) 224301.

[79] Mattsson, T. R. and Mattsson, A. E., Phys. Rev. B **66** (2002) 8.

[80] Zhang, C. and Alavi, A., J. AM. CHEM. SOC. **127** (2005) 9808.

[81] Maeland, A. and Flanagan, T., J. Phys. Chem. **68** (1964) 1419.

[82] Wang, X. W., Louie, S. G., and Cohen, M. L., Phys. Rev. B **40** (1989) 5822.

[83] Blaschko, O., Fratzl, P., and Klemencic, R., Phys. Rev. B **24** (1981) 277.

[84] Emig, J. A., Garza, R. G., Christensen, L. D., Coronado, P. R., and Souers, P. C., J. Nucl. Mater. **187** (1992) 209.

[85] Lasser, R., J. Phys. F: Met. Phys. **14** (1984) 1975.

[86] Alefeld, G. and Volkl, J., *Hydrogen in Metals II: Application-Oriented Properties*, Springer, Berlin, 1978.

[87] Moysan, I. et al., J. Alloys Compd. **322** (2001) 14.

[88] Henriksson, K., J. Nucl. Mater. **395** (2009) 45.

[89] Wu, Y., Yang, R., Zheng, H., and Wang, Y., J. Nucl. Mater. **354** (2006) 36.

[90] Hu, C. H. et al., Materials Science & Engineering B **123** (2005) 13.

[91] Hara, M., Wan, L., Matsuyama, M., and Watanabe, K., J. Alloys Compd. **428** (2007) 252.

[92] Nanu, D. E. and Böttger, A. J., J. Alloys Compd. **446** (2007) 571.

[93] Ke, X., Kramer, G. J., and Løvvik, O. M., J. Phys.: Condens. Matter **16** (2004) 6267.

[94] Moysan, I., Thiebaut, S., and Demoment, J., Fusion science and technology **48** (2005) 23.

[95] Sonwane, C. G., Wilcox, J., and Ma, Y. H., J. Phys. Chem. B **110** (2006) 24549.

[96] Kamakoti, P. and Sholl, D., Phys. Rev. B **71** (2005) 014301.

[97] Ke, X. and Kramer, G. J., Phys. Rev. B **66** (2002) 184304.